REPORT DOCUMENTATION PAGE		READ INSTRUCTIONS BEFORE COMPLETING FORM
1. REPORT NUMBER FR-9787	2. GOVT ACCESSION NO.	3. RECIPIENT'S CATALOG NUMBER
4. TITLE (and Subtitle) Design, Fabrication, and Evaluation of GATORIZED Ceramic-Wrought Alloy Attachment Concepts		5. TYPE OF REPORT & PERIOD COVERED Final Report 1 July 1974 through 31 July 1978
		6. PERFORMING ORG. REPORT NUMBER FR-9787
7. AUTHOR(s) S. A. McLeod B. H. Walker		8. CONTRACT OR GRANT NUMBER(s) N00019-74-C-0484
9. PERFORMING ORGANIZATION NAME AND ADDRESS Pratt & Whitney Aircraft Group Government Products Division Box 2691 West Palm Beach, Florida 33402		10. PROGRAM ELEMENT, PROJECT, TASK AREA & WORK UNIT NUMBERS
11. CONTROLLING OFFICE NAME AND ADDRESS Defense Advanced Research Project Agency 1400 Wilson Boulevard Arlington, Virginia 22209		12. REPORT DATE January 1979
		13. NUMBER OF PAGES 112
14. MONITORING AGENCY NAME & ADDRESS(if different from Controlling Office) Department of the Navy Naval Air Systems Command Washington, D. C. 20361		15. SECURITY CLASS. (of this report) Unclassified
		15a. DECLASSIFICATION/DOWNGRADING SCHEDULE

16. DISTRIBUTION STATEMENT (of this Report)

Approved for public release; distribution unlimited

DDC
RECEIVED
FEB 14 1979
C

17. DISTRIBUTION STATEMENT (of the abstract entered in Block 20, if different from Report)

18. SUPPLEMENTARY NOTES

19. KEY WORDS (Continue on reverse side if necessary and identify by block number)

GATORIZING®   Hot Pressed Silicon Nitride
Superplasticity   AF2-1DA
Ceramic-Wrought-Alloy Attachment
Hybrid-Pseudobladed Rotor
Hybrid Airfoiled Rotor

20. ABSTRACT (Continue on reverse side if necessary and identify by block number)

The attachment of hot pressed silicon nitride material (HPSN) ceramic blades to a wrought superalloy disk, utilizing the GATORIZING® forging process, was developed and demonstrated for application in small gas turbine engines. The development of this hybrid attachment concept consisted of fabricating, optimizing, and evaluating single ceramic blade/wrought alloy attachments by spin testing at ambient and elevated temperatures. The hybrid rotor concept was demonstrated by designing, fabricating, and spin testing several fully-bladed hybrid rotors, some containing ceramic simulated pseudoblades and others containing airfoil blades. The spin testing was conducted at speeds and temperatures comparable to small gas turbine engines.

DD FORM 1 JAN 73 1473   EDITION OF 1 NOV 65 IS OBSOLETE

79 02 12 008

DEVELOPMENT OF A GATORIZED®
HYBRID CERAMIC BLADED ROTOR

SUMMARY

The overall objective of this program was to develop and demonstrate the feasibility of a small gas turbine hybrid rotor consisting of a superalloy disk and ceramic blades. This objective was accomplished during a three phase effort consisting of (1) room-temperature development and characterization of a ceramic blade/superalloy attachment, (2) the development and elevated temperature spin testing of a fully-bladed, hybrid superalloy rotor containing ceramic pseudoblades (Figure 1), and (3) design fabrication, and elevated temperature spin testing of a hybrid rotor containing "airfoil" ceramic blades (Figure 2).
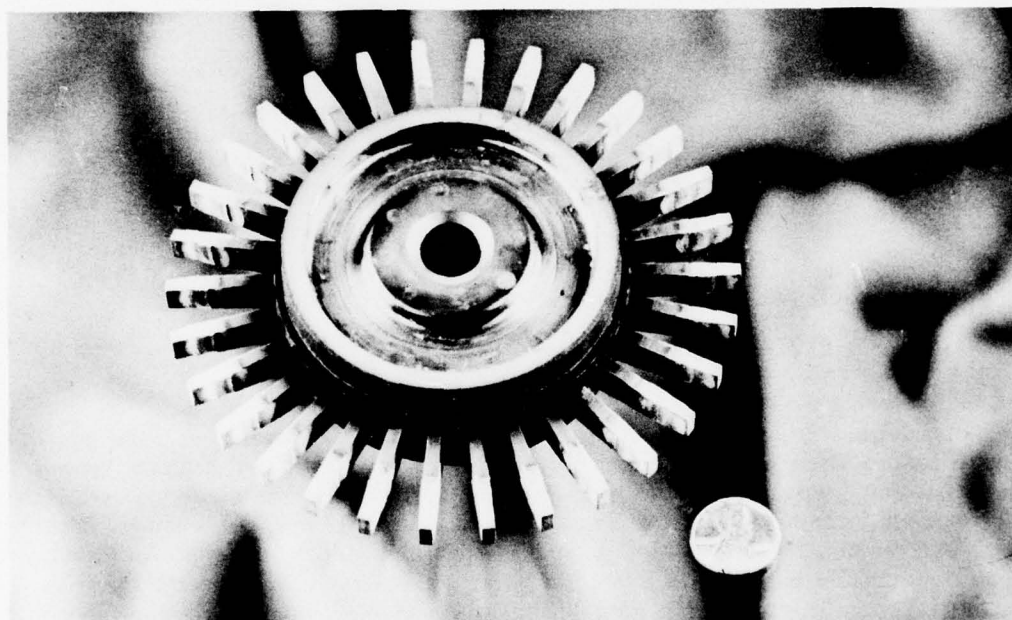
FE 156589

Figure 1. The Pseudobladed Hybrid Rotor After Completion of Program Milestone II Spin Test

The first phase of this program consisted of the room-temperature development and characterization of a ceramic blade/superalloy attachment concept which utilized the superplastic characteristics, induced in selected nickel based superalloys during the GATORIZING® forging process, to forge and diffusion bond wrought disk halves around ceramic turbine blade roots. Optimization and characterization of this concept was accomplished by an iterative fabrication/evaluation study to determine and optimize the room temperature mean and 99.5% lower bound ultimate tensile strength load carrying capabilities of individual hybrid attachments. Upon optimization, single attachment specimens were then tested to 100% of the room-temperature lower bound tensile strength to demonstrate attachment capability and to complete the first major program milestone.

iii

Figure 2. Hybrid Airfoiled Rotor

After demonstrating the room-temperature feasibility of the attachment, development was directed toward Phase II, elevated temperature demonstration of the attachment concept in a small gas turbine type hybrid rotor. Single- and multi-bladed hybrid test rotors were designed and fabricated for endurance testing aimed at demonstrating the hybrid attachment integrity at speeds and temperatures comparable to small gas turbine engine operation. An experimental analysis was conducted prior to rotor fabrication to determine hybrid rotor integrity. This analysis successfully predicted a rotor life in excess of the program Milestone II spin test requirement of 50 hr at 45,000 rpm with a blade temperature of 2250°F. The hybrid rotor circumferential attachment concept feasibility was successfully demonstrated during three separate program Milestone II tests which included (1) spin testing and cycling of a single-pseudobladed rotor at 45,000 rpm and 2250°F for over 66 hr with 97 isothermal LCF dwell and 10 thermomechanical cycles, (2) testing of a 28-pseudobladed hybrid rotor for 54 hr and 10 thermechanical cycles at 45,000 rpm with a blade temperature of 2250°F, and (3) testing of a fully bladed hybrid rotor (30 pseudoblades), Figure 1, at 45,000 rpm for 88 hr and 14 thermomechanical cycles with a 2250°F blade temperature. This testing adequately demonstrated hybrid attachment integrity and completed the Milestone II, as well as the initial contract requirements.

Hybrid rotor technology was further expanded within a 12-month Phase III contract extension resulting in the elevated-temperature spin testing of a hybrid rotor with "airfoil" ceramic blades. During the program extension, an airfoiled hybrid rotor containing ceramic airfoils of the "platformless blade" concept was designed and fabricated. With this airfoil concept, the airfoil and platform (endwall) sections of the conventional turbine blade are segregated into separate components to allow fabrication using single pass through grinding techniques that are approximately one-sixth as expensive as existing methods used to fabricate conventional type ceramic blades of the same material.

iv

To experimentally verify the design, room temperature spin testing of the ceramic airfoil blades was conducted and analyzed to determine the stress bearing capability of the hybrid airfoil attachment. This data was combined with rotor temperature data obtained during a thermal calibration in the spin facility to establish rotor test conditions for the program exension.

Upon completing thermal calibration, the hybrid airfoiled rotor was tested for 5 hr at speeds ranging from 30,000 to 45,000 rpm and with a blade temperature of 2250°F. A spin test abort destroying approximately 70% of the blades occurred at 45,000 rpm and a subsequent failure analysis determined spin tooling failure as the cause.

This test extended the state of the art of hybrid rotor technology and completed the program extension as well as program technical contract requirements.

PREFACE

This final report is submitted in accordance with the requirements of Contract N00019-74-C-0484 and details the work performed during the period from 1 July 1974 to 31 July 1978 and carries the P&WA designation FR-9787. This program was sponsored by the Advanced Research Projects Agency under the direction of Dr. Edward VanReuth and was conducted under the cognizance of Mr. W. T. Highberger, Department of the Navy, Naval Air Systems Command.

This program was conducted under the technical cognizance of M. C. VanWanderham, General Supervisor of the Mechanics of Materials and Structures section of the Materials and Mechanics Technology Department, at the Pratt & Whitney Aircraft Government Products Division.

ACKNOWLEDGEMENTS

The authors would like to acknowledge and extend thanks to W. D. Carruthers, previous Responsible Engineer, for his effort and support which greatly contributed to the success of this program.

TABLE OF CONTENTS

LIST OF ILLUSTRATIONS

LIST OF ILLUSTRATIONS (Continued)

LIST OF ILLUSTRATIONS (Continued)

LIST OF TABLES

SECTION I

INTRODUCTION

Increasing the performance of gas turbine engines has been, and continues to be, dependent on the development and utilization of higher temperature turbine materials which allow higher turbine inlet temperatures. Ceramic materials such as hot pressed silicon nitride and silicon carbide have been identified as excellent candidate turbine materials because of their capability of being used uncooled, at temperatures to approximately 2500°F. These materials are also potentially cheaper than current nickel base turbine alloys. However, the utilization of these materials is difficult due to their inherent brittleness and low coefficient of thermal expansion relative to metals. These two properties of ceramics intensify the effects of localized stresses, and thermal growth, and are of particular concern in the attachment of ceramic blades to metal turbine disks due to the high thermal and mechanical stress conditions.

The Government Products Division of Pratt & Whitney Aircraft Group proposed a solution to this problem using the P&WA GATORIZING® forging process to produce a viable ceramic wrought alloy blade attachment methodology. This process uses hot isothermal forging and a controlled forging rate to maintain a condition of superplasticity in material previously placed in that condition by special processing techniques. By exploiting the superplastic state of the material, the process allows forging of a wrought disk around ceramic turbine blade roots.

This approach addresses each of the above ceramic limitations by: (1) forming a surface-to-surface contact between the ceramic root and metal disk, and (2) forging (upsetting) of the disk material around the blades at temperatures above normal engine temperature. The near surface-to-surface contact formed between the ceramic root and metal disk minimizes local stresses which promote fracture in brittle materials such as hot pressed silicon nitride. Forging of the disk around the blades at temperatures above normal engine operating temperature also minimizes problems resulting from the thermal expansion difference between the ceramic blade and metal disk. This is accomplished as the thermal contraction of the disk from the forging temperatures maintains ceramic blade root and metal disk contact throughout the engine operational temperature range.

To research and develop this hybrid (ceramic blade/wrought alloy rotor) attachment methodology, the Advanced Research Project Agency funded this 3-phase technical effort to demonstrate the feasibility of attaching ceramic blades to metal rotors for gas turbine application. Phase I of this program consisted of room-temperature development and characterization of the ceramic blade/superalloy attachment concept. Phase II demonstrates the attachment concept at elevated temperatures in a small gas turbine type hybrid rotor containing ceramic pseudoblades. A Phase III program extension expanded the hybrid attachment concept by demonstrating an "airfoiled" hybrid rotor at elevated temperatures and speeds comparable to small gas turbine engine operation.

SECTION II

PHASE I — DEVELOPMENT AND CHARACTERIZATION OF ATTACHMENT CONCEPT

The first phase of this contract effort included the development and characterization, at room temperature, of a concept to attach ceramic blades to a wrought alloy disk. This effort consisted of concept selection, optimization, and evaluation with a Phase I, Program Milestone goal of spin testing the optimized attachment.

A. ATTACHMENT CONCEPT SELECTION

Four basic approaches to the ceramic blade-disk attachment problem were selected for study and analysis. Two of these approaches consisted of forming a superplastic wrought alloy around the ceramic dovetail blade root; the other two approaches combined the GATORIZING® forging process with diffusion bonding (requiring a minimum of material flow to form the attachment).

Initially, each of these four concepts were evaluated with respect to ease of fabrication, processing parameters, ceramic stability during forging, and load-carrying capability of the attachment. From this evaluation an attachment approach was selected combining the GATORIZING forging process with diffusion bonding (Figure 3). Using this attachment scheme, the root section of the hot-pressed silicon nitride blades were sandwiched between two nickel base, superalloy (AF2-1DA) disk halves and bonded in a forging-diffusion bond cycle.

B. ATTACHMENT CONCEPT OPTIMIZATION AT ROOM TEMPERATURE

After selecting the most promising attachment concept (Figure 3), an iterative study was conducted to optimize the load-carrying capability of the attachment. This optimization included: (1) photoelastic analysis, (2) forging process parameterization, (3) ceramic preheat treatment studies, and (4) a compliant layer study. The results of these analyses were evaluated by iteratively spin testing ceramic pseudoblade attachments to failure.

1. Photoelastic Analysis of Dovetail Geometry

A photoelastic analysis was conducted to optimize the ceramic blade root attachment geometry. This was accomplished by using an analytically-derived baseline root geometry in an iterative photoelastic optimization process. This baseline root geometry was analytically designed for an ultimate blade failure at 40,000 rpm based on a ceramic ultimate strength of 58 ksi. To optimize this root geometry, a model was fabricated from ¼-in. birefringent epoxy plastic. This model simulated a slice taken through the attachment area in a direction perpendicular to the disk slot/blade root centerline. The model was tested in the fixture illustrated in Figure 4 which was designed to subject the blade model to the centrifugal and forging loads that the blade root would be subject to under operating conditions. To account for forging load effects, the disk was split in the middle and uniformly loaded against the blade, as also indicated in Figure 4, and data were taken over the indicated area. The results of this analysis, as shown in Figure 5, along with a photo of the photoelastic fringe pattern obtained indicate a maximum localized stress for the baseline root configuration of approximately 31 ksi.

In comparison, a previously conducted analysis of a standard 45-deg dovetail used in conventional-metal dovetail blade attachments, as shown in Figure 6, indicated a maximum localized stress of 72 ksi. This stress exceeded the indicated ultimate failure stress of the baseline root geometry (31 ksi) by 132% and, in addition, exceeded the ultimate failure stress of the ceramic material (58 ksi) by 24%.

2
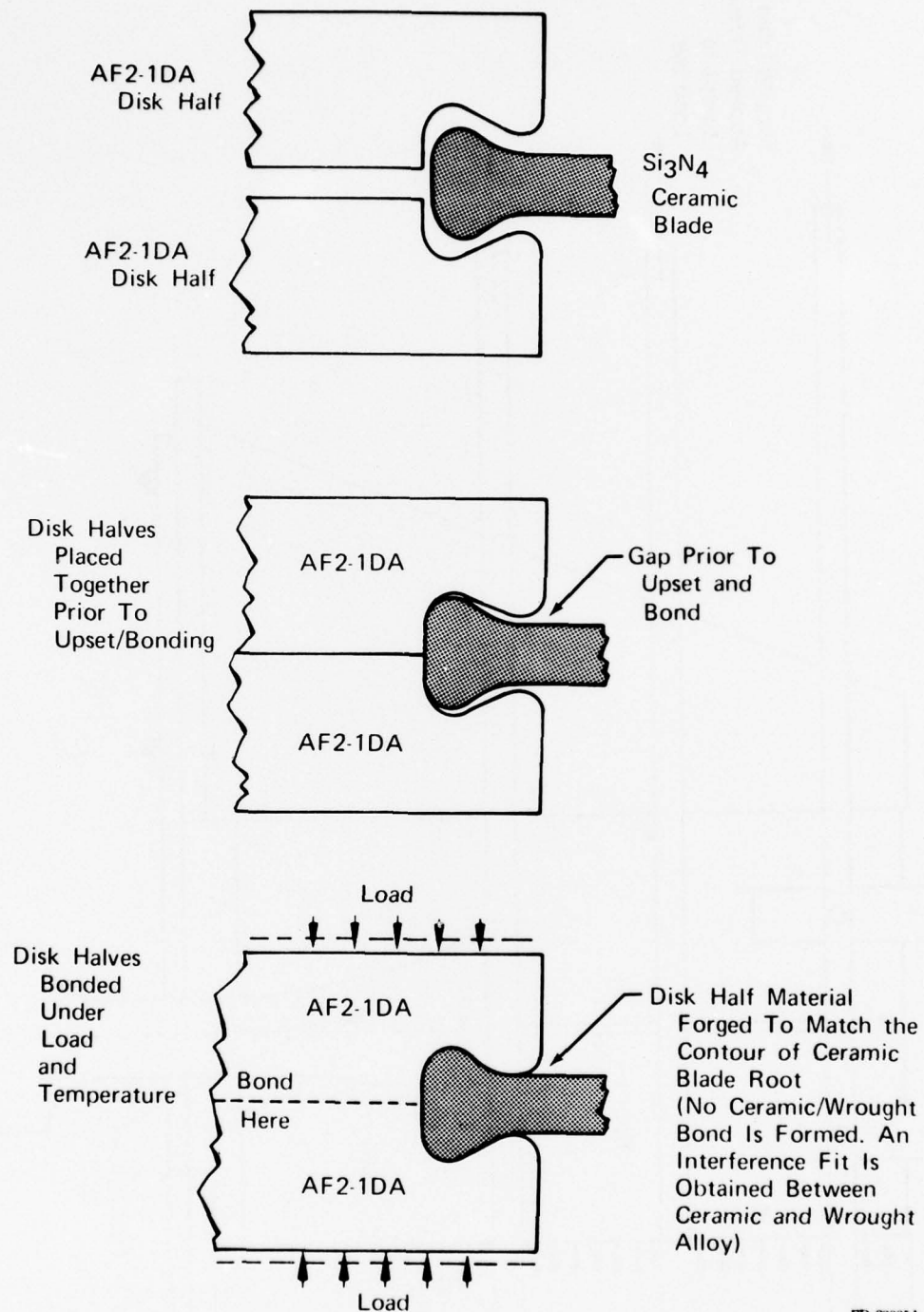
Figure 3. Fabrication Process for the Ceramic-Wrought Alloy Attachment

Forging Load
Applied Through
Straps to
Load Bar

Restraining Load

Split

Blade
ϕ

Disk

Load
Bar
(Sliding)

Blade is Analyzed in This Area

Blade Load
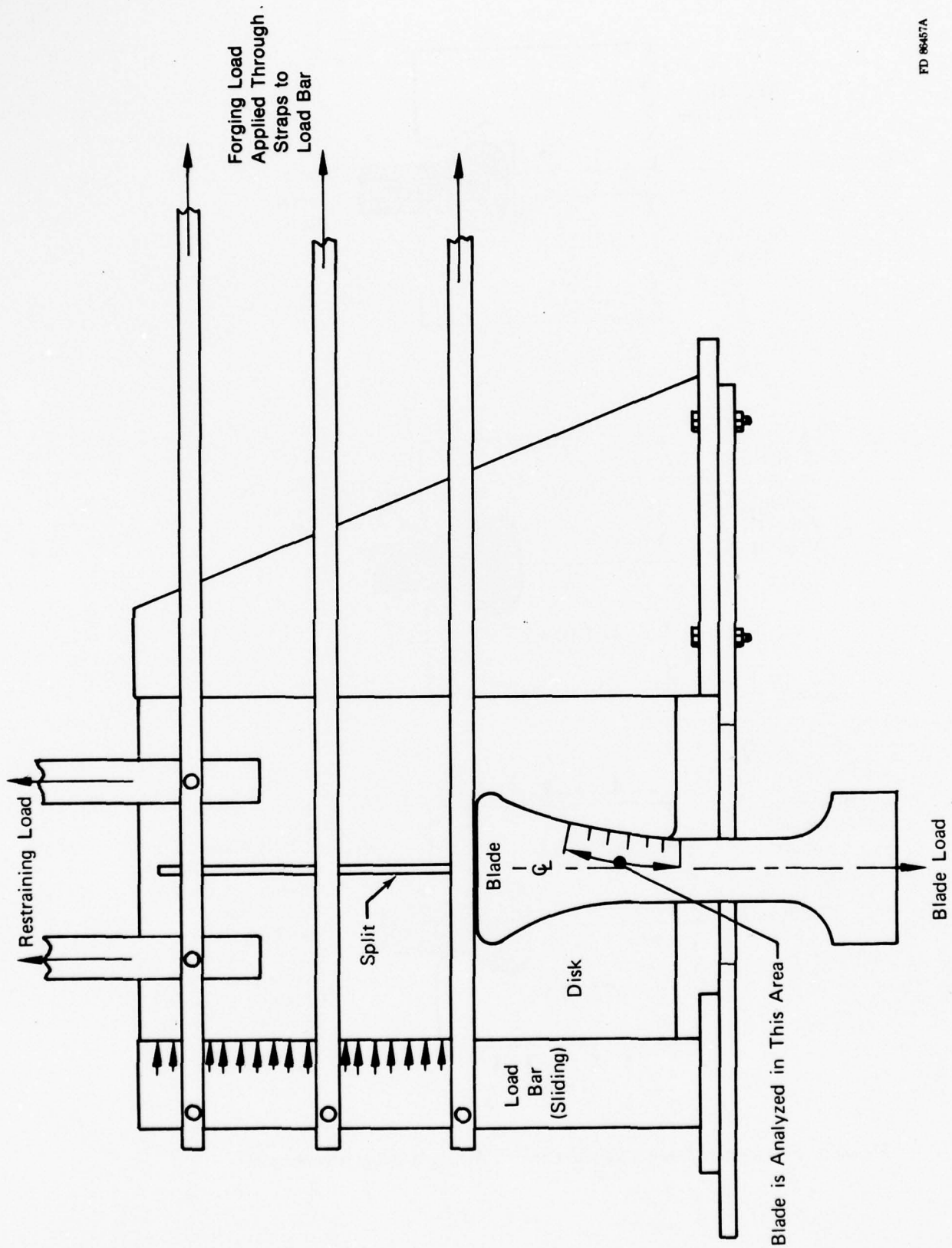
FD 86487A

Figure 4. Photoelastic Loading Schematic

4
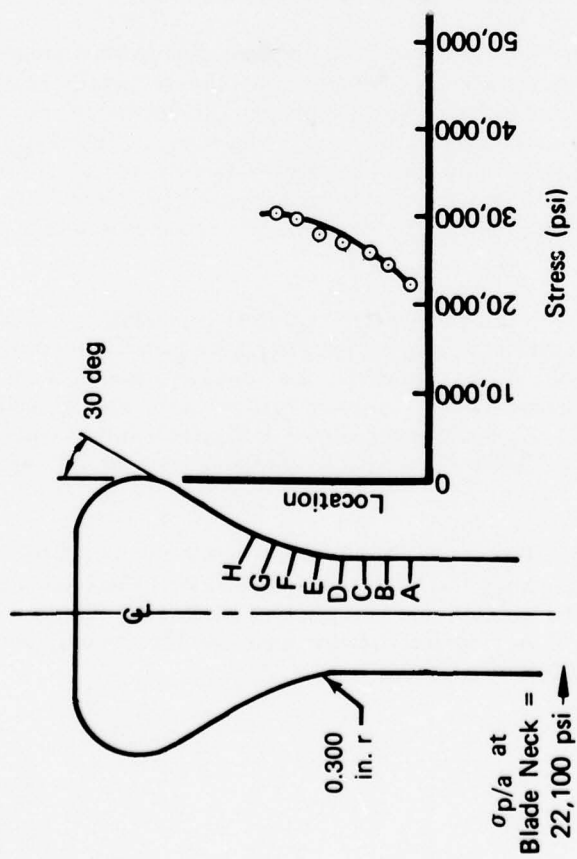
Figure 5. Photoelastic Analysis of Analytically-Designed Baseline Ceramic Blade Root
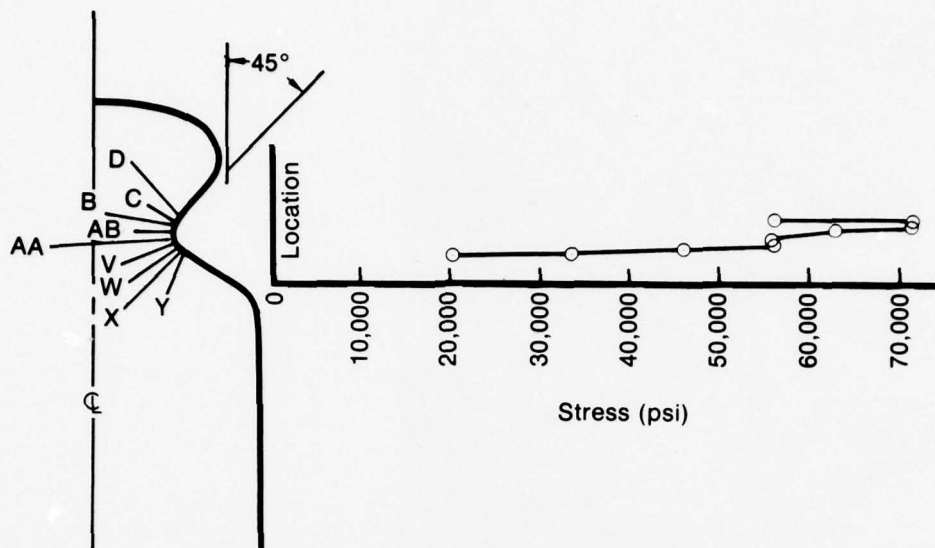
Figure 6. Typical Metal Dovetail Attachment

FD 86459C

This comparison clearly indicated the high stress concentrations produced in the conventional geometry, thus substantiating attachment redesign when using ceramic materials. Subsequently, the baseline geometry was chosen for continued optimization.

To further improve the baseline root geometry, an iterative photoelastic analysis was conducted and resulted in two ceramic dovetail configurations shown together with their respective fringe patterns in Figures 7 and 8. These results indicated that further increases in the blade root radius would decrease the stress level in the ceramic; however, an increasingly deep root would also be required to sustain the shear loads. Therefore, because of the small difference in the resultant stresses shown in Figures 7 and 8, it was decided that ceramic blades with the 0.5 and 1.0-in. radius dovetail configurations would be used in spin tests to determine actual ultimate speed and failure locations.

Since the selected attachment concept involved forging/diffusion bonding two disk halves around a ceramic dovetail root, the effect of increasing the forging load on the ceramic was of additional concern. To photoelastically study this effect, the simulated forging load on the dovetail shown in Figure 6 was increased by 50% over the original load, and a photoelastic analysis was conducted. The results of this analysis are shown in Figures 9 and 10 and indicate a maximum stress level increase of 20% for the 0.5-in. radius configuration and 35% for the 1.0-in. radius dovetail configuration.

The actual loading on the ceramic blade root after forging was not calculated because the AF2-1DA material yielded plastically during the forging and a portion of the cooling process. Both blade root designs were spin tested to determine the optimum parameters. The photoelastic studies illustrated that the effects of forging interference loads on the ceramic should be minimized to obtain the maximum attachment strength.

6
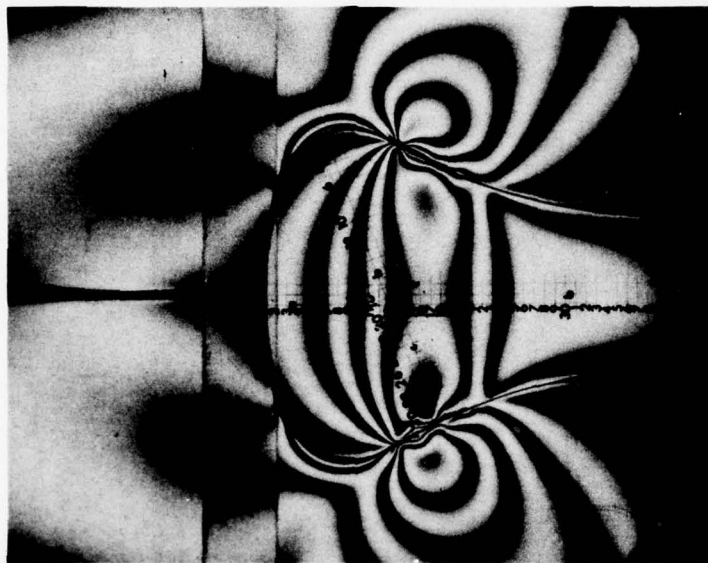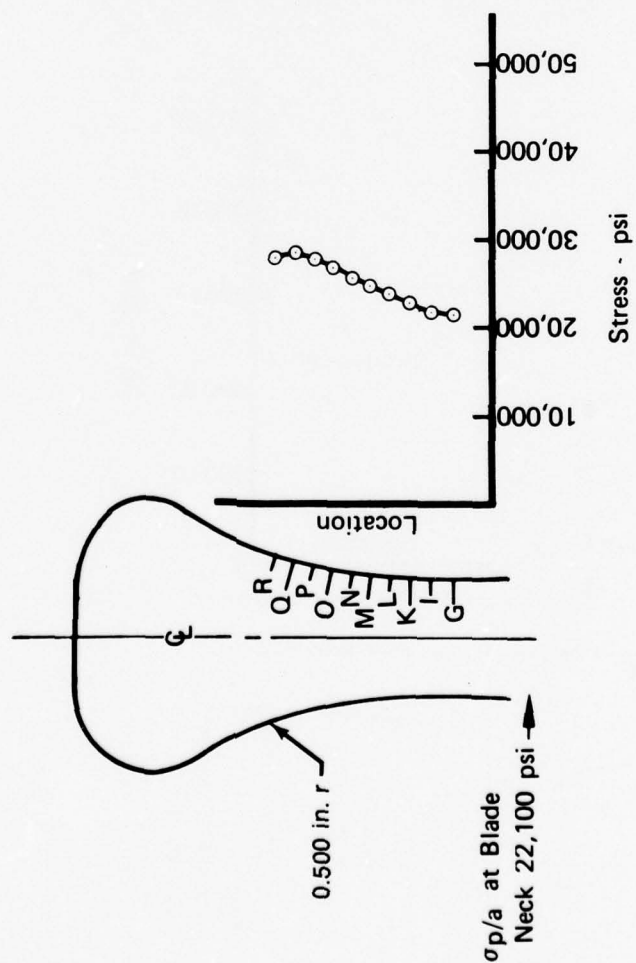
Figure 7. Result of First Experimental Blade Root Iteration

7
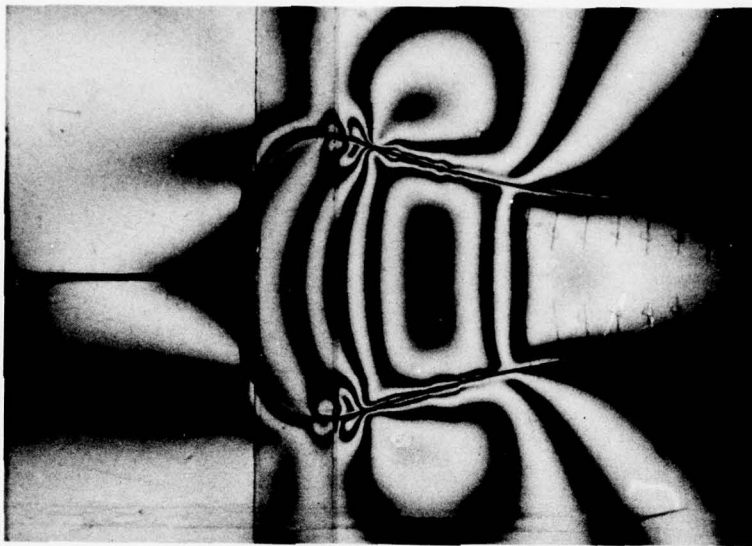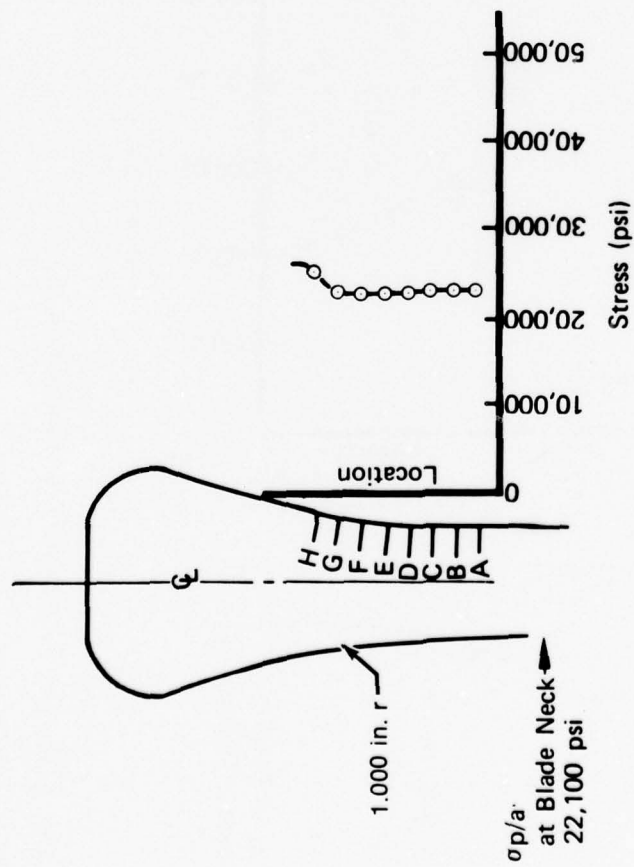
Figure 8. Result of Second Blade Root Iteration

8

Figure 9. *Photoelastic Analysis of Doubled Forging Load Effect on Ceramic Dovetail*

9

MOD 2
Prototype Stress vs Location
at 40,000 rpm
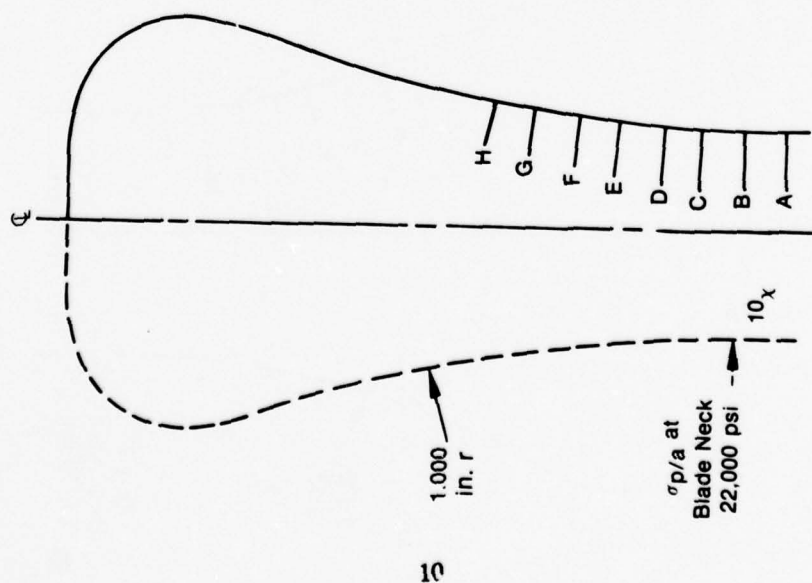
⊙ Stress Distribution vs Location

◇ Stress Distribution for Doubled Forging Load vs Location
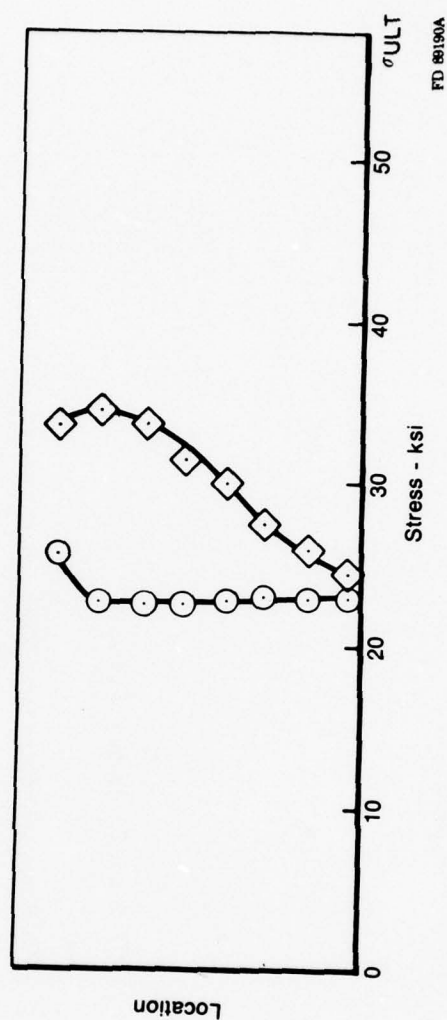
Figure 10. Photoelastic Analysis of Doubled Forging Load Effect on Ceramic Dovetail

FD 89190A

10

2. Forging Parametric Optimization

A study was conducted to optimize forging/diffusion bond process parameters and to investigate the effects of residual loads introduced by an interference fit on the ceramic during forging.

The forging/diffusion bond process was optimized by forging simulated attachment specimens as shown in Figure 11. These specimens were machined to vary the root cavity dimensions and amount of upset, as illustrated in Figure 12. Following forging/diffusion bonding, specimens were sectioned to evaluate the resultant ceramic-wrought alloy interface and diffusion bond areas.

Results of these forging trials indicated that the ceramic-wrought alloy interface contact can be maintained by controlling all preforged root cavity dimensions. In addition, an excellent diffusion bond could be obtained with as little as 0.003-in. total material upset. This was evidenced by the lack of a discernible bond line in the bond area (Figure 13).

An interface reaction between the AF2-1DA and NC-132 silicon nitride was detected after sectioning and analysis of the interface (Figure 14). Upon investigation of this interface reaction it was concluded that the load-carrying capability of the attachment could have been decreased. Thus, an interlayer of platinum was introduced at the interface to eliminate the reaction. It was also found to be compliant as will be discussed in later sections.

The previously discussed photoelastic blade root analysis indicated a degradation in load-carrying capability as a result of increased interference fit on the ceramic. The interference fit was calculated as the total amount of upset minus the initial clearance around the dovetail section prior to forging. This is illustrated in Figure 15.

To optimize the forging parameters to produce maximum attachment strength, various interference fits between AF2-1DA and the ceramic blade, during the forging process, were studied for the 0.5 in. and the 1.0 in. radius dovetail geometry.

Initially, 7 attachment specimens with the 0.500-in. dovetail radius and 11 specimens with the 1.00-in. dovetail radius were fabricated and bonded, as shown in Figures 16 and 17, to study the effect of varying the amount of interference. All of these ceramic blades were polished to remove dovetail machining marks and preheat treated at 2200°F for 3 hr. The ceramic pseudoblade dovetail was polished on the load-bearing radius to remove surface flaws generated during blade fabrication. As suggested in literature and as an added measure to improve load-carrying capability of the ceramic, the 2200°F heat treatment (which will be discussed in a later section) was conducted as a possible means of "healing" (or alleviating) any machine-induced surface cracks by oxidizing the ceramic surface.

After fabrication and bonding, each attachment specimen was spin tested to failure to determine the interference effect. After spin testing to failure, the corresponding P/A ultimate stresses (Figure 18) were calculated at the tangent point of the root radius.

The spin test results and Weibull distribution of the ultimate stress levels for the seven 0.500-in. and eleven 1.00-in. root radius dovetail blades are shown in Figures 19 and 20, and Table 1 respectively.

As is evident from Table 1, there is little correlation in the ultimate failure stress of the ceramic and the amount of ceramic-AF2-1DA interference created during the upset-bonding process. For example, of the first seven specimens with the 0.5-in. root radius configuration, wide scatter in ultimate stress (12.5 to 33.2 ksi) was exhibited for those attachment specimens forged with 0.004-in. interference fit. This scatter was also manifested in the 1.0-in. root radius data.

11
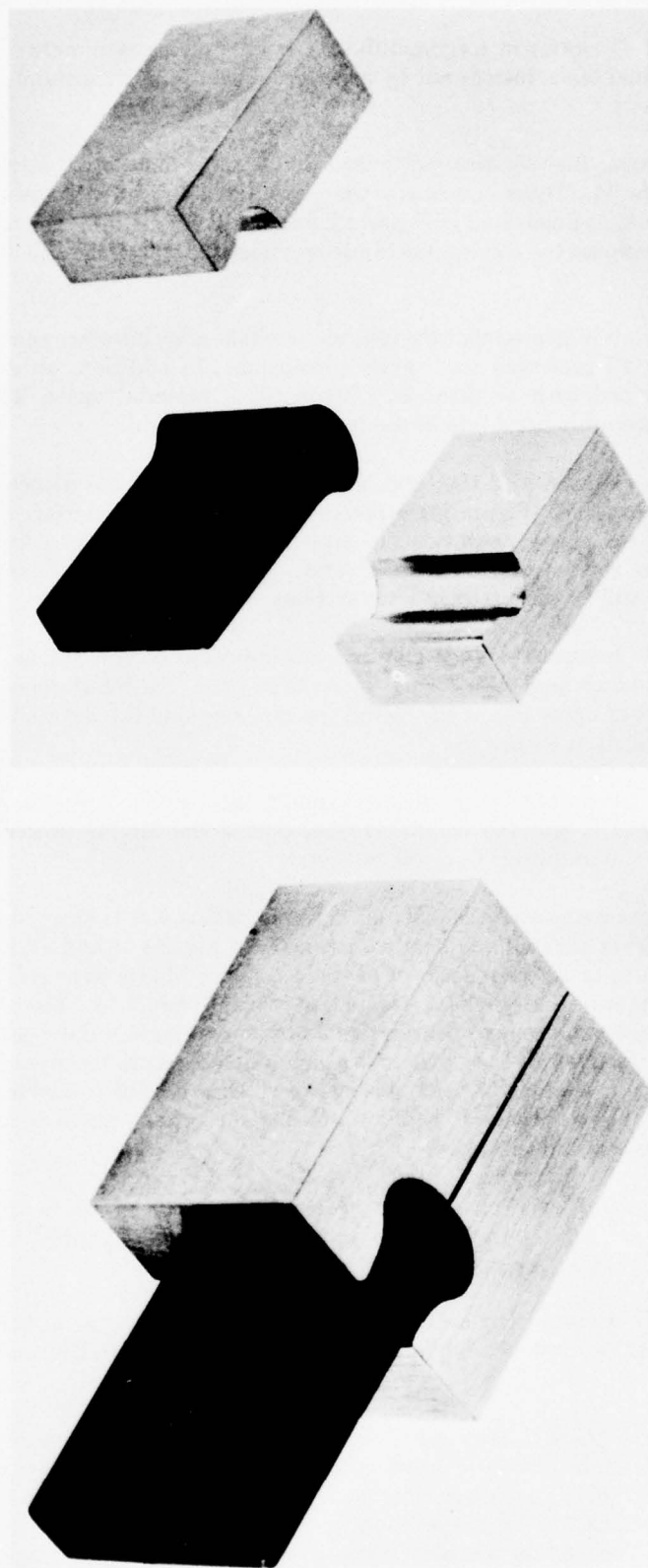
Figure 11. Specimen Using Dovetail Ceramic Blade Roots To Analyze the Forging Parameters

These Dimensions
Can be Varied To
Control the Contact
and Load on
the Ceramic
Blade Root

Vary the Amount
of Upset To Obtain
Optimum Bond

This Dimension
Can be Varied
To Control the
Contact and
Compressive
Load on the
Ceramic Root
Neck
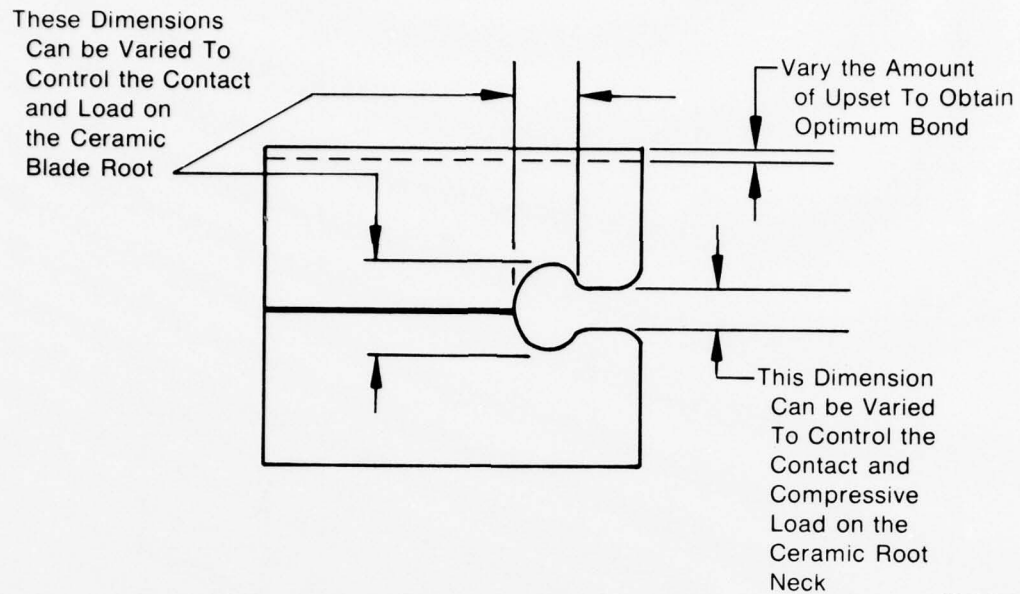
FD 86454A

Figure 12. Sketch of Upset-Bonding Specimens for Dovetail Blade Root Showing Cavity Dimension Variations
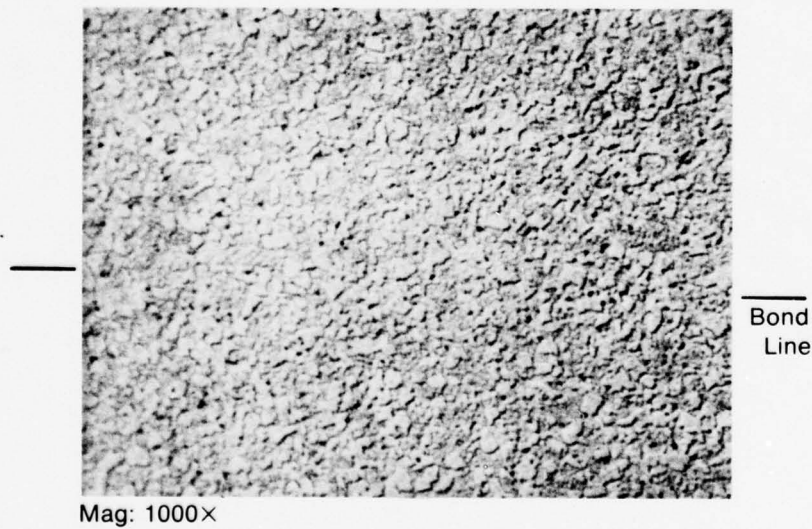
Bond
Line

Mag: 1000×

FD 86451A

Figure 13. Photomicrograph of the Diffusion Bond. Lack of a Discernible Bond Line Indicates an Excellent Bond

13

Interference = Total Upset — Pre-upset Clearance
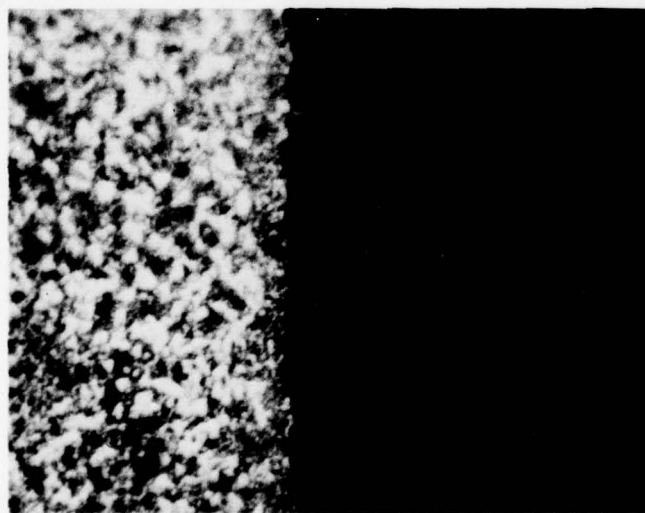
Figure 15. Upset-Bonding Specimen Showing Interference Fit

Mag: 1000X

Figure 14. Photomicrograph of Silicon Nitride AF2-1DA Contact Area

14
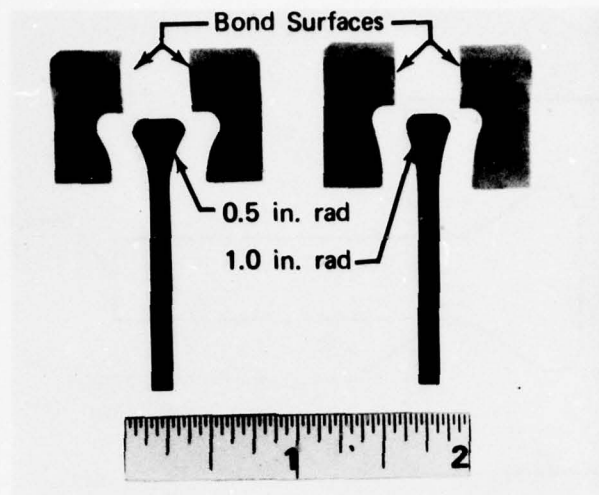
FD 88948

Figure 16. Two Ceramic-Wrought Alloy Attachment Configurations Studied
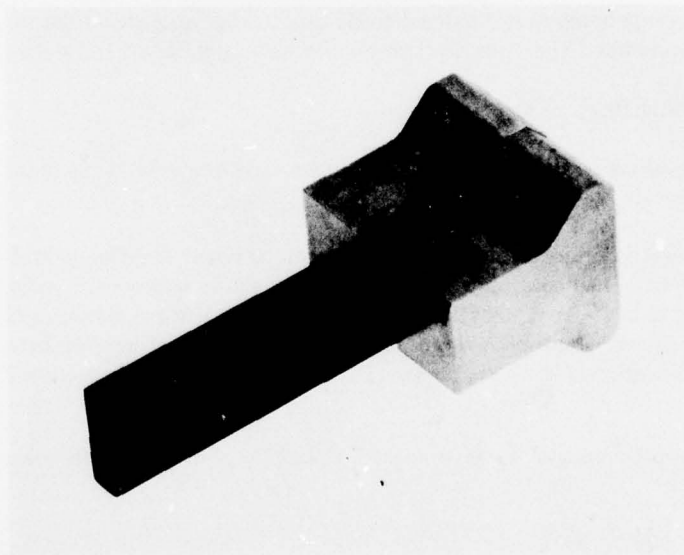
FD 88949

Figure 17. Diffusion-Bonded Spin Test Specimen

15

AF2-1DA

Ceramic
Pseudoblade

AF2-1DA

Area of P/A Ultimate
Stress Calculation
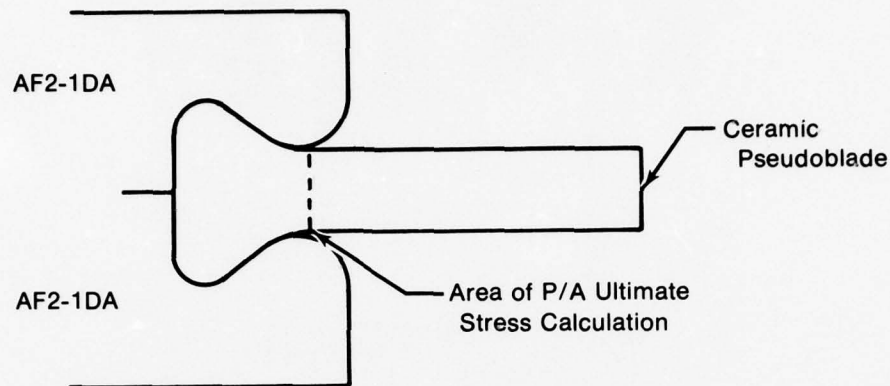
FD 94435A

Figure 18. Area Used for P/A Stress Calculations

In addition, the Weibull distributions of the ultimate strengths indicate that the 2-Sigma* lower bound for the 1.0-in. radius configuration (3.13 ksi as shown in Figure 20) was approximately one-half that of the 0.50-in. radius configuration (6.26 ksi as shown in Figure 19). Although this trend was predicted by the photoelastic analysis, the mean ultimate strengths (20.8 ksi and 19.6 ksi for the 1.0-in. and 0.50-in. radius root configurations, respectively) were too close to provide a meaningful correlation.

The above discrepancies were believed to be due to the large degree of data scatter. From these tests it was concluded that the random results were attributed to two major areas:

1. Machining flaws in the ceramic

2. Point contact between the ceramic and wrought material, thus point loading the dovetail.

To further investigate these possibilities, ceramic preheat treatment and compliant layer studies were conducted. The ceramic preheat treatment study was conducted to investigate the possibility of using a heat treatment to "heal" machining surface flaws in the ceramic. The compliant layer study was conducted in an effort to eliminate point loading between the ceramic and wrought alloy dovetail of the attachment. Each of these studies is discussed in the following paragraphs.

---

* The 2-Sigma lower bound stress level is that stress above which 97.5% of the specimen failures should occur.
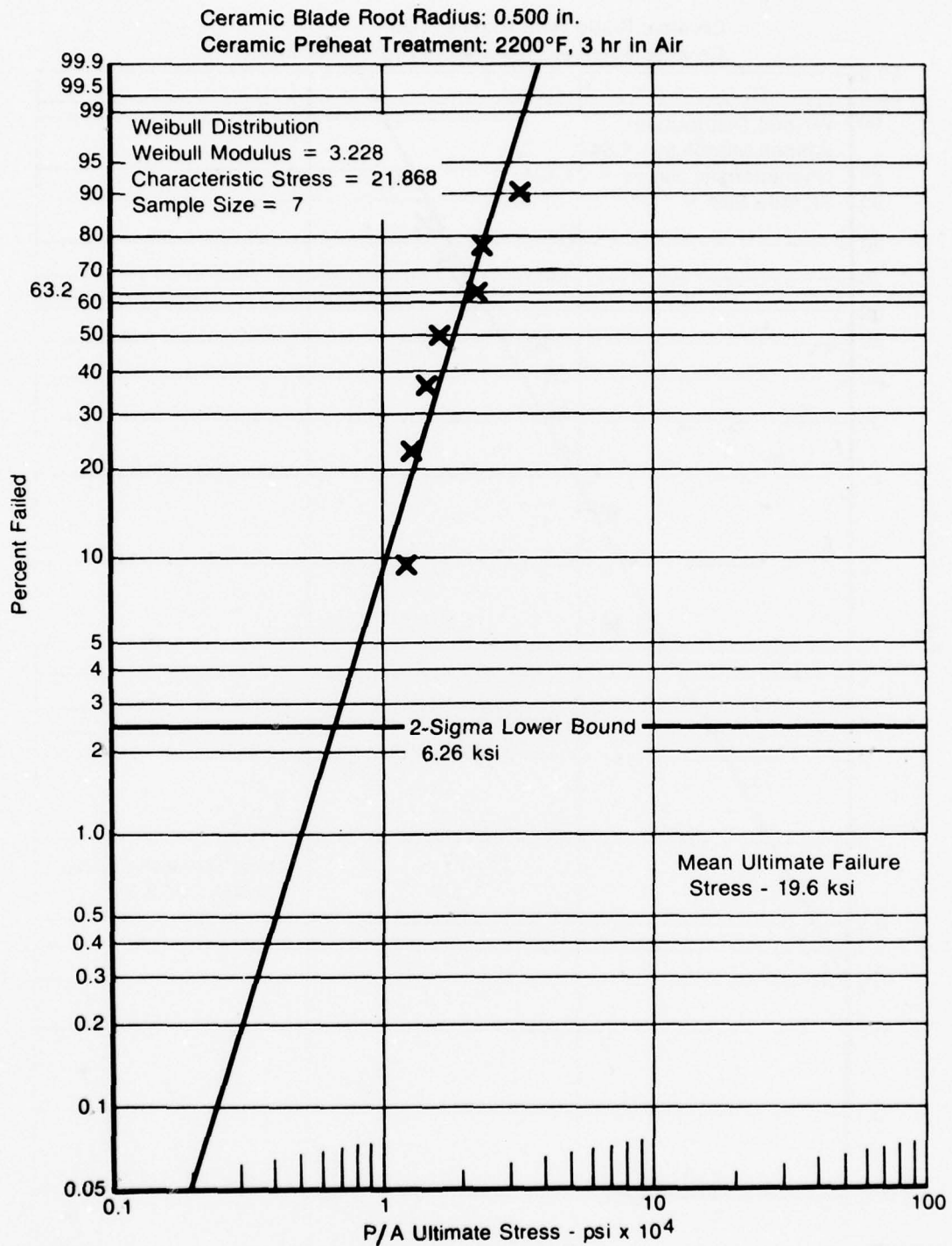
Figure 19. *Room-Temperature Ultimate Stress of Ceramic-Wrought Alloy Attachment*

17
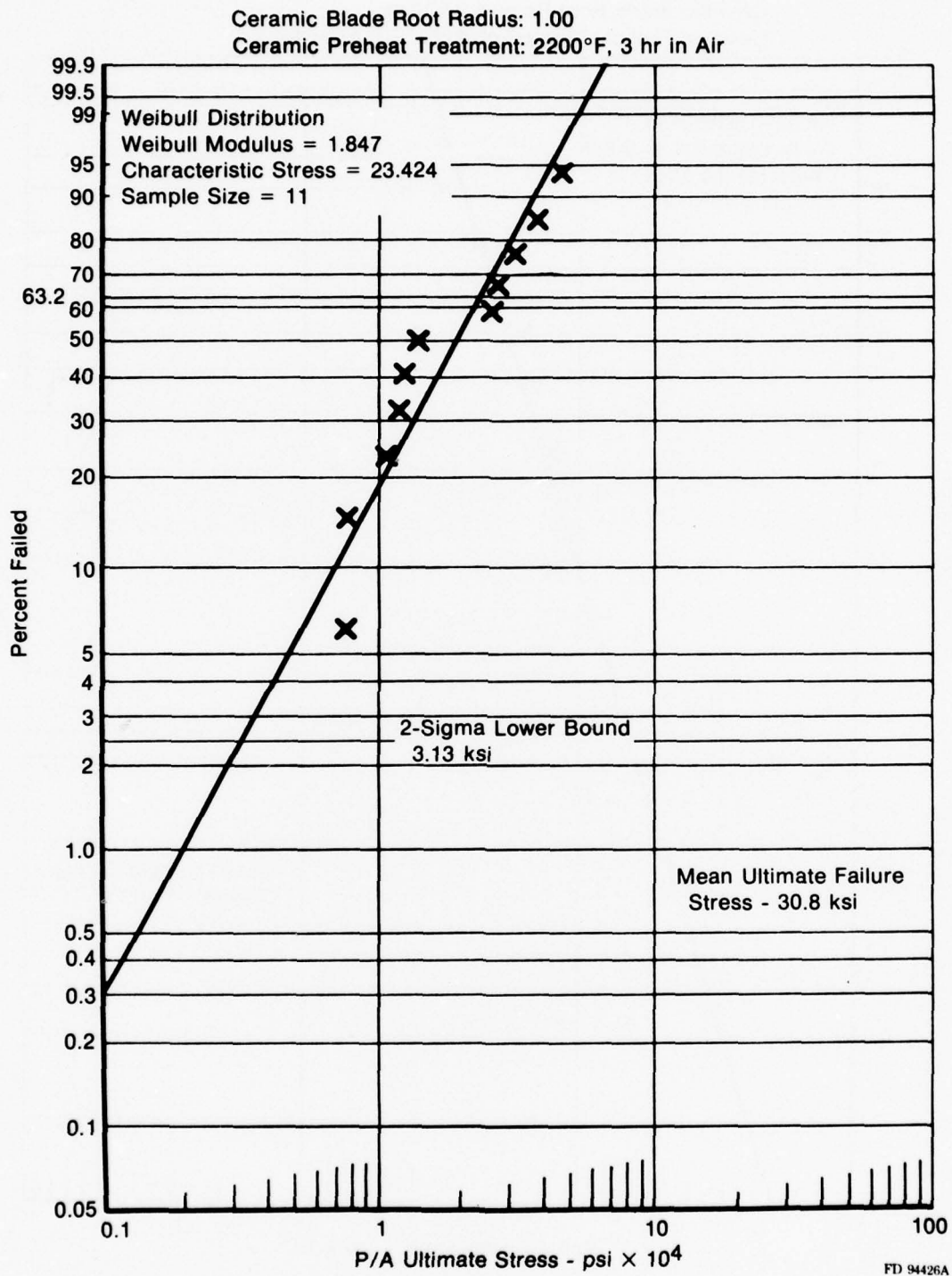
Figure 20. *Room-Temperature Ultimate Stress of Ceramic-Wrought Alloy Attachment*

18

TABLE 1. RESULTS OF ROOM-TEMPERATURE SPIN TEST-
ING CERAMIC BLADE ATTACHMENT SPEC-
IMENS

Attachment S/N	Dovetail Root Radius Configuration (in.)	Ceramic-Wrought Alloy Interference (in.)	Speed at Failure, (rpm)	P/A Stress at Failure, (ksi)
1	0.5	0.004	48,400	33.2
2	0.5	0.004	41,000	24.2
3	0.5	0.010	40,400	23.1
4	0.5	0.002	34,900	17.2
5	0.5	0.004	33,000	15.4
6	0.5	0.004	43,400	12.5*
7	0.5	0.002	30,600	13.3
8	1.0	0.011	53,300	38.2
9	1.0	0.005	58,900	46.7
10	1.0	0.0075	48,200	31.2
11	1.0	0.006	45,000	27.2
12	1.0	0.002	62,400	25.7*
13	1.0	0.0085	30,300	12.3
14	1.0	0.005	32,400	14.4
15	1.0	0.002	24,000	7.7
16	1.0	0.002	28,400	10.8
17	1.0	0.002	23,700	7.6
18	1.0	0.002	42,400	11.8*

* This attachment specimen used a shorter ceramic blade, thus the high rpm and low stress.

3. Ceramic Preheat Treatment Studies

As previously discussed, the initial ceramic preheat treatment was conducted at 2200°F for 3 hr in air. As a result of a literature search, this heat treatment was used as a possible means of "healing" any machine-induced surface cracks by oxidizing the ceramic surface.

To further investigate the preheat treatment oxidation effect, a study was conducted during Phase I, which incorporated increased heat treat temperature and duration. The NC-132 ceramic blade specimens were machined, polished, and heat treated in air at 2500°F in two lots, one for 3 hr and one for 23 hr. Two different heat treatment durations were chosen as an indicator of heat treatment time dependence.

Five ceramic blades were used for this study. Three ceramic blades of the 1.00-in. root radius were preheat treated at 2500°F for 3 hr, and two blades of the 0.5-in. radius were preheat treated at 2500°F for 23 hr. Because previous spin test results did not indicate a blade root radius preference, these ceramic blades were used for this test due to their availability. The heat treated blades were forged-bonded between AF2-1DA simulated disk halves and spin tested to failure. Results of these tests are tabulated in Table 2.

TABLE 2. RESULTS OF ROOM-TEMPERATURE SPIN
TESTING INVESTIGATING THE EFFECT OF
CERAMIC PREHEAT TREATMENT

S/N	Root Radius (in.)	Preheat-Treatment (in Air) (°F/hr)	Actual Interference (in.)	Speed at Failure, (rpm)	P/A Stress At Failure, (ksi)
19	1.000	2500/3	0.002	36.600	18.0
20	1.000	2500/3	0.002	30,500	12.5
21	1.000	2500/3	0.014	32,700	14.4
22	0.500	2500/23	0.001	39,400	22.0
23	0.500	2500/23	0.001	39,800	22.4

19

The data tabulated in Table 2 indicated that the 2500°F/3 hr heat treatment had no advantage over the previously used 2200°F/3 hr heat treatment. However, the results for the specimens preheat treated at 2500°F for 23 hr indicated an average stress (22.2 ksi) above both mean stress levels (Figures 19 and 20) and, in addition, indicate a potential for reduced scatter. Because no previous spin test data indicated a higher stress level capability for either blade root design, it was concluded that both repeatability and ultimate strength capability would be enhanced by using the 2500°F/23 hr preheat treatment.

Realizing that the existing data were not sufficient to make a statistical conclusion, additional preheat treatment tests were also conducted during the load distributing compliant layer study, discussed in the following paragraphs. The results of the additional tests, however, confirmed the advantages of the 2500°F/23 hr preheat treatment discussed; thus, this preheat treatment was used in subsequent testing, during Phase I.*

4. Compliant Layer Studies

As previously discussed, initial testing of single hybrid attachments to determine the effect of interference fit during forging/diffusion bonding produced widely scattered data. This randomness was believed due, in part, to compressive point loading of the ceramic dovetail caused by ceramic-wrought alloy point contact. The mating surfaces of the ceramic dovetail and corresponding wrought alloy disk halves were machined by two different operations, thus, making it virtually impossible to obtain complete surface-to-surface contact throughout the load-bearing area of the dovetail. Since the ceramic is not ductile material, the dovetail surface will not deform like a metal blade and alleviate a point load situation. Therefore, a study was conducted to obtain a sufficient compliant layer to achieve the surface-to-surface contact.

For this study both a ceramic and metallic compliant layer material were considered. In both cases the requirements for the compliant layer were established as follows:

1. The compliant layer must be capable of withstanding the high-temperature extremes that it will be exposed to during the fabrication cycle, during post fabrication heat treatment, and ultimately, during use in an engine application. Thus, the material must possess adequate material strength and corrosion resistance.

2. The compliant layer must be of a nonreactive material, producing no detrimental reactions to either the silicon nitride blade root or the AF2-1DA blade holder. Thus, this compliant layer must not be detrimental to any of the parent material characteristics under any conditions of the turbine rotor duty cycle.

3. The compliant layer must offer load-distributing characteristics. Thus, the layer must be capable of transferring the compressive load of the AF2-1DA uniformly to the silicon nitride without creating point loading.

4. Ideally, the compliant layer should have a low thermal conductivity. This low conductivity would aid in maintaining the AF2-1DA in its operable temperature range while the ceramic is at a higher temperature.

---

* Additional ceramic preheat treat studies were conducted during Phases II and III in a continuing effort to increase the load-carrying capability of the attachment. These studies and their resultant impact are discussed in the respective phases.

Considering these requirements, a fibrous aluminum oxide (alumina) and a 0.005-in. platinum shim were chosen as compliant layers for further study. The fibrous alumina was chosen for study due to its commercial availability as well as its fulfillment of the established requirements.

The platinum compliant layer was chosen for its nonreactive nature, its high melting temperature, and its ductility. The low thermal expansion of platinum combined with its ductility, made it a good candidate for eliminating possible residual stresses induced in the ceramic during cooldown after the forging-bonding cycle. Additionally, the use of any compliant layer would eliminate any previously noted reaction in the ceramic-wrought alloy interface.

The alumina and platinum materials were evaluated by fabricating and spin testing hybrid attachments using each material individually as a compliant layer between the ceramic dovetail and wrought alloy disk material.

During initial testing of the alumina compliant layer attachments, a design modification was incorporated in the AF2-1DA simulated disk-half design. This modification was incorporated to balance the bending moment created in the AF2-1DA dovetail area during spin testing by (1) the material required to form the dovetail, and (2) the load that the ceramic blade placed on the attachment while rotating. This imbalance and the design modification are shown in Figure 21.

Subsequently, ceramic-wrought alloy attachments using the platinum and alumina compliant layers, the modified "balanced" attachment design, and ceramic pseudoblades preheat treated at 2500°F for 23 hr were fabricated and spin tested at room temperature to compare the load-carrying capabilities of each compliant material. Figures 22 and 23, illustrate the "balanced" attachment with the platinum and alumina compliant material, respectively.

Both the alumina and platinum compliant layers increased the load-carrying capabilities of the hybrid attachment; however, two problems were exposed during this spin testing which eliminated the fibrous alumina as a potential compliant layer candidate. First, the absorption qualities of the fiber allow the compliant layer to absorb moisture, and, more probably, oil. The absorption of either of these (or any liquids) supplies a medium that allows the compliant layer to compact further than originally compacted during the forge-bond cycle. This compaction produces an undesirable looseness in the ceramic-wrought alloy attachment that would lead to premature ceramic failure. Secondly, spalling of the fibrous alumina during centrifugal loading would produce a loose ceramic attachment.

The results of spin testing four attachments, two of each compliant material, are shown in Table 3. The use of the platinum compliant layer had obvious potential, as the 60,200 rpm failure speed attained was the highest reached at that time using a full length NC-132 pseudoblade.

The average ultimate stress at failure for the two balanced specimens using the platinum compliant layer was 43.6 ksi, an increase of 96% over the best previous "unbalanced" attachment average ultimate stress with the same ceramic preheat treatment. Thus, the 0.005-in. platinum shim compliant layer and the "balanced" attachment were chosen for future testing as the combination produced a more uniform loading on the ceramic blade root.

At this time the hybrid attachment concept was sufficiently optimized to proceed with further evaluation and characterization to establish a baseline load-carrying capability of the attachment at room temperature.

21
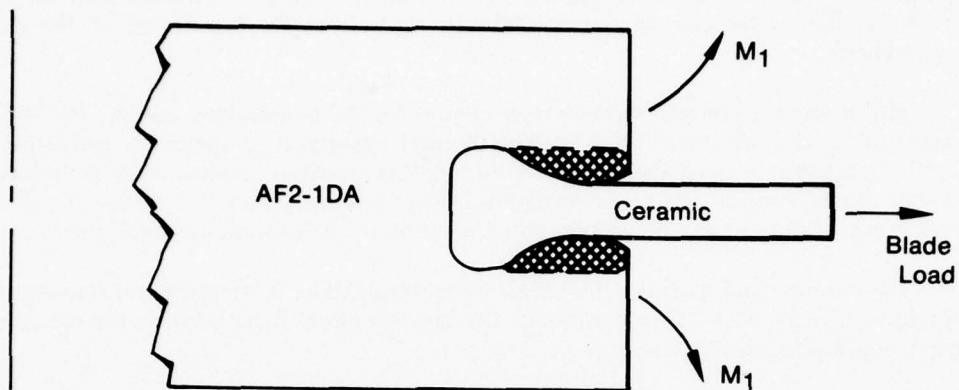
a) Imbalanced Attachment:
   The Blade Load and Mass of the Shaded Area Create a Moment,
   M_1, During Spin Testing Which Would Result in Ceramic Blade/AF2-1DA
   Contact Area Shift and Thus Lower Ultimate Strengths.
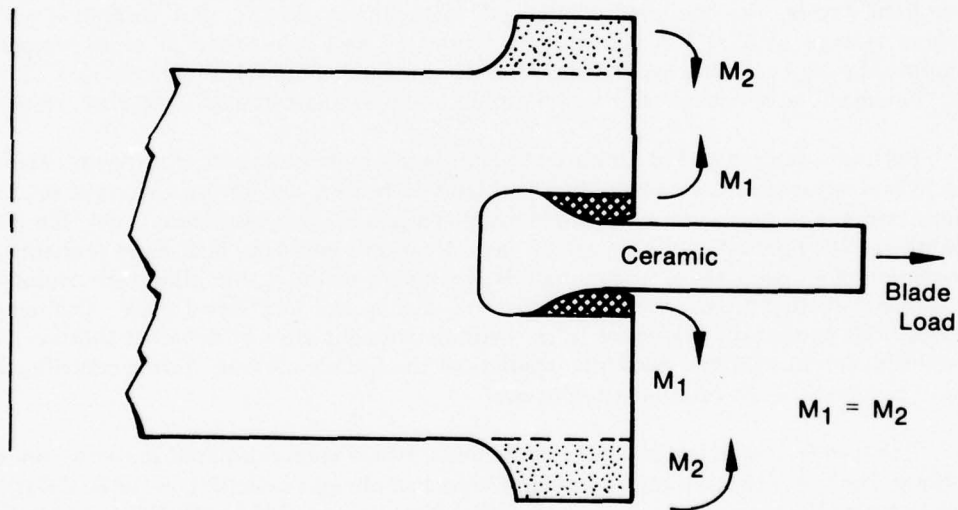
b) Balanced Attachent
   The Added Material in This Design Balances the Moment
   Created by the Ceramic Blade and Dovetail.

FD 91881A

Figure 21. Balanced and Imbalanced Attachments

22
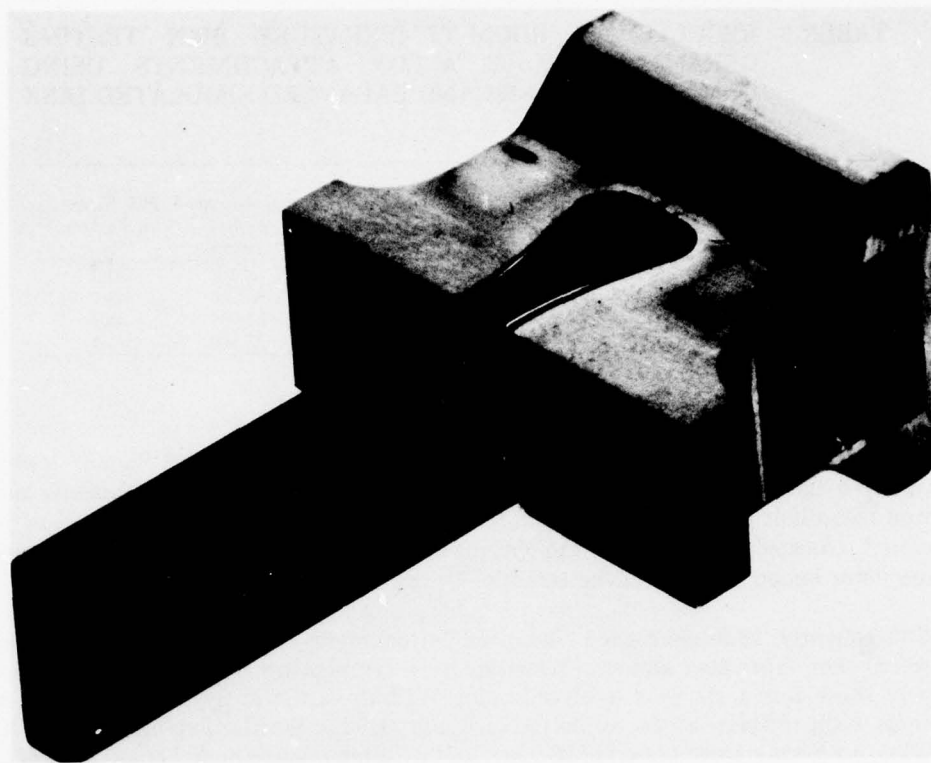
FAE 145375

Figure 22. Ceramic-Wrought Alloy Attachment Using Platinum Shim Compliant Layer and Balanced Attachment Design
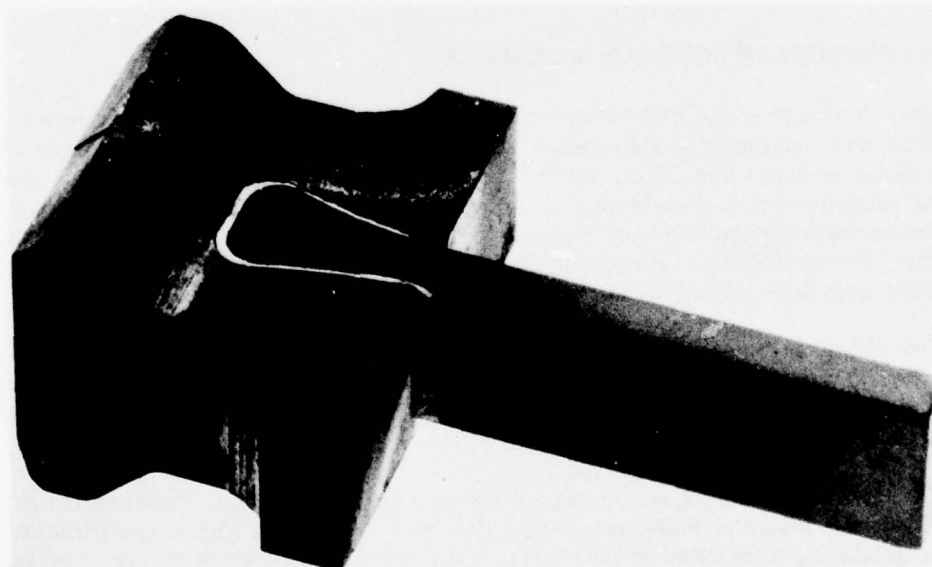
FAE 145652

Figure 23. Ceramic-Wrought Alloy Attachment Using Alumina Compliant Layer and Balanced Attachment Design

23

TABLE 3. RESULTS OF ROOM-TEMPERATURE SPIN TESTING CERAMIC-WROUGHT ALLOY ATTACHMENTS USING COMPLIANT LAYERS AND BALANCED SIMULATED DISK HALVES

S/N	Blade Root Radius (in.)	Ceramic Preheat-Treatment (°F/hr)	Compliant Material	Interference (in.)	Speed at Failure (rpm)	P/A Stress at Failure (ksi)
33	1.00	2500/23	Platinum	0.001	53,500	38.5
34	1.00	2500/23	Platinum	0.001	60,200	48.7
35	1.00	2500/23	Alumina	0.001	51,000	35.0
36	1.00	2500/23	Alumina	0.001	55,400	41.3

C. OPTIMIZED ATTACHMENT EVALUATION

To further evaluate the optimized attachment and establish the 3-Sigma* lower bound baseline load-carrying capability, additional spin testing of hybrid attachments using the platinum compliant layer was conducted. The 3-Sigma lower bound was desired, as program Milestone I consisted of spin testing the optimized attachment to 100% of the room temperature 3-Sigma lower bound strength of the ceramic.

Subsequently, 12 single-bladed "balanced" attachments similar to the previous assemblies (Figure 22) were fabricated and spin tested at room temperature as tabulated in Table 4. The results of these spin tests were analyzed using Weibull statistics by minimizing the squared deviations in the ultimate stress, as plotted in Figure 24. This distribution indicates a mean stress of 37.4 ksi, a 2-Sigma lower bound of 26.3 ksi, and a 3-Sigma lower bound stress level of 20.5 ksi, above which 99.5% of the failures should occur. These data show less scatter and higher mean and 2-Sigma stress levels than all previous data and are also compatible with turbine engine design requirements for ceramic materials. Thus, the design P/A stress and corresponding rotor speed to be used for program Milestone I spin testing were set at 20.5 ksi and 60,000 rpm, respectively, as discussed in the following paragraphs.

D. COMPLETION OF PROGRAM MILESTONE I

After determining the room temperature design stress level, three ceramic-wrought alloy specimens were successfully spin tested to 100% of this design limit. All of the ceramic pseudoblades received the 23-hr, 2500°F preheat treatment. After attachment upset and bonding, using a ceramic-wrought alloy interference of 0.001 in., the entire ceramic-wrought alloy assemblies were subjected to a heat treatment typical of one necessary to obtain the desired disk properties in the AF2-1DA simulated disk halves. After heat treatment, the attachment assemblies were Zyglo penetrant inspected for cracks; none were observed.

Two of the three specimens spin tested were of a short dummy blade design, as shown in Figure 25, and were spin tested to 60,000 rpm with a P/A stress at the root of the blade of 20.5 ksi. The pseudoblade portion of these short blades were 0.725-in. long, resulting in a tip speed of 2029 ft/sec.

The third attachment specimen was of the standard blade design, shown earlier in Figure 22, and was spin tested to 40,000 rpm with a P/A stress of 20.5 ksi. This longer blade was 1.11-in. long, producing a tip speed of 1487 ft/sec. A summary of this data is tabulated in Table 5.
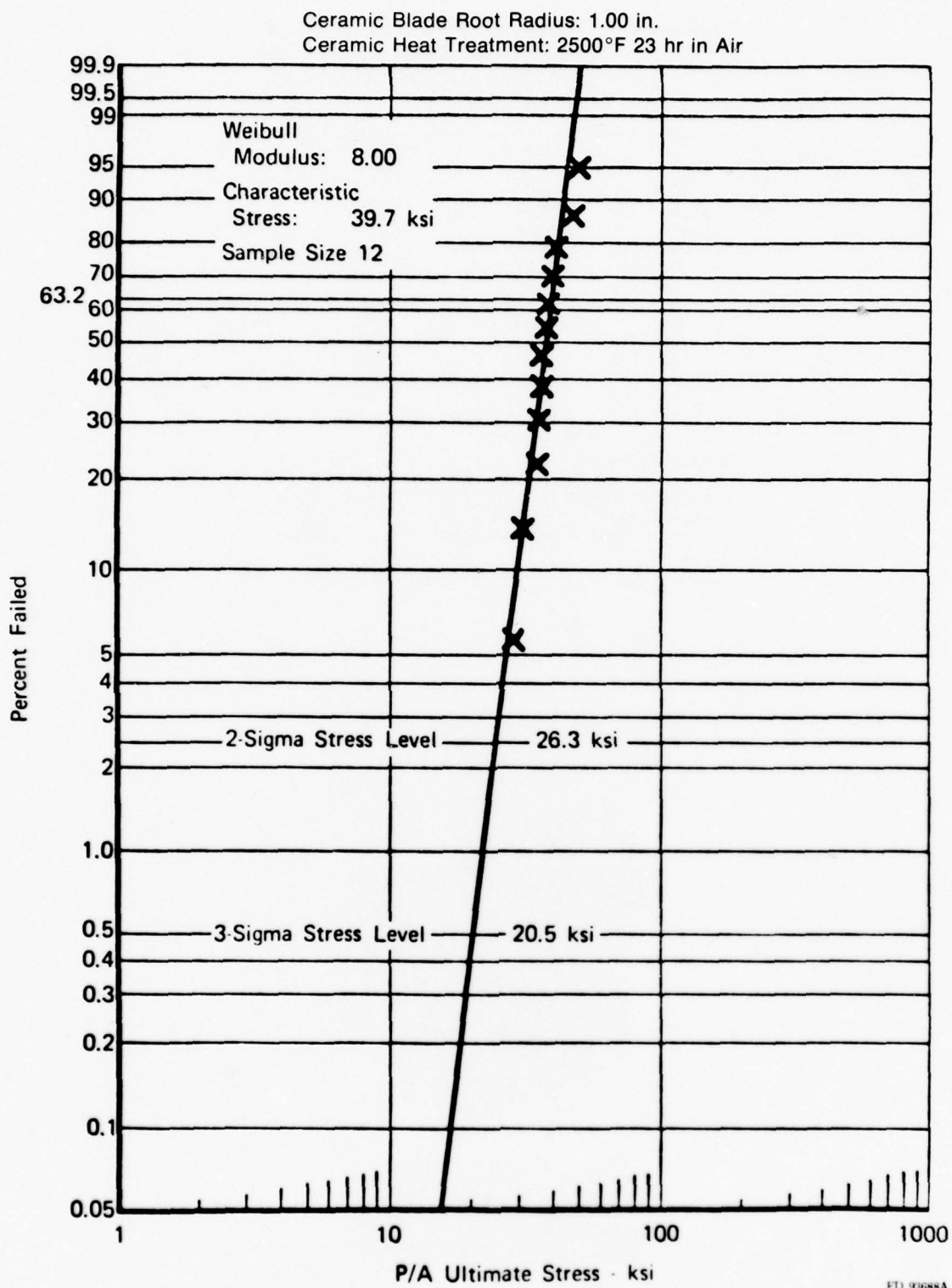
Figure 24. Room-Temperature Spin Test Ultimate Stress Weibull Analysis of Ceramic-Wrought Alloy Attachment Using Platinum Compliant Layer

25

TABLE 4. RESULTS OF ROOM-TEMPERATURE SPIN TESTING CERAMIC-WROUGHT ALLOY ATTACHMENTS

S/N	Speed at Failure (rpm)	P/A Stress at Failure (ksi)
33	53,500	38.5
34	60,200	48.7
37*	58,900	46.7
38	50,800	34.7
39	50,300	34.0
40	46,400	29.0
41	52,300	36.8
42	51,600	35.8
43	54,800	40.4
44	48,000	31.0
45	52,100	36.5
46	53,300	38.2

Compliant Layer:	Platinum
Ceramic Preheat Treatment:	2500°F/23-hr Air
Attachment Design:	Balanced Lug
Root Radius:	1.00 in.
Ceramic-Wrought Alloy Interference:	0.001 in.

*Specimens 35 and 36 used an alumina compliant layer.
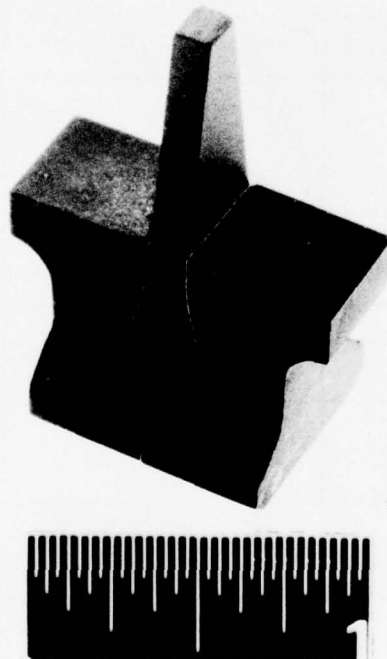
FAE 147374

Figure 25. Short Bladed Ceramic-Wrought Alloy Attachment Specimen Spin Tested to 60,000 rpm, 20.5 ksi

26

TABLE 5.   RESULTS OF ROOM-TEMPERATURE SPIN TESTING CERAMIC-WROUGHT ALLOY ATTACHMENTS TO 100% OF THE DESIGN STRESS FOR MILESTONE I

S/N	Blade Length,* (in.)	Spin Test Speed (rpm)	P/A Stress at Blade Root (ksi)	Tip Speed (ft/sec)
47	0.725	60,000	20.5	2029
48	0.725	60,000	20.5	2029
49	1.11	40,000	20.5	1487

*Blade length does not include the length of the ceramic root.

After spin testing to these speeds and stress levels, all specimens were examined and found in their original prespin condition. In addition to satisfying the requirements of program Milestone I, the successful spin testing of these specimens illustrated the fact that the integrity of the attachment was not sacrificed during the heat treatment of the AF2-1DA wrought alloy.

---

* The 3-Sigma lower bound stress level is that stress above which 99.5% of the specimen failures should occur.

SECTION III

PHASE II — ELEVATED-TEMPERATURE ATTACHMENT CHARACTERIZATION AND ROTOR DEVELOPMENT

The second phase consisted of development and elevated-temperature spin testing of a fully-bladed hybrid rotor conducted in two tasks:

1. Evaluating the forged-diffusion bonded attachment concept in an elevated-temperature environment

2. Demonstrating the feasibility of this attachment concept for a typical small gas turbine rotor application by spin testing a fully pseudobladed rotor at elevated temperature.

An elevated-temperature evaluation of the forged diffusion bonded single attachment was conducted in three subtasks to investigate the load-carrying capability of the attachment. This work was conducted by (1) spin testing a disk containing six individual attachments at 45,000 rpm rotor speed and 2100°F blade temperature, (2) conducting cyclic thermal testing of a single attachment, and (3) continuing ceramic preheat treat development. These efforts demonstrated the ability of the individual attachments to withstand a typical gas turbine thermal environment.

After completing the elevated-temperature evaluation of the single-blade attachment, efforts were directed toward demonstrating the feasibility of a fully-bladed rotor by spin testing at elevated temperature. This was accomplished by (1) designing and fabricating the rotor and spin tooling, (2) spin testing a single pseudobladed rotor for 16 hr beyond the Milestone II test objective of 10 thermomechanical cycles for 50 hr at 45,000 rpm and 2,250°F blade temperature, and (3) spin testing both a 28 and 30 pseudobladed rotor in accordance with the Milestone II spin test requirements. These achievements demonstrated the feasibility of this hybrid attachment concept for typical small gas turbine rotor application.

A. ELEVATED-TEMPERATURE ATTACHMENT EVALUATION

As previously discussed, evaluation of the forged-diffusion bonded single attachment in an elevated-temperature environment was conducted in three subtasks: (1) elevated temperature spin testing of a six-attachment disk, (2) single-attachment cyclic thermal testing, and (3) ceramic-preheat treat development.

1. Single-Attachment Elevated-Temperature Spin Testing

To summarize this effort, an evaluation of the attachment concept at elevated temperature was conducted by spin testing a disk containing six individual attachments. This evaluation was conducted in four stages:

    a. Tooling and Attachment Redesign and Fabrication
    b. Experimental Analysis of Redesigned Rotor and Attachment
    c. Hybrid Attachment Proof and Elevated-Temperature Spin Testing
    d. Rotor Failure Analysis.

An analysis of the tooling previously used for spin testing at room temperature, indicated that a redesign was required for testing at elevated temperatures. To assess the redesigned spin disk and attachment integrity prior to hot spin testing, an experimental analysis was conducted.

28

After completing the experimental analysis, a six-bladed rotor hot spin test was conducted. However, after 3.5 hr at speed and temperature, a rotor failure occurred. A failure analysis was then conducted to determine the mode of failure and is discussed in detail in paragraph d.

a. Tooling and Attachment Redesign and Fabrication

A hot spin test disk was designed to simulate the speeds and rotor size anticipated for small, automotive-type gas turbines. The ceramic-wrought alloy attachment design was also modified to accommodate the redesigned disk. Testing conditions were established at 45,000 rpm rotor speed, 2100°F ceramic blade temperature, and a P/A stress on the ceramic blade root of 15 ksi. The capability of testing up to six-attachment specimens during this test was also incorporated in the disk design.

The hot rotor and attachment specimen designs are illustrated in Figure 26 and a typical attachment specimen after fabrication is shown in Figure 27. It is evident that these new specimens have no balance material as previously used; however, any loads that might cause an undesirable bending moment in the specimen dovetail area would now be balanced by the disk rim loading on the attachment. A schematic of the new rotor design and elevated-temperature spin tooling is shown in Figure 28.

b. Experimental Analysis of Redesigned Rotor and Attachment

Prior to fabrication of the elevated-temperature rotor, an experimental stress analysis was conducted to determine rotor integrity. This analysis consisted of a dynamic photoelastic and experimental strain analysis, strain rupture testing, and a rotor thermal calibration. The dynamic photoelastic analysis and experimental strain analysis were conducted to predict and verify, respectively, the room-temperature localized strain in the most highly stressed areas of the rotor. Strain rupture testing and a thermal calibration were conducted to establish the length of time the rotor could sustain these localized strain levels at the elevated temperatures encountered in the hot spin test. Rotor life prediction was possible by using the strain-rupture testing data to establish a Larsen-Miller type curve for the rotor material. The experimental analysis and thermal calibration results were used with the strain-rupture curve to predict a rotor life of 7 hr at 45,000 rpm and 2100°F blade tip temperature, as discussed in the following paragraphs.

First, to locate the most highly stressed areas around the dovetail slots, a dynamic photoelastic analysis was performed. A schematic of the setup used to perform this analysis is shown in Figure 29. Using this setup, the stress distribution can be seen, and the highly stressed areas can be identified, as shown in Figure 30. These highly stressed areas were analyzed in the photoelastic model, then transformed to prototype stresses in the actual rotor.

Based on this analysis, the predicted room temperature strain in the most highly stressed location of the dovetail would be 0.0051 in./in. at 45,000 rpm. This strain level was considered high for the anticipated disk operating temperature of 1500°F but acceptable for a short-term test. To establish the length of time the rotor could sustain this localized strain level at elevated temperature, an additional experimental analysis was conducted.

For this analysis, flat strain rupture specimens simulating the area and stresses between the rotor dovetail slots were fabricated, as shown in Figure 31a. Initially, one specimen was strain gaged and a strain vs load plot established, as shown in Figure 31b. The load in this case simulated the P/A loading at increasing rotor speeds produced by both the rotor lug mass and the ceramic-wrought alloy attachment. These flat strain rupture specimens were then tested to failure at various temperatures and loads. The loads at these elevated temperatures were correlated to the room-temperature strain, and a strain vs time and temperature plot was established, as shown in Figure 31c.

29

FE 14754

Figure 27. Redesigned Ceramic-Wrought Alloy Attachment
Test Specimen After Fabrication

Rotor

Ceramic
Pseudoblades

Wrought Alloy
Simulated Disk

Dovetail Slots for
Additional Attachments

Instrumentation
Routing Holes

Ceramic Pseudoblade

Rotor

FD 95509

Figure 26. Elevated-Temperature Rotor Tooling and
Ceramic-Wrought Alloy Attachment Design

30
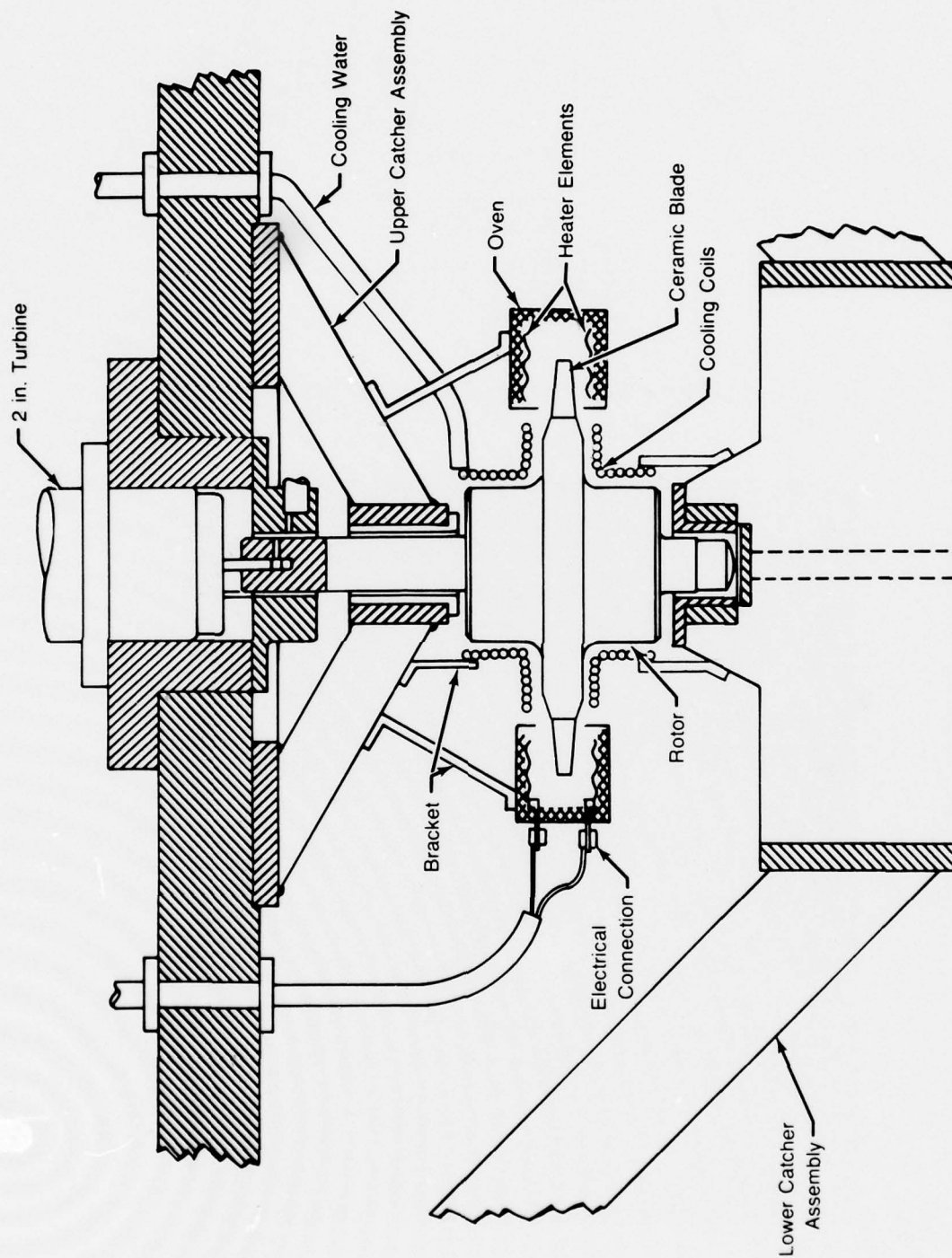
FD 96510

Figure 28. Single-Attachment Spin Tooling and Oven Assembly
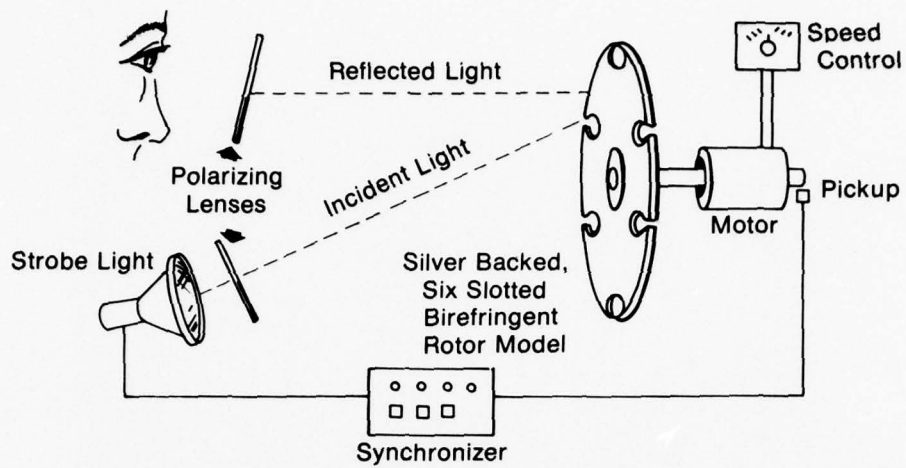
FD 93691B

Figure 29. Schematic of the Photoelastic Analysis of the Elevated-Temperature Rotor
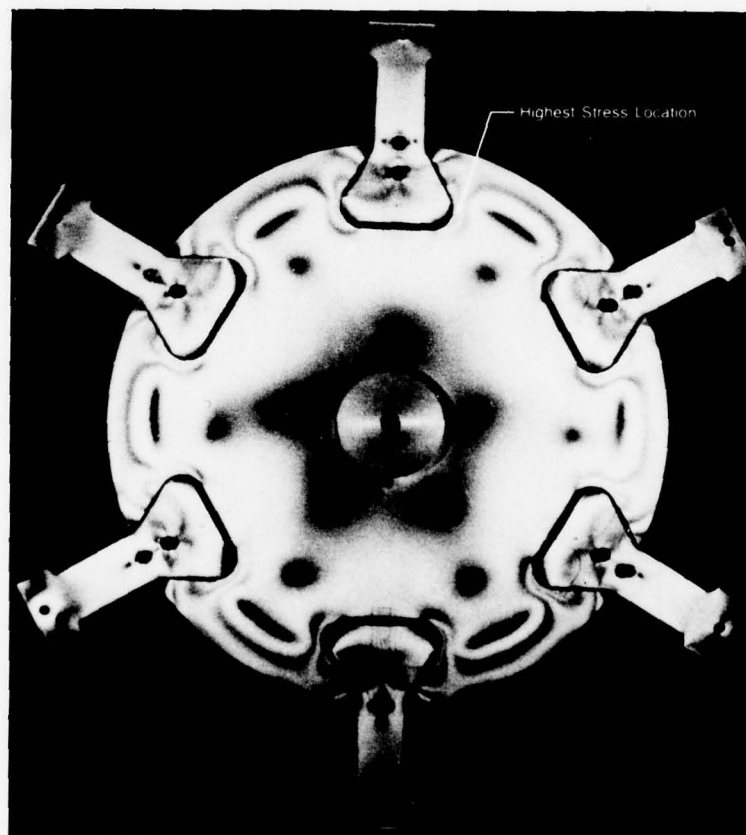
KFE 147318B

Figure 30. Photoelastic Stress Distribution of Six-Slotted Rotor
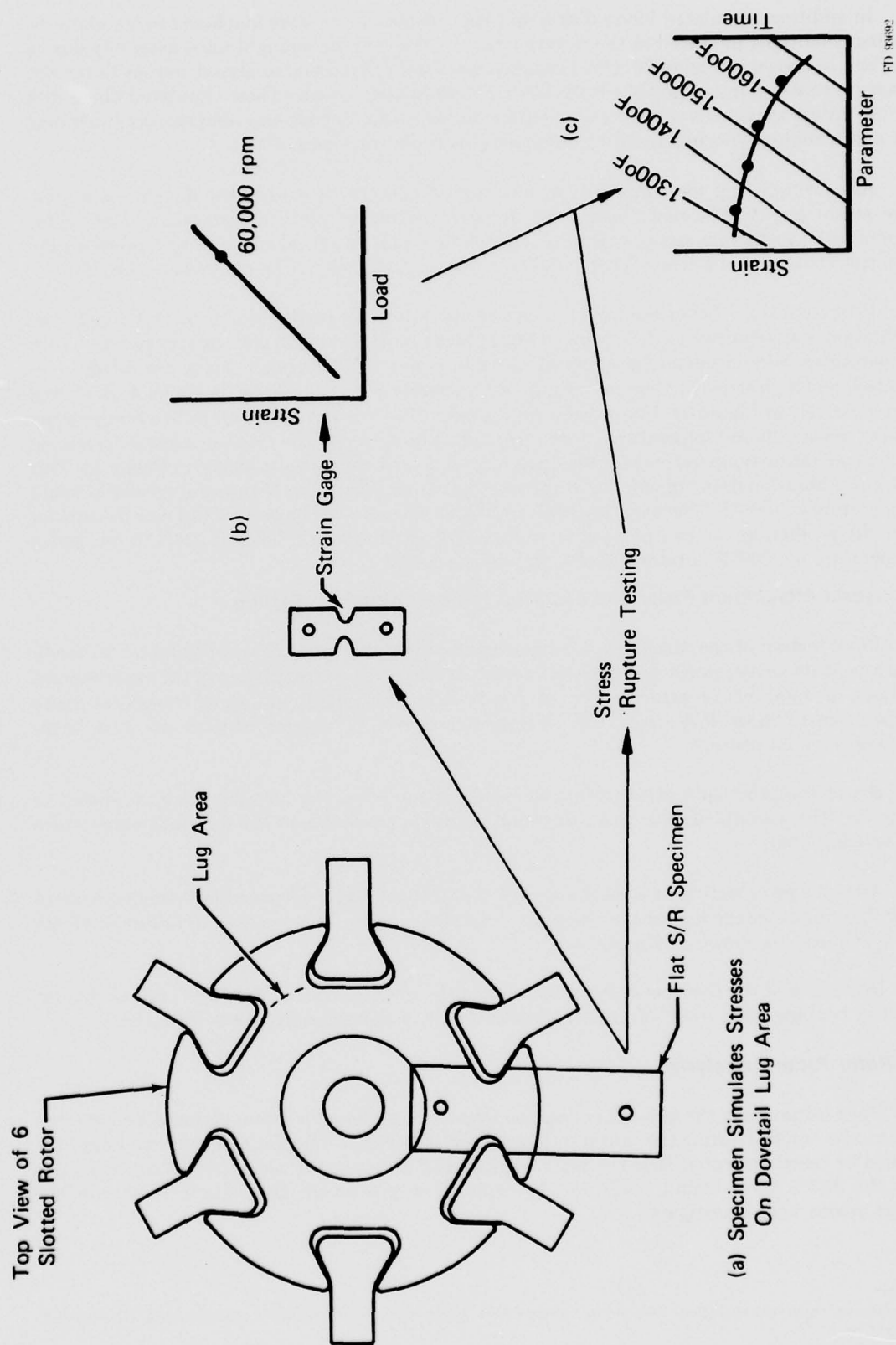
Figure 31. Flat Stress-Rupture Specimen and Analysis of Dovetail Lug Area

In addition, simulated blade-disk strain-rupture specimens were machined to simulate the loading conditions produced in the dovetail area by the ceramic-wrought alloy assembly during rotation, as shown in Figure 32. One specimen was strain gaged and analyzed similar to the flat strain rupture specimens and the loads were related to rotor speeds. These simulated blade-disk strain-rupture specimens were tested to failure and all strain vs time and temperature (including flat strain rupture specimen) data were plotted as shown in Figure 33.

After completing rotor fabrication, all areas of concern, primarily the dovetail slot area, were strain gaged. The disk, loaded by dummy weights in place of ceramic-wrought alloy attachments, was strain analyzed during rotation to obtain an actual strain vs rpm relationship. This test confirmed the strain level of 0.005 in./in. as predicted by the photoelastic analysis.

Prior to using the experimental analysis for rotor life prediction, a rotor temperature calibration was required to determine ceramic blade vs attachment area temperatures. These temperatures were obtained by applying thermocouples to the ceramic blade tip, blade root, dovetail, and high stressed areas of the spin test assembly as illustrated by locations A, B, C, and D, respectively in Figure 34. Using a slip ring to relay the thermocouple voltage to a temperature display device, these temperatures were recorded while spinning the rotor at a low rotor speed. Typical operating temperatures for the areas of primary concern are also shown in Figure 34. This thermal calibration data indicated that the most highly stressed areas of the rotor dovetails would be operating at 1500°F. The experimental strain analysis data of Figure 33 could now be used for rotor life prediction. As can be seen from Figure 33, with a strain level of 0.005 in./in. and a temperature of 1500°F, a rotor life of 7 hr. was predicted.

c. Hybrid Attachment Proof and Elevated-Temperature Spin Testing

Proof testing of the attachment configuration shown in Figure 27 was conducted to verify attachment integrity prior to elevated-temperature testing. Upon completion of the experimental analysis, a total of 12 attachment specimens were fabricated and proof tested at room temperature to 26 ksi P/A stress (the 2-Sigma stress level as determined from previous room-temperature spin testing).

Six of the proof spin attachments were then mounted in the hot spin rotor, as shown in Figure 35. The assembled rotor was suspended in the spin facility and the elevated-temperature test was initiated.

After 3.5 hr of testing at a rotor speed of 45,000 rpm* and a ceramic blade temperature of 2100°F, a failure in the lug area of the rotor dovetail occurred. This resulted in failure of all six test specimens, as shown in Figure 36.

Inspection of the five specimens remaining in the rotor indicated that these ceramic blades failed in bending, as a result of impact. Subsequently, a failure analysis was initiated.

d. Rotor Failure Analysis

Upon initiation of the failure analysis, an inspection of the rotor revealed that a second rotor lug had also cracked during the spin test, but did not fail (Figure 37). The fact that two rotor lugs cracked or failed indicated that the rotor was actually closer to the mean life condition rather than the 97.5% lower bound condition. To explain the premature disk failure, three possible failure modes were investigated.

---

* In addition, these test conditions resulted in a desired P/A blade stress of 15 ksi and a ceramic blade tip speed of 1305 ft/sec.
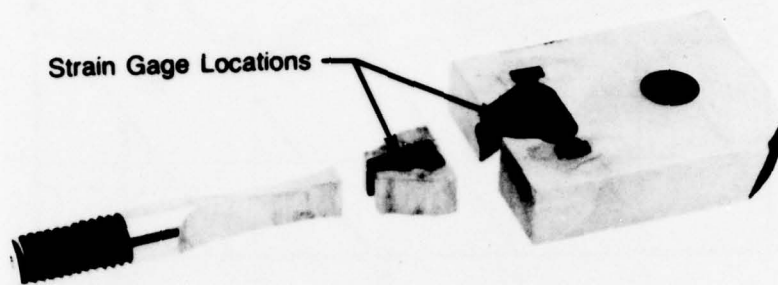
Strain Gage Locations

FAE 147486
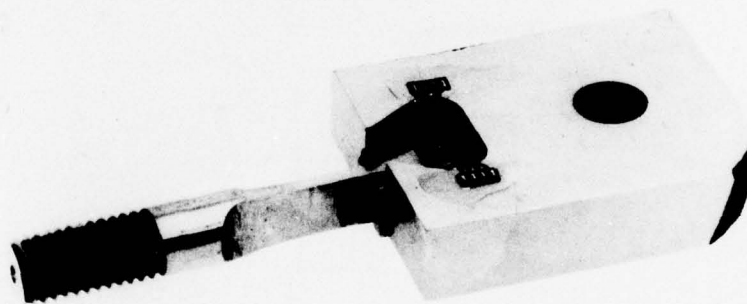
FAE 147487

FD 95512

Figure 32. Exploded and Assembled View of Simulated Disk and Blade
Strain Rupture Specimen

35
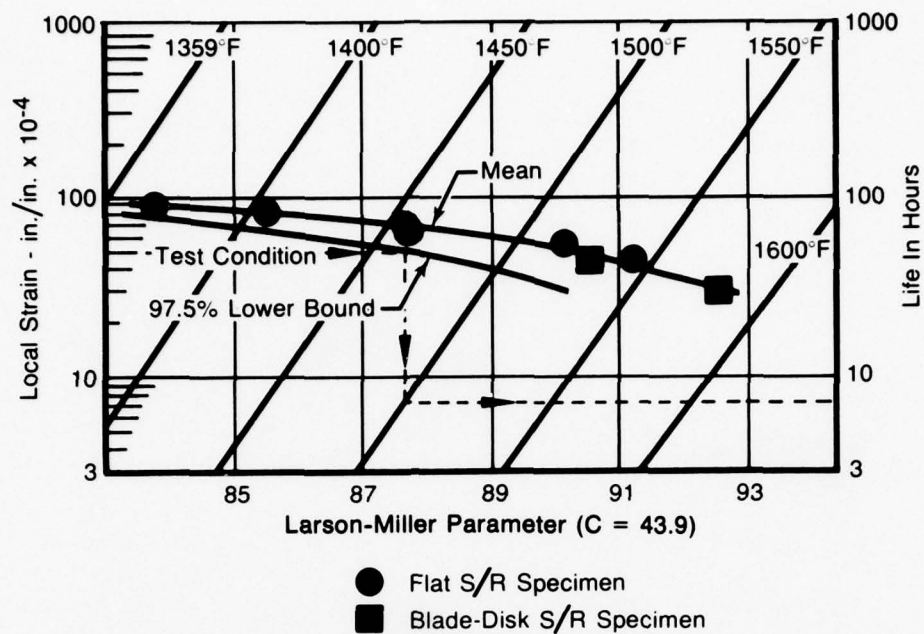
FD 95513

Figure 33. Results of Hot Spin Rotor Experimental Analysis

Test Temperatures

Location	Average Temperature °F
A	2100
B	1550
C	1550
D	1500
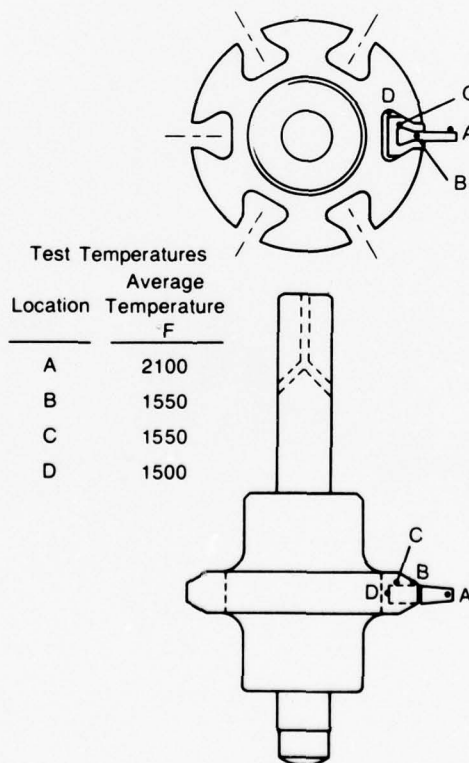
FD 95514

Figure 34. Typical Thermocouple Locations and Test Temperatures for Elevated-Temperature Spin Test

36

FAE 148144A

Figure 36. Elevated-Temperature Rotor Failure

FE 147846

Figure 35. Hot Spin Rotor With Ceramic-Wrought Alloy Attachment Specimens in Place

37

FAL 36862

FD 97814

FAL 36863

Figure 37. Closeup of Crack in Lug Adjacent to Failed Lug on Hot Spin Rotor

38

The first suspect failure cause was an overtemperature condition in the rotor rim. Figure 38 shows that any rim temperatures over 1500°F would severely decrease the rotor life. To investigate this overtemperature possibility, a metallographic examination of the rotor periphery was conducted. The resulting microstructure photographs were compared with existing microstructure data on IN 100 material receiving the same processing and heat treatment as the hot rotor. Using this comparison as a temperature indicator, Figures 39 and 40 illustrated the microstructure similarity between the rotor rim and a stress specimen tested at 1500°F. This comparison suggested that an overtemperature condition was not the primary cause of premature rotor failure.

The second suspected failure cause investigated was a fatigue-induced reduction in the stress rupture properties of the IN 100 rotor material. This failure mode was suspected because of the rotor speed variation which resulted as the rotor was cycled between the upper and lower speed limits set on the speed control for the spin pit. Although the rotor speed changes produced a stress variation of only 1 to 2%, this cyclic fatigue was believed sufficient to reduce the stress rupture life of the IN 100 rotor material at this temperature.

To verify this possibility, five IN 100 uniaxial test specimens were fabricated, heat treated, and tested under high R ratio small stress excitation conditions, similar to those of the hot spin test. Specifically, specimens were tested at 1500°F with the load varying between 64 and 65 ksi at 5 and 20 cpm. These frequencies were chosen to cover the range of frequencies the spin rotor experienced during the elevated temperature spin test.

The results of this testing as a comparison between the steady-state stess rupture life and the steady-state stress rupture plus high R-ratio, small-stress excitation life are shown in Figure 41. This figure illustrates that at 1500°F (test rotor conditions) the superposition of the small excitation stress reduces the rupture life by approximately 50%. Thus, this fatigue-induced reduction in the stress-rupture life is considered a primary source of the premature failure problem.

The third probable cause investigated was a thermally-induced overstress condition in the rotor rim. This condition was believed to have been the result of "locking" each attachment specimen in its respective dovetail slot with lock tabs, effectively forming a continuous rotor rim. The "hot" rim tended to thermally expand during the spin testing. It was restricted by the cooler rotor hub, which resulted in an increased tensile stress in the dovetail area as illustrated in Figure 42. To quantify this additional stress, a second thermal calibration and a thermal strain analysis were conducted.

Since the initial thermal calibration only measured the attachment/rotor thermal gradient, a second thermal calibration was conducted to measure the thermal gradient between the rotor rim and the rear portion of the rotor attachment slot (locations A and C, respectively, in Figure 43). The results of this second calibration (also shown in Figure 43) indicated a rotor rim thermal gradient of 170°F. Although the temperatures obtained were below the actual temperatures of the spin test, sufficient data were obtained during this calibration to substantiate this gradient as representative of the actual spin test conditions.

A thermal strain analysis was conducted to measure the resultant additional strain produced by the 170°F thermal gradient.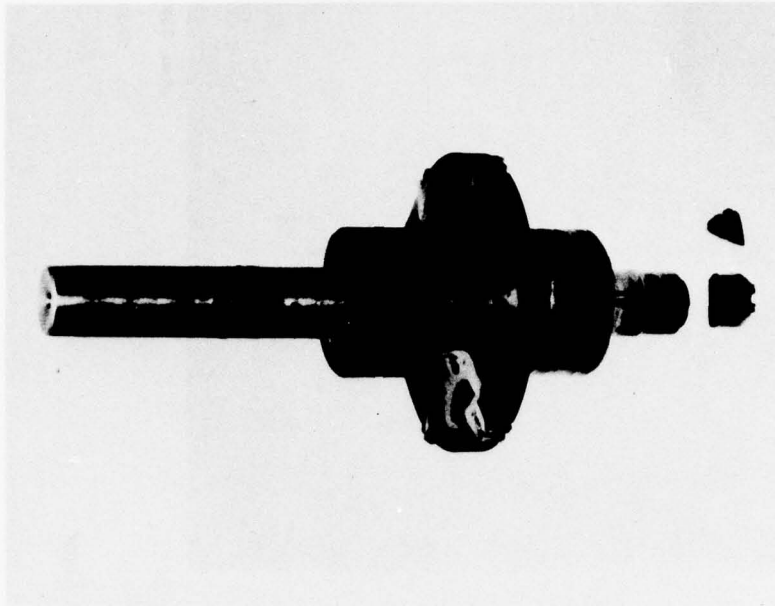 To perform this test, rotor strain in the attachment slot was monitored while heating the rotor rim and cooling the rotor bore to produce the desired thermal gradient. The test results are illustrated in Figure 44.

These test results indicate that the 170°F thermal gradient produced an additional tensile strain of 1500 micro in./in. in the dovetail, or 30% more strain than was originally used in the 7-hr rotor life prediction. Thus, both the fatigue-induced decrease in material stress rupture capability and the thermally induced stress condition contributed to premature rotor failure.

39
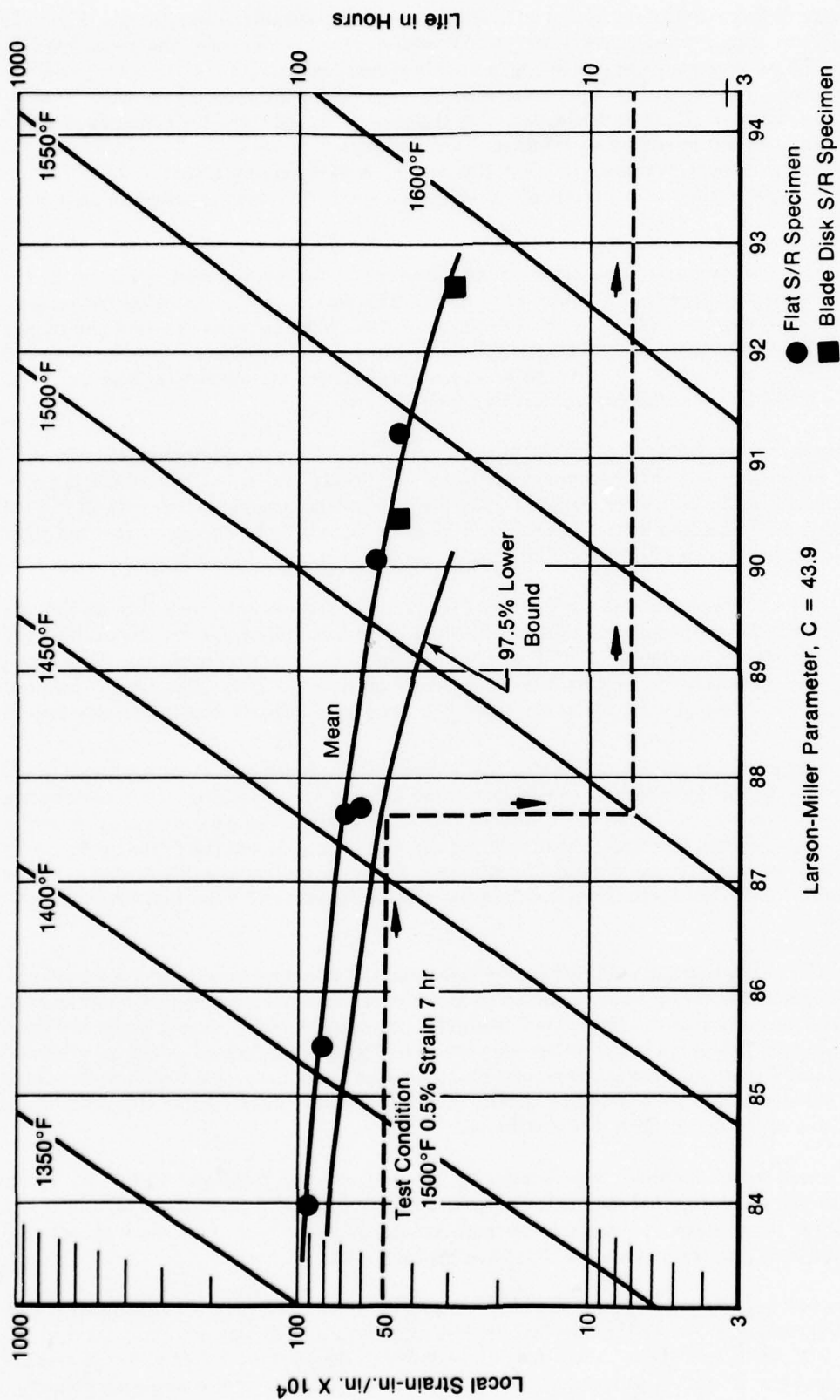
Figure 38. Results of Hot Spin Rotor Experimental Analysis

FD 95813

40
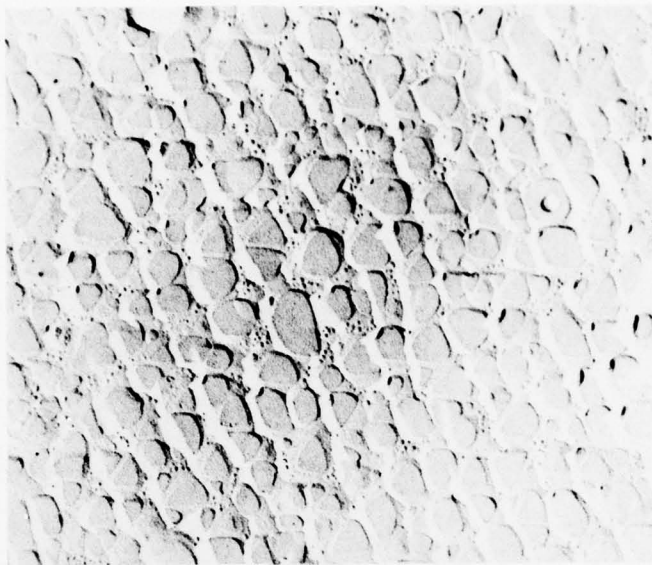
Mag: 20,000X   FD 97815A

Figure 39. Electron Photomicrograph of IN 100 Hot Spin Rotor Rim
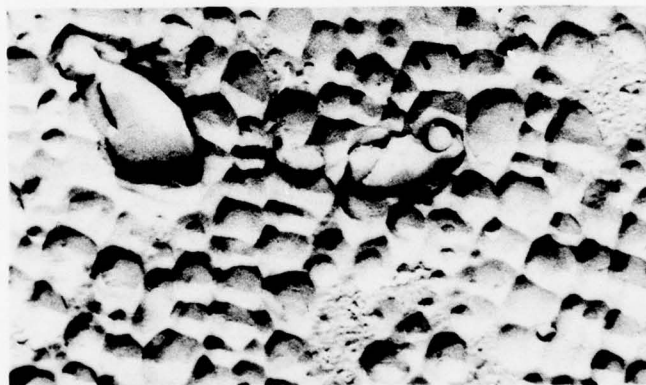
Mag: 20,000X   FD 140377

Figure 40. Electron Photomicrograph of IN 100 Stress-Rupture Specimen Tested at 1500°F

41
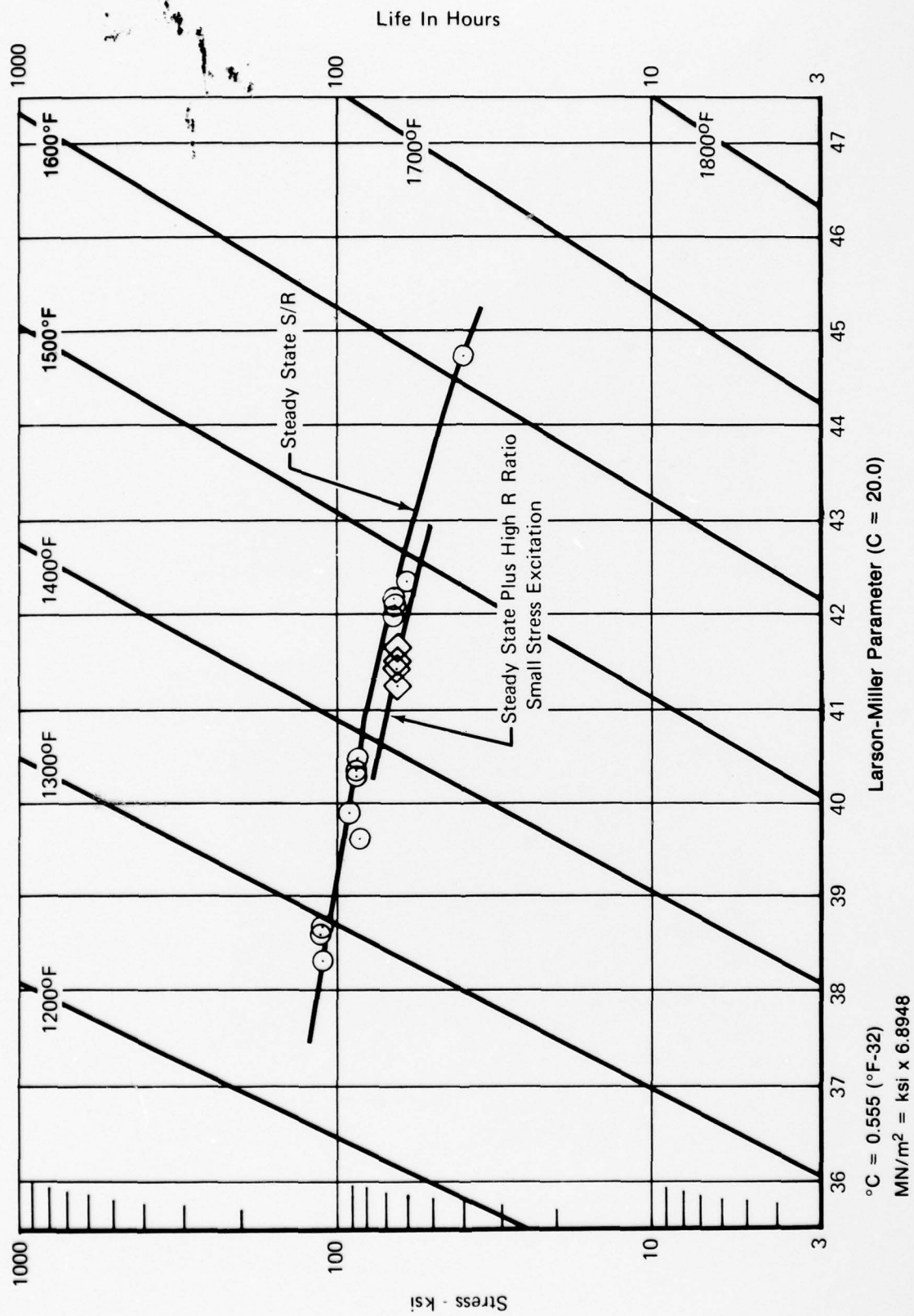
Figure 41. *Effect of High R Ratio Small Stress Excitation on Stress-Rupture Life of IN 100 Rotor*

42

① Tabs "Lock" Each
Attachment Specimen
In Place

② "Hot" Rim and Cooler Hub
Produce Additional Tensile
Stresses at the Maximum
Stress Location
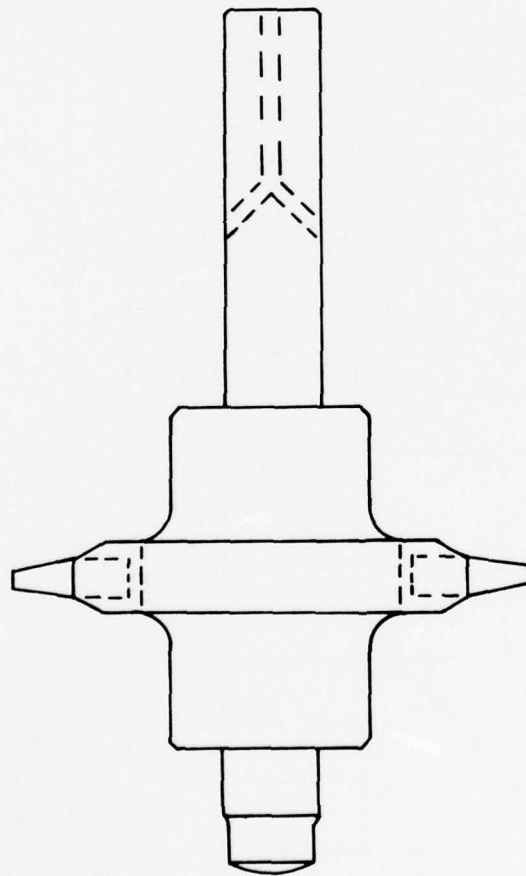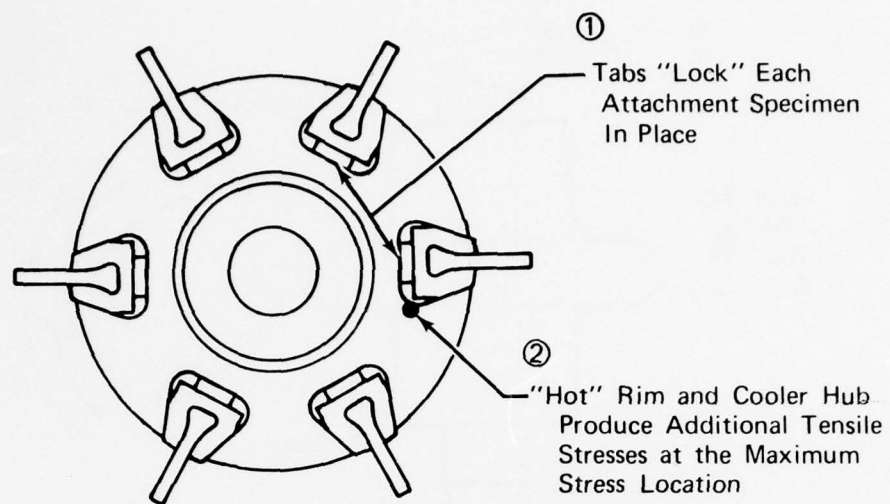
FD 97818

Figure 42. Thermally-Induced Stress in Rotor

43

Post Spin Test Calibration

A	1172°F
B	1093°F
C	1002°F

T/C Locations A. B, and C

Rotor

Rotor Rim
Thermal
Gradient

A-C = 170°F

Ceramic
Blade

Rotor

C B A

C B A
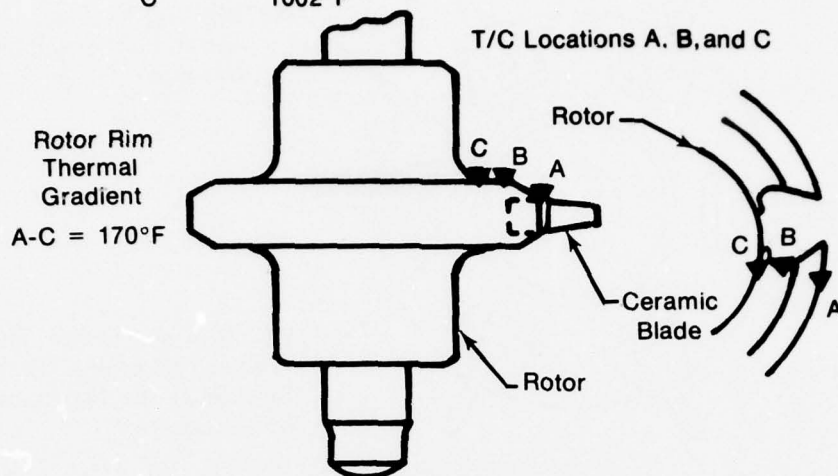
FD 97819

Figure 43. Results of Thermal Calibration
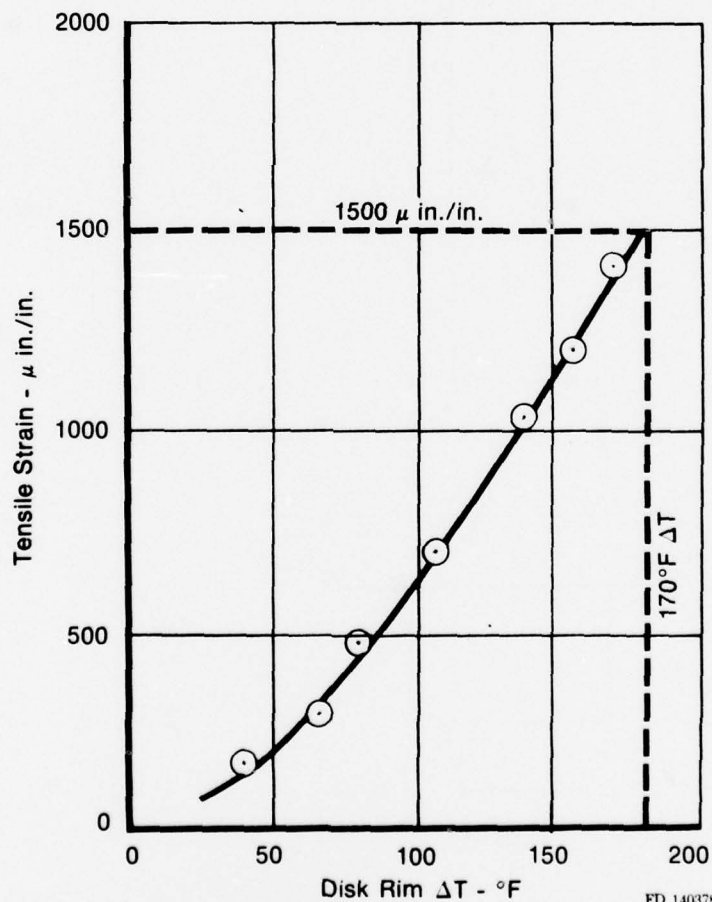
Figure 44. Results of Thermal Gradient Stress Analysis

44

The results of both these analyses are summarized in Figure 45. This graph illustrates the effect of lowering the original stress rupture life by 50% due to the high R ratio small stress excitation and the effect of operating at a strain level of 0.65% due to the additional thermal stress. As previously mentioned, the rotor was actually closer to the mean life condition rather than the 97.5% lower bound condition initially used to predict rotor life. By using this lowered curve and the 0.65% strain level (Figure 45), the mean rotor life of only 3.5 hr was verified. Thus, these two conditions were adequate to produce the rotor failure which occurred.

2. Cyclic Thermal Testing

To further evaluate the hybrid attachment concept, cyclic thermal shock and elevated-temperature bend tests were conducted to investigate the ability of the hybrid attachment to withstand the thermal shock and gas load stresses associated with a typical gas turbine thermal cycle.

Cyclic thermal-fatigue testing was conducted using the test specimen shown in Figure 46, by alternately exposing an instrumented attachment to hot gases of two different temperatures and cycling the ceramic blade temperature between 2200 and 1300°F. The dwell period at each temperature was 60 sec to allow blade temperature stabilization.

Testing was planned for up to 500 thermal cycles or until ceramic or wrought alloy cracking occurred. During testing, the attachment was inspected after the completion of each 25 cycles. Upon completion of 500 thermal cycles no cracking had been observed. Therefore, sufficient confidence in the attachment integrity was gained for completing all cyclic requirements, within the scope of the program, and testing was terminated.

An elevated-temperature bend test was also conducted on a ceramic-wrought alloy attachment specimen to illustrate any potential problems that might result from gas bending loads on the ceramic blade during engine operation. This test was not conducted to determine materials or design capabilities but to point out any possible problems that might need additional study. To conduct this test, one ceramic-wrought alloy specimen was mounted in a broached fixture block and a 30-lb side load was applied on the blade tip. This load produced a bending moment of 30 in./lb on the blade and a bending stress on the ceramic surface of 28.8 ksi. The assembly was then heated to 1475°F using Quartzline heating lamps. After 30 hr at this condition, no sign of attachment deterioration was observed. At this point the load was increased to 60 lb, producing a moment and bending stress of 60 in./lb and 57.6 ksi, respectively. The test was allowed to run for 100 additional hours. The specimen was again inspected and no attachment problems were noted. Therefore, the test was discontinued.

It was concluded from this test that bending stresses on the attachment should not present any formidable problems in the ceramic-wrought alloy interface area.

3. Ceramic Preheat Treatment Development

During Phase II, testing conducted on NC132 silicon nitride by United Technologies Research Center (UTRC) (Reference 1) revealed that an oxidizing heat treatment prior to testing drastically reduced the impact strength of the material. Additional bend testing conducted by Westinghouse (Reference 2) supported these results. Since this data was in contrast to the heat treatment results obtained earlier in this program, in which the oxidation was thought to "heal" (or alleviate) any possible surface machining cracks, additional tests were performed to reinvestigate these results.
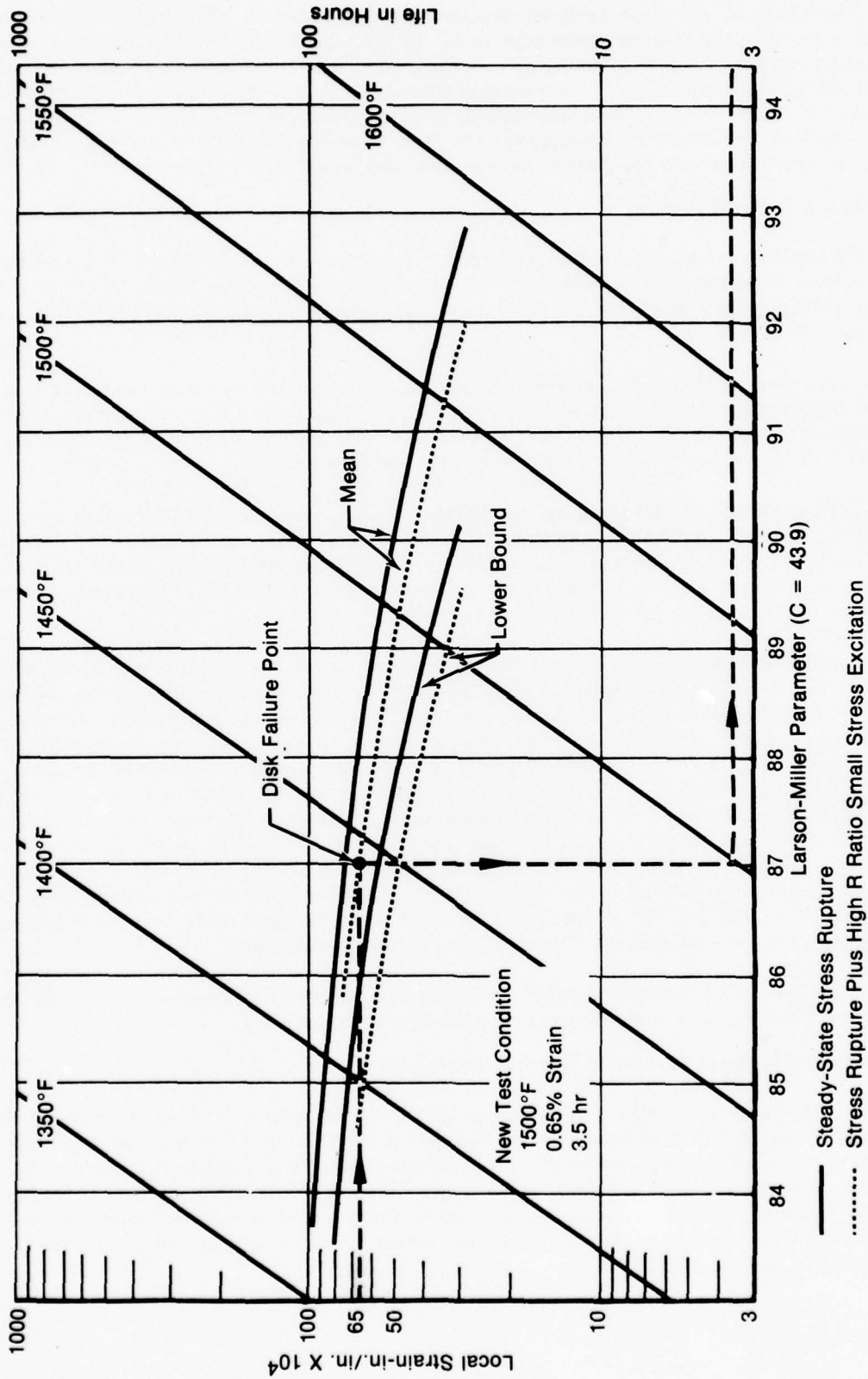
Figure 45. Results of Hot Spin Rotor Failure Analysis

FD 95821

46
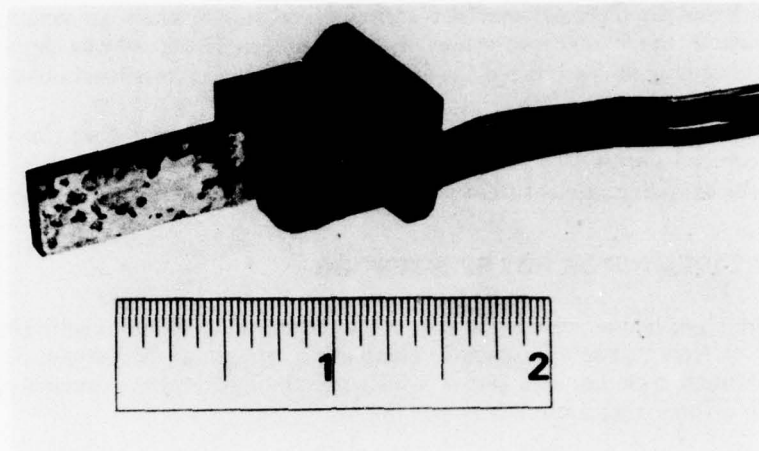
FD 91887

*Figure 46. Thermocoupled Ceramic-Wrought Alloy Attachment
Ready for Thermal Shock Test Calibration*

Toward this end, testing was conducted to determine whether the NC132 silicon nitride used in this program would suffer the same properties degradation observed by others. For this study, rectangular impact specimens were machined, polished, and heat treated using the same procedures used in fabricating pseudoblades for attachment spin testing. These specimens were then subjected to room-temperature Charpy impact tests at UTRC. Although the number of samples tested was not enough to obtain an accurate statistical conclusion, the results of these tests confirmed the decrease in impact strength observed by others.

To determine whether the oxidation surface effect would also affect the tensile strength of the silicon nitride material, these attachment specimens, using as-ground and polished ceramic pseudoblades, were fabricated and spin tested at room temperature. Except for not being heat treated, these specimens were similar to those used to establish the 37.4 ksi mean and 26.3 ksi 2-Sigma lower bound room-temperature ultimate-stress capability of the hybrid attachment of program Milestone I. Results of spin testing these three specimens are shown in Table 6.

TABLE 6. RESULTS OF ROOM TEM-
PERATURE SPIN TESTING
CERAMIC-WROUGHT ALLOY
ATTACHMENTS USING AS
GROUND AND POLISHED
CERAMIC BLADES

S/N	Maximum Speed Obtained (rpm)	Maximum P/A Stress Reached (ksi)	Results
47	70,000	63.2	No failure
48	60,200	46.8	Failure
49	70,000	63.2	No failure*

Compliant Layer: Platinum
Root Radius: 1.00 in.

* Failure occurred on slowdown when spin rotor hit catcher
bushing.

47

The data listed in Table 6 was not sufficient to substantiate an accurate statistical conclusion. However, the 70,000 rpm achieved for specimens 47 and 49 was the maximum safe speed of the spin tooling and produced the highest P/A ceramic stress level obtained thus far.

It was concluded from the testing, as well as from the literature, that this oxidizing heat treatment was indeed harmful to the impact resistance and tensile strength of the material. Consequently, the oxidizing preheat treatment of the ceramic was discontinued for the remainder of Phase II.

B. PSEUDOBLADED ROTOR HOT SPIN TESTING

With completion of the initial hot spin rotor failure analysis and cyclic thermal testing, program efforts were directed toward completing program Milestone II, the 50-hr, 10 thermomechanical cycle hot spin test of a fully pseudobladed rotor. A review of the program plan resulted in a three-task approach consisting of:

1. Design and Fabrication of Rotors and Tooling Components
2. Single Pseudoblade Elevated Temperature Spin Test
3. Fully Pseudobladed Rotor, Elevated-Temperature (Milestone II) Spin Test.

Details of this effort are discussed in the following sections.

1. Design and Fabrication of Rotor and Tooling Components

During this task, all rotors, ceramic blades, and tooling to be used in the planned elevated-temperature characterization and spin testing were designed and fabricated. The resultant design of the fully-bladed rotor, the reuseable spin tooling and ceramic pseudoblade in cross section is illustrated in Figure 47. In addition, a two-dimensional analytical stress analysis of the fully-bladed rotor and spin tooling was conducted.

The rotor was designed with a circumferential dovetail root attachment incorporating the upset/diffusion bond fabrication approach. As discussed in Phase I, this fabrication approach was chosen because of the lower ceramic root and disk rim stresses associated with this approach than would be attained using a conventional axial root attachment, particularly in a small multibladed turbine rotor application.

In addition to the fully-bladed rotor, a single-blade rotor was designed to spin test individual ceramic blades at elevated temperature.

The resultant ceramic blade design, illustrated in Figure 48, consisted of a flat, paddle-like, platform pseudoblade which could be machined using conventional grinding techniques. The pseudoblade design was chosen over an airfoil design because at that time the high cost of ceramic airfoil fabrication was economically beyond the scope of this contract. The root radius for this blade design was 0.300 in. rather than the 1.00-in. radius used in much of the attachment development. This 0.300-in. root radius was chosen for two reasons. First, as illustrated in Figure 49, to produce the equivalent effective ceramic load-bearing area* with a 1.00-in. root radius blade, a longer ceramic blade root was required. The dovetail bearing surface width was determined by the radial location of the circumferential dovetail root, and thus, was the same for the 0.300- and 1.00-in. radius root configurations. Consequently, the effective bearing surface height, h, had to be equal between the two configurations to produce an equally effective dovetail bearing area, and a longer ceramic blade root was required for the 1.00-in. root radius blade.

---

* The effective load-bearing area is the effective area over which the ceramic blade bearing loads are distributed. Numerically, the effective load-bearing area is the product of the bearing surface effective height, h (Figure 50), and the bearing surface width.

Thus, some of the structural portion of the wrought alloy disk had to be sacrificed for the longer dovetail root. Additionally, the smaller dovetail root of the 0.300-in. radius configuration would result in lower disk and dovetail root stresses during spin testing.
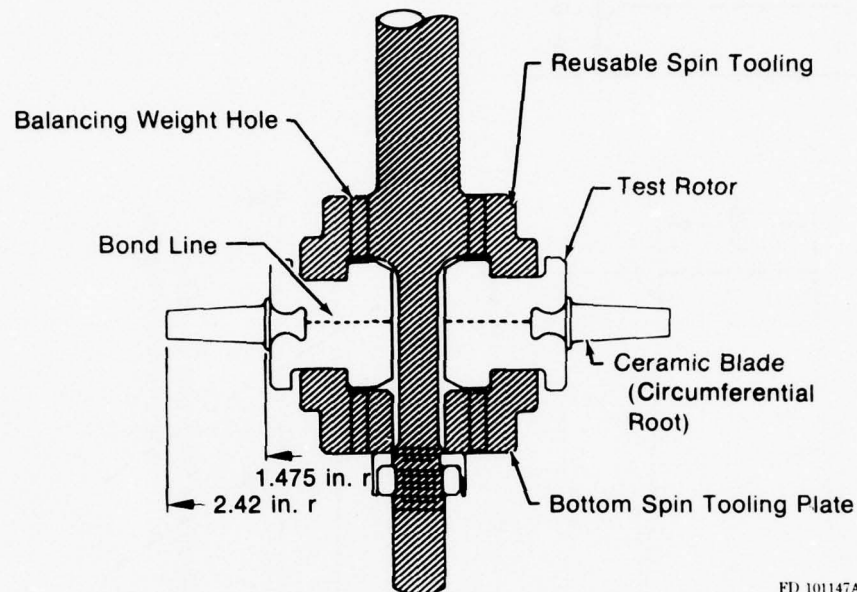
FD 101147A

Figure 47. Spin Tooling and Rotor

Although previous spin testing did not show any advantage of the 1.00-in. root radius over the 0.500-in. root radius configuration, an assumption to this effect could not be made for the 0.300-in. root radius configuration. To investigate the load-carrying capability of the 0.300-in. root radius configuration, eight flat blades (similar to Figure 46) were fabricated and spin tested to failure using the room temperature spin tooling. These blades were not preheat treated, but were in as-ground and polished condition. The results of testing these specimens are tabulated in Table 7. A Weibull analysis of this data is also shown in Figure 50. Results of these tests were actually better than results of any previous spin testing. The 3-Sigma stress level of 39 ksi was a 90% increase over the 20.5 ksi 3-Sigma stress level previously attained in room temperature testing of 1.00-in. root radius blades. This increase in stress capability was attributed to the absence of any ceramic surface degradation due to oxidation and also to improve attachment fabrication techniques, rather than to a change in the root radius. These results substantiated the 0.300-in. root radius as a viable design for future testing.

49
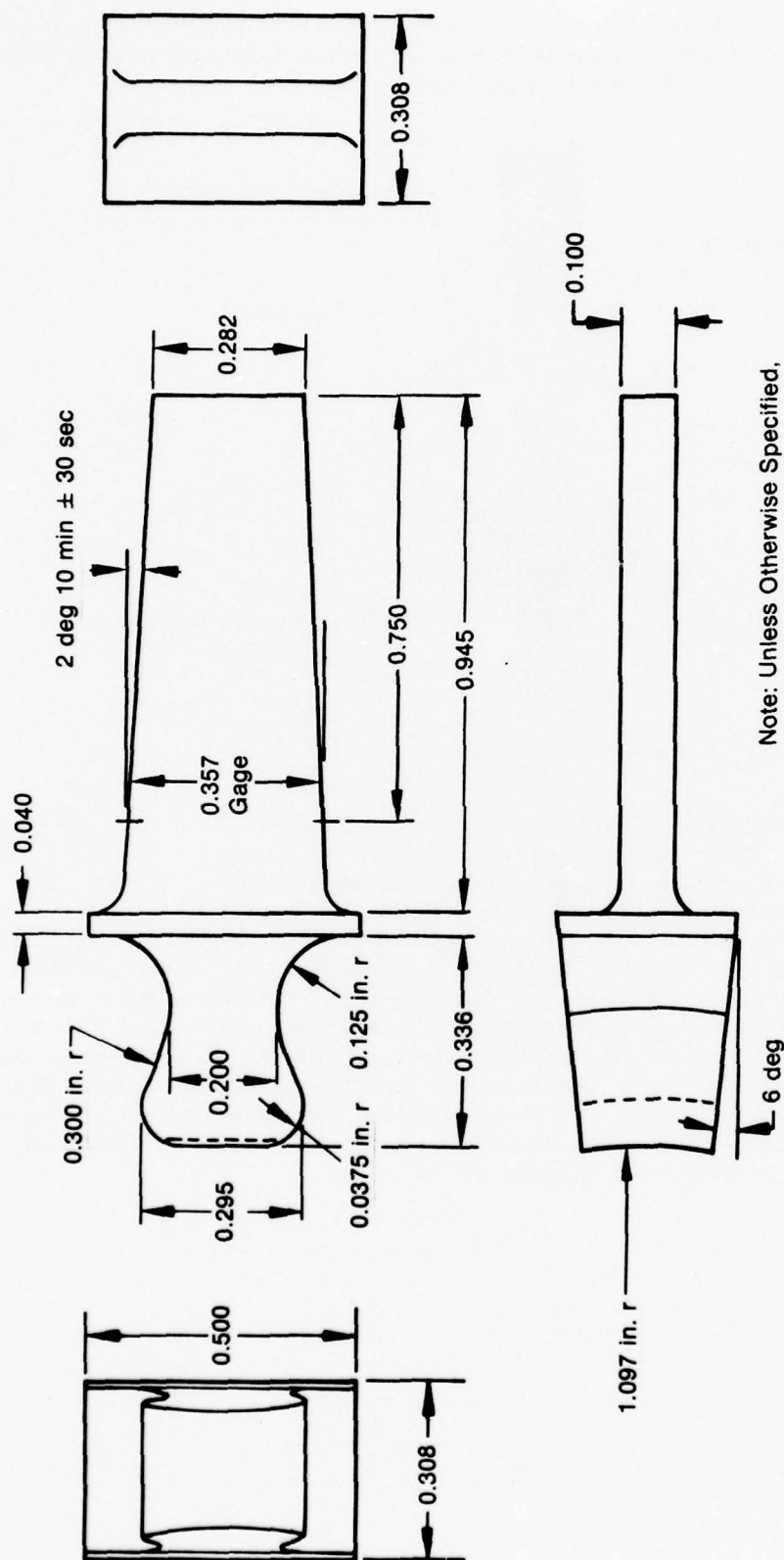
Figure 48. Circumferential Root Ceramic Pseudoblade
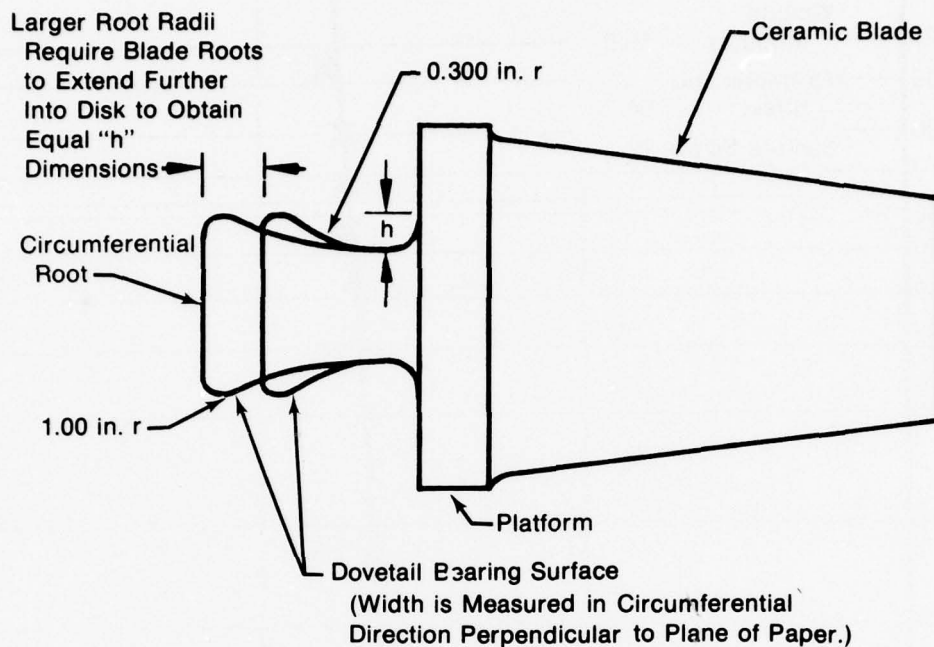
Figure 49. Effects of Root Radius on Root Length

TABLE 7. RESULTS OF ROOM-TEM-
PERATURE SPIN TESTING
CERAMIC-WROUGHT
ATTACHMENTS USING A
0.300-IN. ROOT RADIUS
BLADE

S/N	Speed at Failure (rpm)	P/A Stress at Failure (ksi)
50	59,300	55.5
51	55,500	48.6
52	57,000	51.3
53	57,300	51.8
54	56,400	50.2
55	63,300	63.2
56	58,100	53.3
57	56,900	51.1
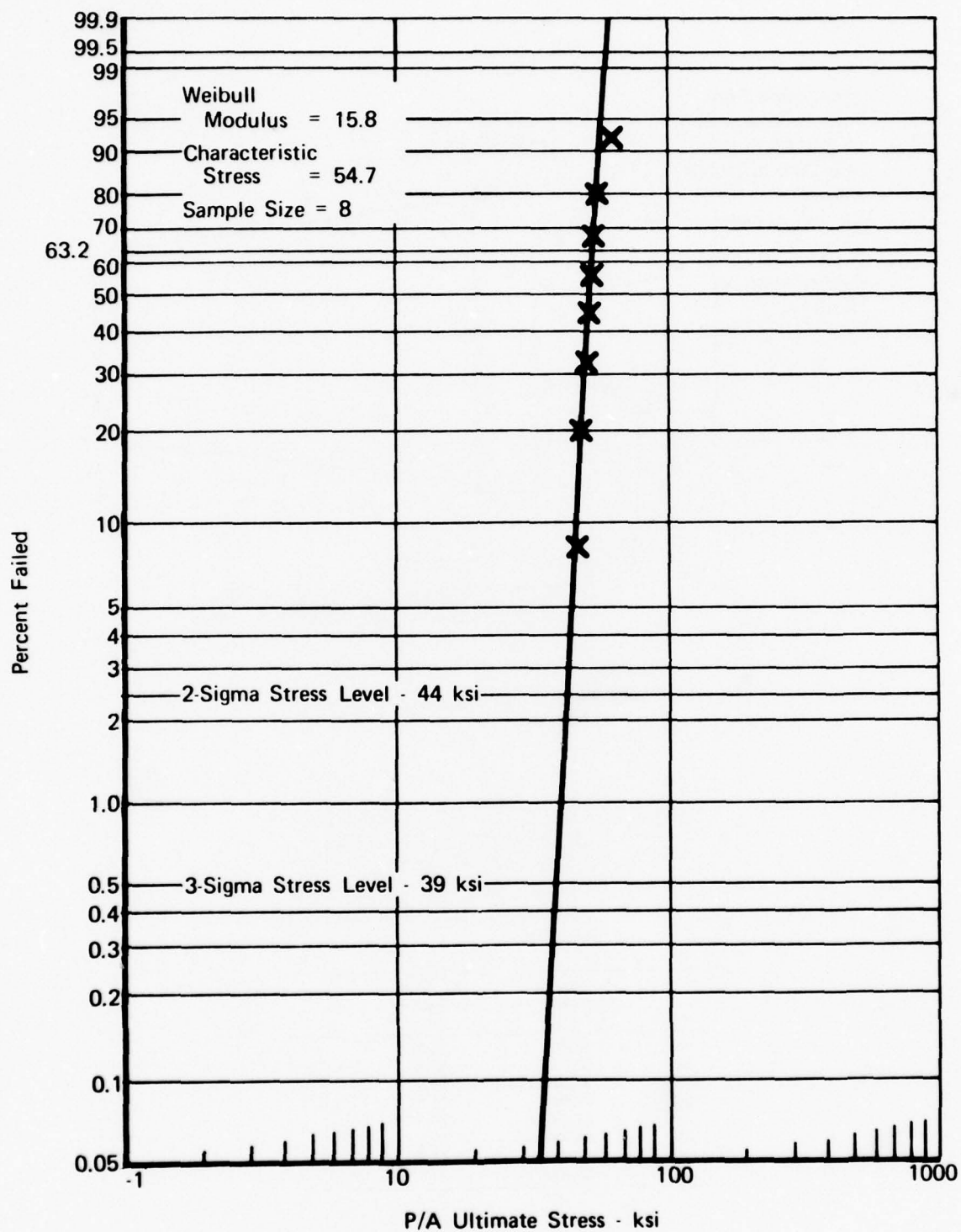
Figure 50. *Room-Temperature Spin Test Weibull Analysis (Ultimate Stress of Ceramic-Wrought Alloy Attachment Using 0.300-Root Radius and Platinum Compliant Layer)*

Previous experience with upset and diffusion bonding single attachments indicated the need for upset and diffusion bond tooling to fabricate a fully-bladed ceramic-wrought alloy rotor. A schematic of the tooling designed for this purpose, as illustrated in Figure 51, shows the upper and lower load plates, the blade holder ring, and the outer retaining ring. These parts, when assembled, hold the 2 disk halves and 30 ceramic blades in their respective positions during the upset and diffusion bond cycle.

A two-dimensional analytical elastic stress analysis of the rotor and spin tooling was conducted during this task. Figure 52 summarizes the stress analysis results and illustrates the estimated rotor temperatures that were used based on previous hot spin test data. From this analysis, the P/A blade root stress of 10,500 psi was considerably below the 39,000 psi 3-Sigma lower bound ultimate stress level previously established. Although the elastic analysis did not consider the effect of stress concentrations, all other disk stress levels calculated were well below the stress rupture limit of AF2-1DA (93 ksi) at the temperatures anticipated.[*]

Additionally, the effective stress at location C (Figure 52) was also of interest due to the combined shear and normal stresses at this location. This effective stress was evaluated by first determining the principal stresses, then calculating the effective stress.

In this calculation the hoop stress was neglected due to its insignificant value. Thus,

$$\sigma_{P_1} = \frac{\sigma_R}{2} \pm \sqrt{\left(\frac{\sigma_R}{2}\right)^2 + \sigma_s^2} \tag{1}$$

where:

σ_{P_1} = principal stress
σ_R = radial stress
σ_s = shear stress

and therefore:

$$\sigma_{P_1} = \frac{29,700}{2} \pm \sqrt{\frac{(29,700)^2}{2} + (29,290)^2}$$

$$\sigma_{P_{1,2}} = 47.6, -18.0 \text{ ksi}$$

the effective stress is then:

$$\sigma_\epsilon = \sqrt{\sigma_{P_1}^2 + \sigma_{P_2}^2 - \sigma_{P_1}\sigma_{P_2}}$$

$$\sigma_\epsilon = \sqrt{47.6^2 + (1-18)^2 - (47.6)(-18)}$$

$$\sigma_\epsilon = 58.7 \text{ ksi}.$$

This effective stress and the anticipated temperature of 1400°F at location "5" in Figure 52 indicated a rotor life well in excess of the planned 50-hr test.

After completing tooling and component design, fabrication of all components was initiated.

---

[*] An experimental photoelastic stress analysis of the disk attachment area was conducted to determine the stress concentration effect and is discussed subsequently, in paragraph B.3.a.

53
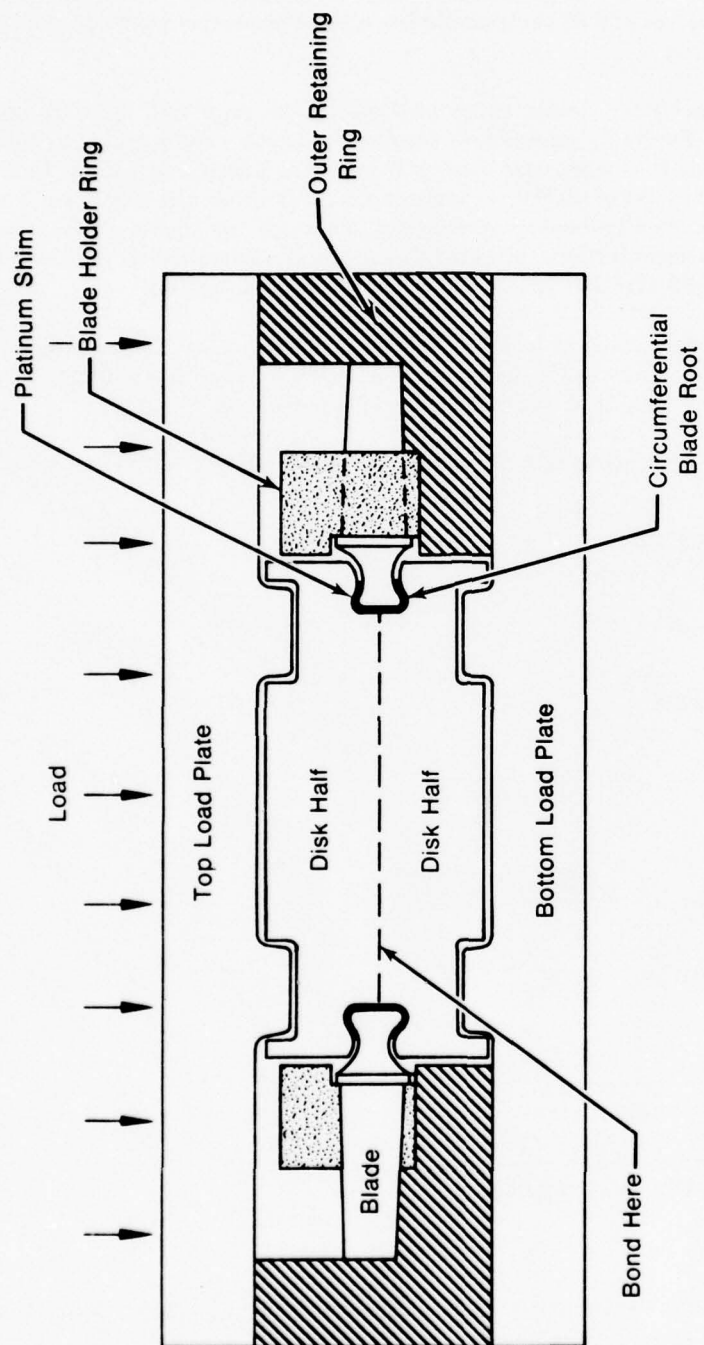
Figure 51. Upset Diffusion Bond Tooling

54

Calculated Stress

Location	Hoop Stress (ksi)	Radial Stress (ksi)	Maximum Shear Stress (ksi)
A	–	10.5	0
B	2.47	29.9	0
C	2.22	29.7	29.29
D	1.97	29.6	0
E	36.15	0	0
F	2.95	0	0
G	23.0	29.2	0
H	3.4	49.2	0

Note: These Stresses do not include stress concentration effects

Estimated Temperatures

Location	Temperature (°F)
1	2250
2	1650
3	1470
4	1470
5	1400
6	1300

2.42 in. r

1.43 in. r
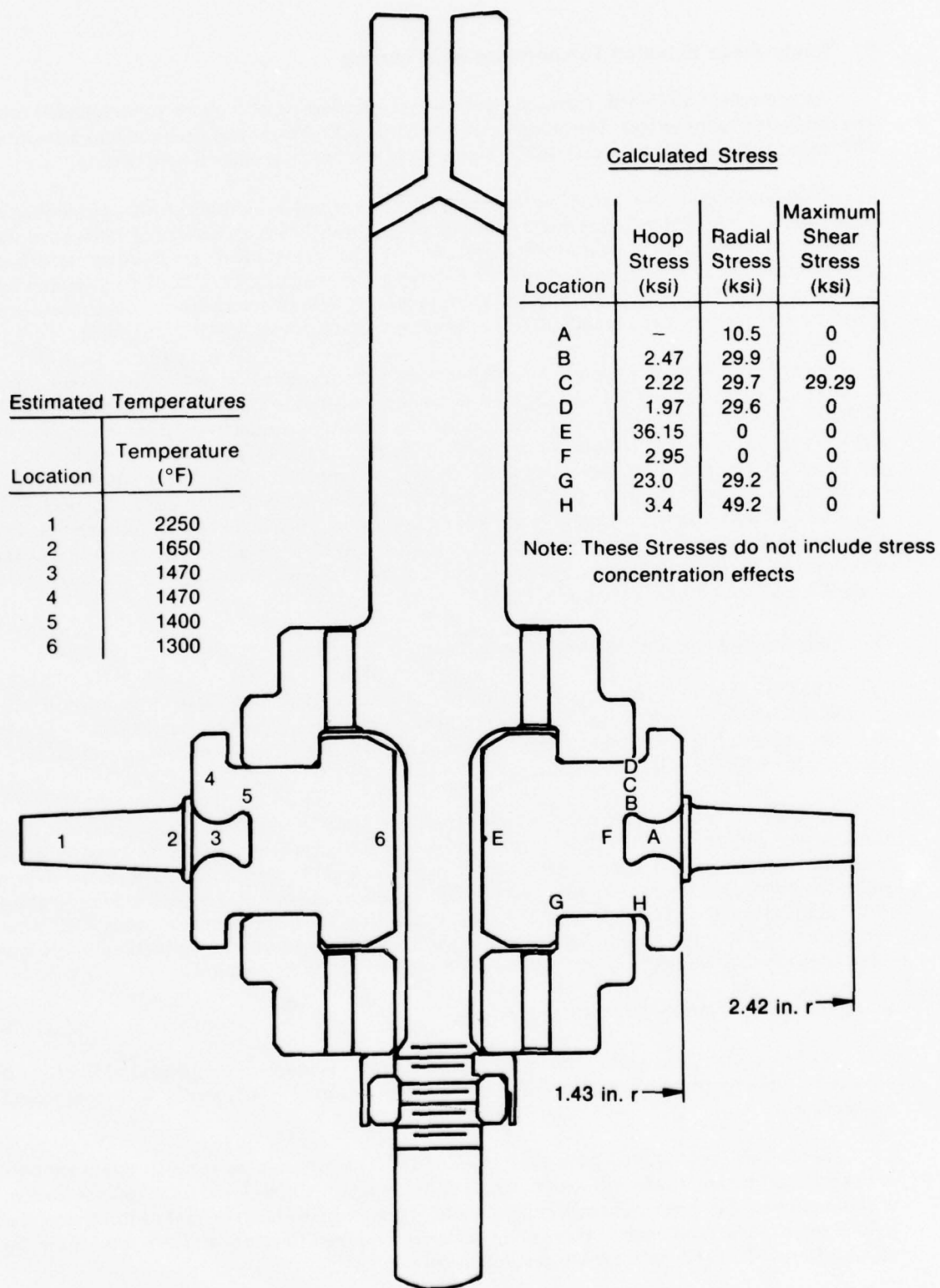
FD 101166B

Figure 52. Analytical Stress Analysis Summary for Hot Spin Rotor

55

2. Single-Blade Elevated-Temperature Spin Testing

As previously discussed, elevated-temperature spin testing of a single pseudobladed rotor was conducted to investigate the integrity of the hybrid attachment and the problems associated with spin testing at temperatures 150°F higher than the previous 2100°F spin testing.

Upon completion of fabrication the single blade rotor was assembled on the spin tooling as shown in Figure 53. Prior to conducting the actual spin test, however, a thermal calibration was initiated to determine localized temperatures in the attachment area. After attaching thermocouples at the locations illustrated in Figure 53, the assembly was installed in the spin test facility shown in Figure 54. Rotor and blade temperatures were then recorded at a low rotor speed after the temperatures had stabilized. Results of this analysis are shown in Figure 53.

Upon completion of the single-blade rotor thermal calibration, the test rotor was reinstalled in the spin facility (Figure 54) and the spin test was conducted to determine rotor and blade life under actual spin test conditions. Conditions for this test were the same as those anticipated for the Milestone II spin test: a blade temperature of 2250°F, a rotor speed of 45,000 rpm, and blade tip speed of 950 ft/sec. At these conditions testing was continued until 10 thermomechanical cycles and 66 hr at 45,000 rpm and 2250°F had been attained. Upon completion of this testing, the rotor and spin tooling assembly (Figure 55) was removed. Inspection of the rotor revealed no damage or deterioration. Thus, this spin test successfully demonstrated the capability of the ceramic attachment to complete the requirements of the Milestone II spin test. A summary of the complete test conditions is shown in Table 8.

3. Fully-Bladed Rotor Milestone II Spin Test

After completion of the single-blade hybrid rotor evaluation, a two-step effort was initiated to spin test a fully pseudobladed hybrid rotor in accordance with the program Milestone II spin test requirement. This effort consisted of: (1) experimental analysis of rotor design, and (2) fully-bladed rotor Milestone II spin testing.

An experimental analysis was conducted to substantiate the rotor design prior to conducting elevated-temperature spin testing. This analysis consisted of dynamic photoelastic strain analysis, experimental strain analysis, and fabrication and thermal calibration of the hybrid rotor. Data obtained during the photoelastic and experimental strain analyses were used along with temperatures obtained in the thermal calibration to predict hybrid rotor life. After completion of the rotor life prediction and fabrication, the program Milestone II spin test was conducted. Details supporting this testing are discussed in the following sections.

a. Experimental Analysis of Rotor Designs

To further verify the ability of the fully-bladed rotor to complete the program Milestone II objectives, an experimental analysis of the rotor was initiated concurrently with component fabrication.

The analysis and life prediction effort consisted of (1) a dynamic photoelastic strain analysis of the rotor attachment area, (2) experimental strain analysis of simulated rotor test specimens, (3) an analytical fracture mechanics analysis, and (4) an experimental thermal calibration of the hybrid rotor. Data from each of these analyses were combined to establish the hybrid rotor life using a Larson-Miller type rotor life prediction curve.

Thermocouple Location	Assumed Temperatures (°F)	Experimental Temperatures (°F)
1	2250	2250
2	1650	1500
3	1470	1400
4	1470	1140
5	1400	1170
6	1300	1050
7	—	1025
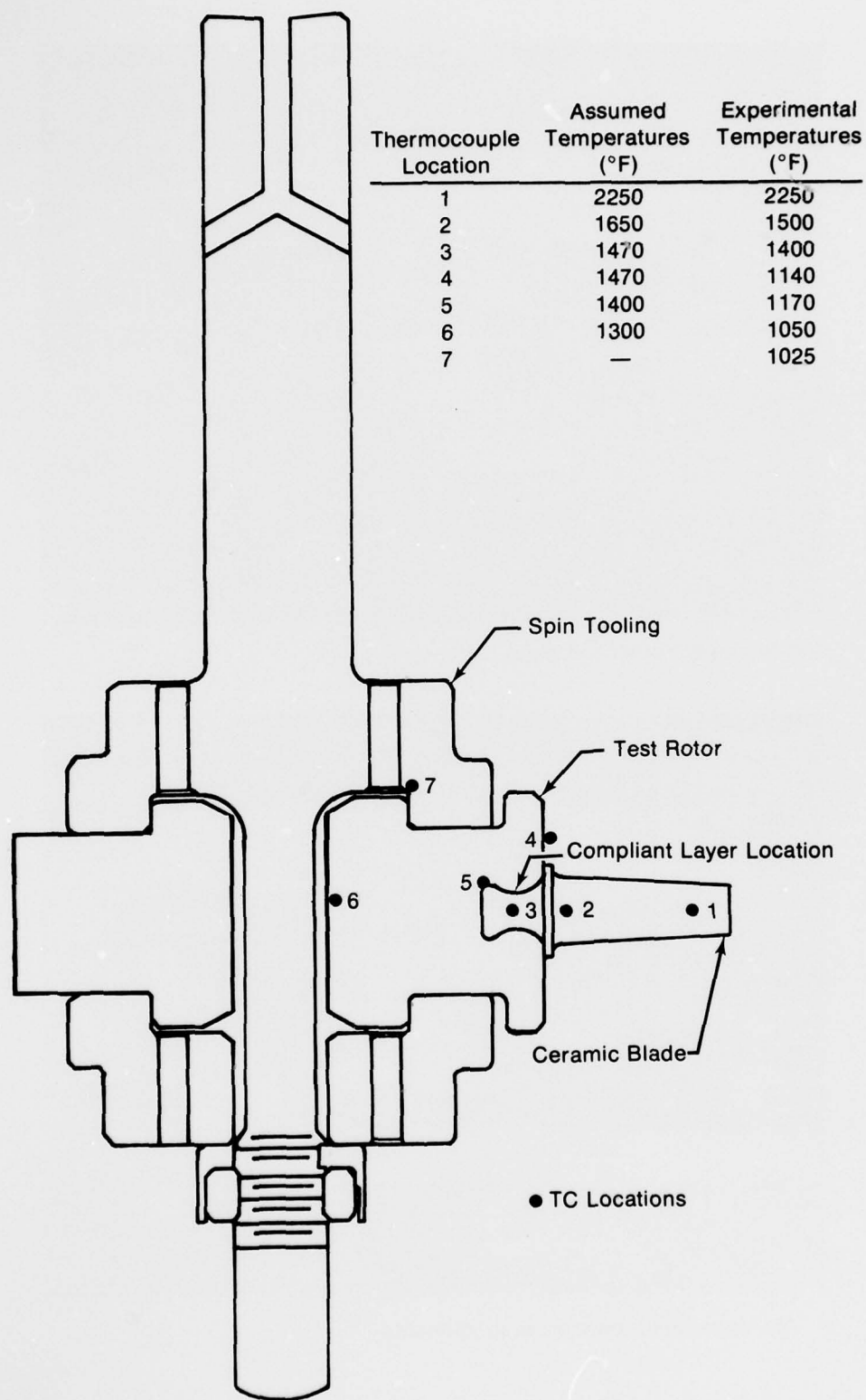
FD 101149B

Figure 53. Thermocouple Locations and Temperatures Measured on the Single-Blade Rotor and Tooling

57
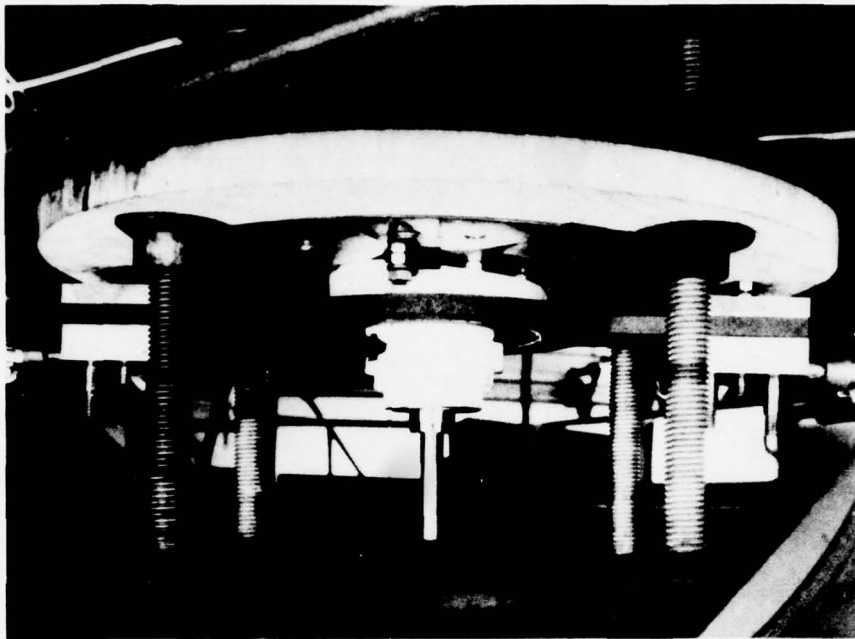
FC 33894

a) With Upper Furnace Heating Element
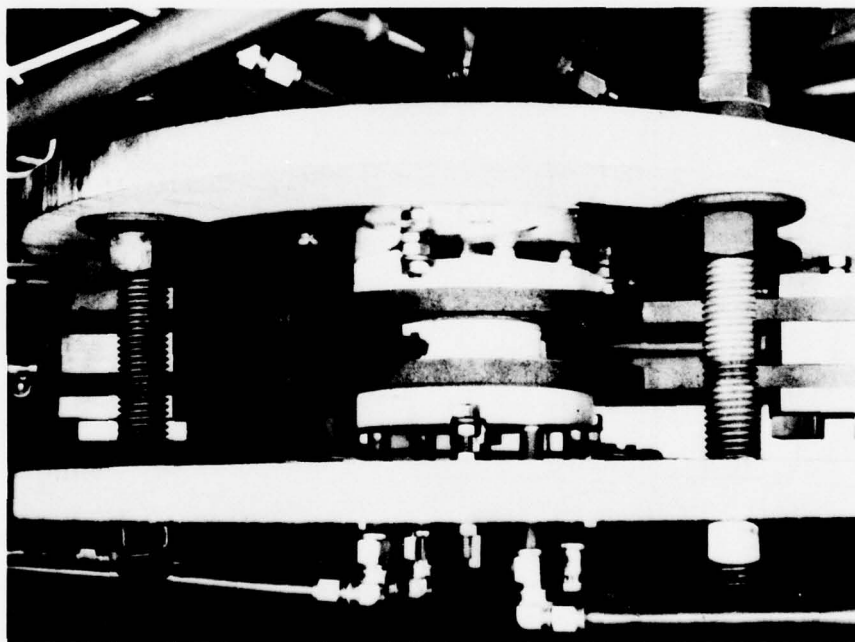
FC 33895

b) With Upper and Lower Heating Elements

FD 101142

Figure 54. Single-Blade Rotor Installed in the Spin Facility

58
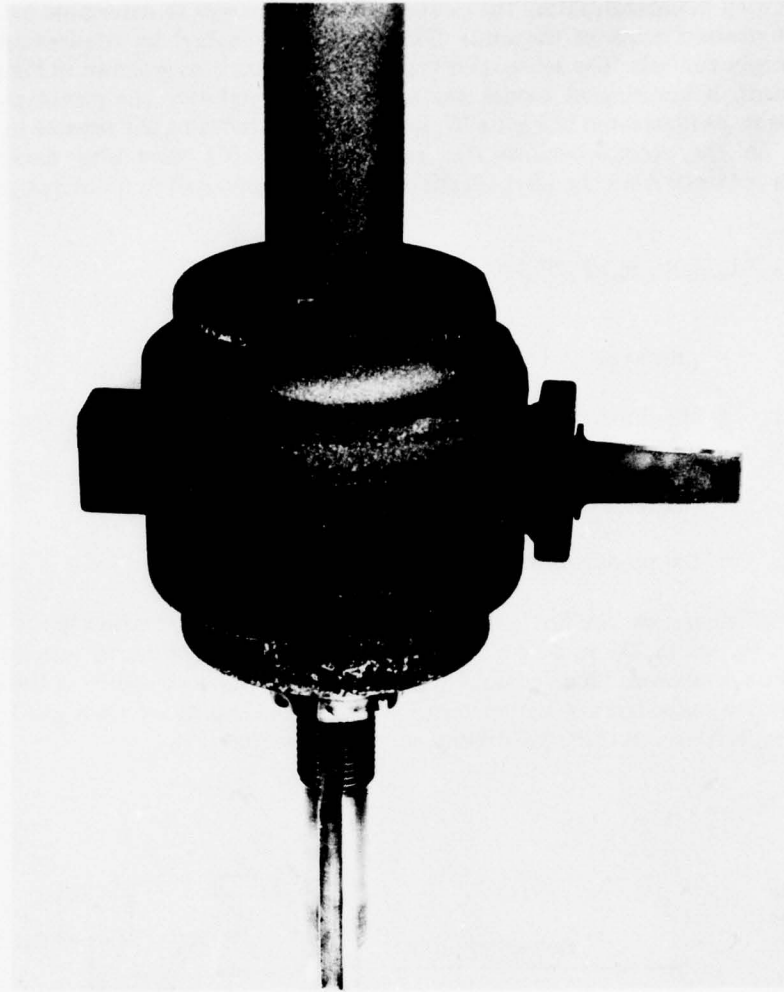
Figure 55. Single-Bladed Rotor and Tooling After 66 hr and 10 Cycles

TABLE 8. SINGLE-BLADED
ROTOR SPIN TEST
CONDITION

Rotor Speed, rpm	45,000
Tip Speed, ft/sec	950
Blade Temperature, °F	2,250
Blade Root P/A Stress, ksi	12
Rotor Diameter Tip-to-Tip, in.	4.84

59

The first step in substantiating the existing rotor design was to determine localized strain in the highly stressed areas of the rotor. This was accomplished by conducting a dynamic photoelastic strain analysis. The setup used to perform this analysis is shown in Figure 56. Using this arrangement, a birefringent model was spin tested simulating the prototype rotor cross section and loads, as illustrated in Figure 57. In addition to analyzing the stresses in the dovetail slot, stresses in the counterbalance rim radius (Figure 57) were also analyzed. Stress measurements obtained from the photoelastic model were converted to prototype stresses using the equation:

$$\sigma_p = \sigma_m(d_m/d_p)(t_m/t_p)(P_p/P_m) \qquad (2)$$

where:

σ_p, σ_m = prototype and model stresses, respectively

d_p, d_m = the linear dimensions of the area of concern of the prototype and model, respectively

t_p, t_m = the respective thickness

P_p, P_m = the prototype and model loads.

Based on this analysis, the predicted room temperature localized strain in the dovetail slot was 0.0046 in./in. at 45,000 rpm. At the counterbalance rim radius, a localized strain of 0.0019 in./in. was measured. Thus, combining this data with previous results of the single-blade thermal calibration indicated the critical strain and temperature in the rotor was 0.0046 in./in. and 1170°F, respectively, in the high-stressed area of the dovetail slot.
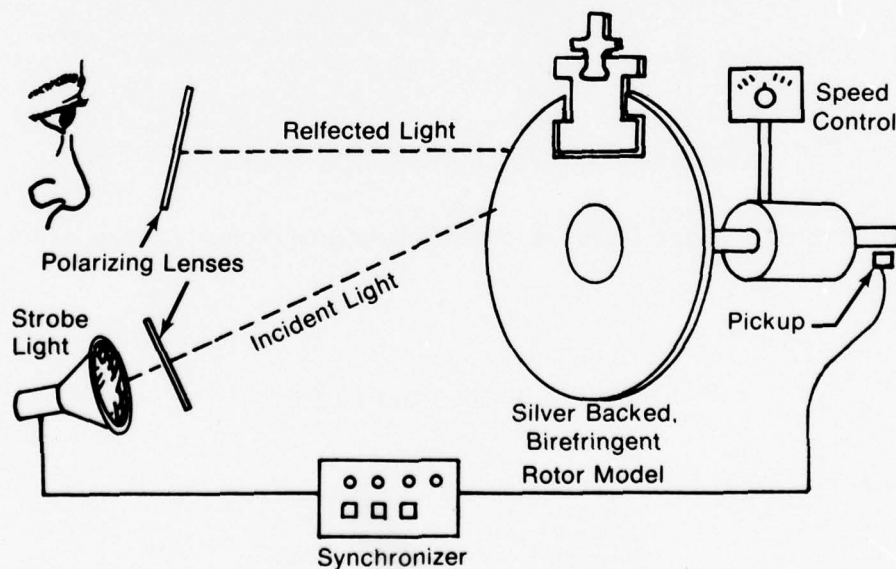
FD 93691A

Figure 56. Schematic of the Photoelastic Analysis of the Elevated-Temperature Rotor
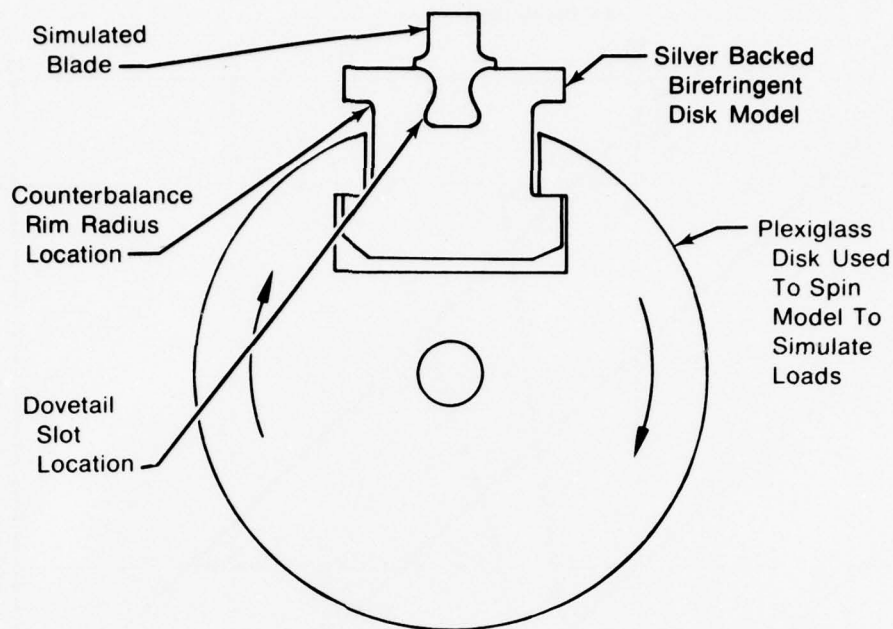
Figure 57. *Photoelastic Model Used for Experimental Strain Analysis*

To verify the rotor 50-hr life capability, strain-rupture testing of flat AF2-1DA test specimens was conducted. These specimens were machined to simulate a cross section of one-half of the rotor dovetail slot. One specimen was then strain gaged and calibrated to obtain room temperature load vs strain values. Specimens were subsequently strain-rupture tested at strains and temperatures representative of the prototype rotor dovetail conditions, i.e., 0.0046 in./in. (from previous photoelastic analysis) and 1170°F (from single-bladed rotor thermal calibration). Additional specimens were also tested at higher strain levels and temperatures (maximum of 0.0070 in./in. and 1550°F, respectively) to establish a Larson-Miller type strain-rupture curve. The results of this strain-rupture testing, as illustrated in Figure 58, indicated that with a local strain level of 0.0046 in./in., a dovetail slot temperature as high as 1470°F would still allow a 50-hr test.

The above strain-rupture testing did not include the effect of a problem that occurred on the initial elevated-temperature (2100°F) spin test of a disk with six hybrid attachments. The problem resulted as the spin facility speed controller cycled the test rotor between the upper and lower speed limits set on the controller. This cyclic speed variation resulted in a fatigue-induced reduction in the strain-rupture life of the IN 100 rotor. To investigate this effect on AF2-1DA material, two flat specimens were strain-rupture tested with a high R-ratio (0.98) small stress excitation superimposed on the steady-state load. These tests were conducted at 1200°F and 0.0046 in./in. strain and at 1300°F and 0.0070 in./in. strain, respectively. Both tests were terminated short of completion when it became evident that the high R-ratio small stress excitation had little or no effect on the rupture life of AF2-1DA at temperatures and strains expected in the fully-bladed rotor hot spin test.
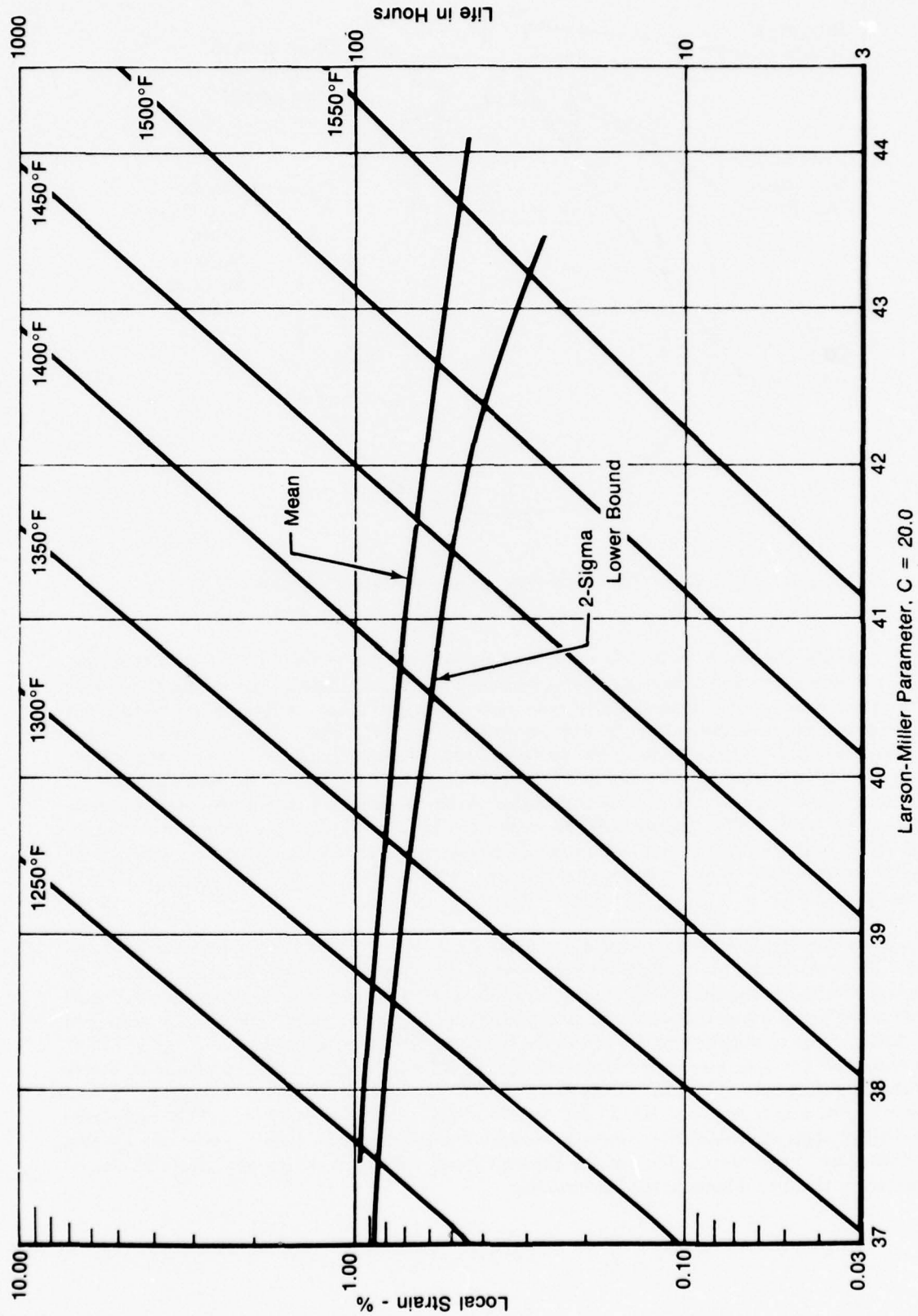
Figure 58. Results of Experimental Analysis of Flat Simulated-Geometry AF2-1DA Specimens

62

In addition to the experimental analysis, an analytical fracture mechanics analysis of the ceramic blade root was made to determine the maximum allowable flaw size for a successful test. For this analysis, the general equation

$$K = \sigma \sqrt{\pi a} \, F \qquad (3)$$

was used. This is the relation for the stress intensity of a surface flaw on a flat surface

where:

      a = flaw size, in.
      K = stress intensity factor, ksi $\sqrt{in}$.
      σ = maximum stress, ksi
      F = geometry factor.

      Solving for the flaw size,

$$a = \frac{1}{\pi} \left(\frac{K}{\sigma F} \right)^{2} \qquad (4)$$

A geometry factor of 1 was used for this analysis since the flaw size anticipated is considerably less than the part dimension.

The stress intensity factor used was based on the results of tests conducted at Pratt & Whitney Aircraft during the NASA-funded ceramic attachment program (Reference 3). Crack growth rate test results generated at 2200°F, as illustrated in Figure 59, were used for this analysis because they yield the most conservative flaw size. Based on this data, it was assumed that once the stress intensity threshold (K_{th} = 3.0 ksi $\sqrt{in}$.) was reached, crack propagation would be rapid and blade failure would be immediate.

The remaining variable in equation (3) is the maximum blade root stress. This stress was determined by reviewing photoelastic data obtained during the program's initial blade root design, and also by analyzing single blade ultimate spin test data.

Although no previous photoelastic analysis was conducted on the currently used continuous 0.300-in. root radius blade design, an analysis was conducted on a blade root design using a 30 deg load-bearing surface and a 0.300-in. fillet radius as shown in Figure 60. This analysis indicated that the maximum blade root stress in this dovetail design would be 45% above the P/A blade stress. The P/A stress in the pseudoblade design dovetail is 12 ksi at 45,000 rpm, thus, based on this analysis, the maximum blade root stress is 17.4 ksi.
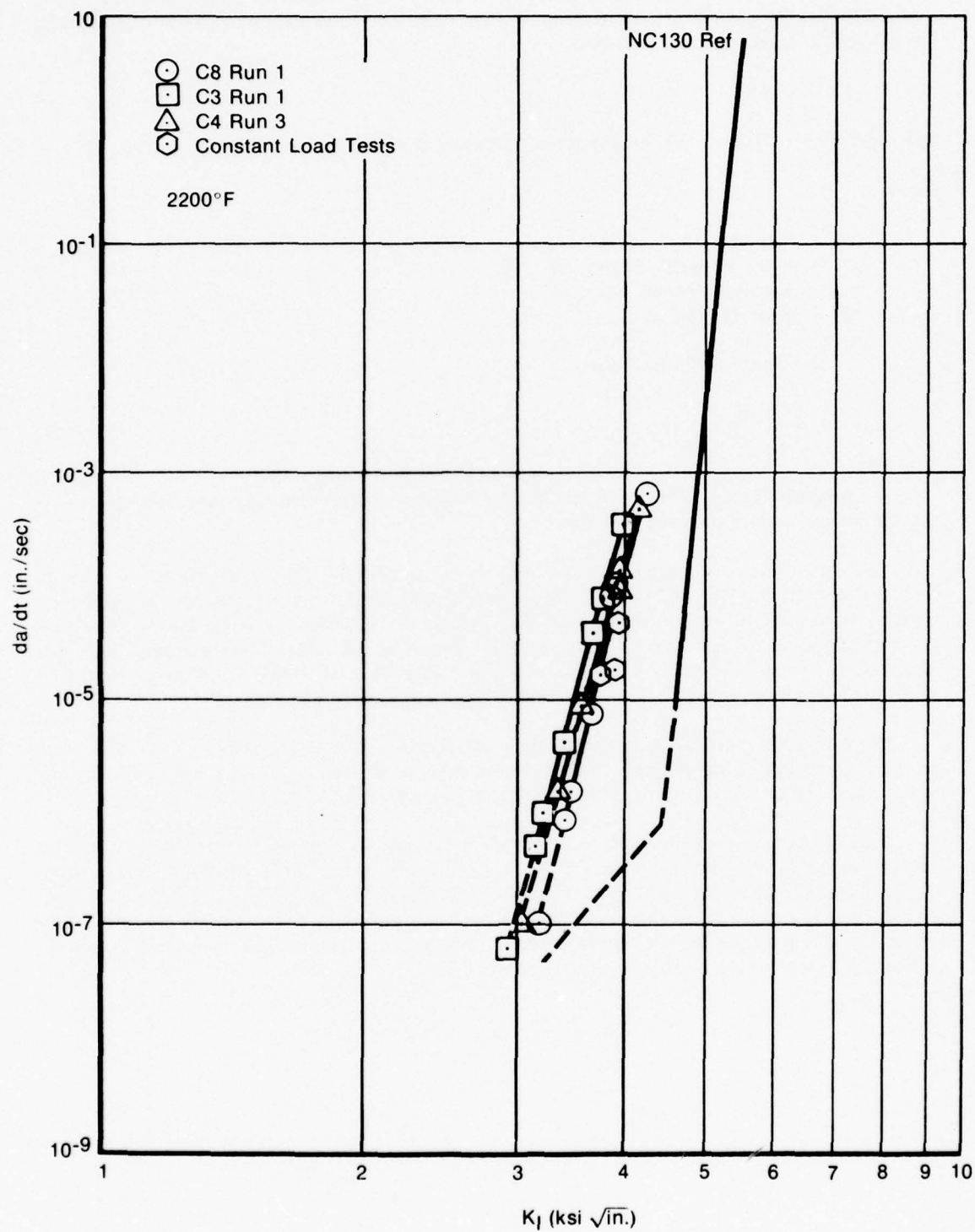
Figure 59. *The NC132 Crack Growth Rate vs K_I at 2200°F*

64

FD 86458B
781109
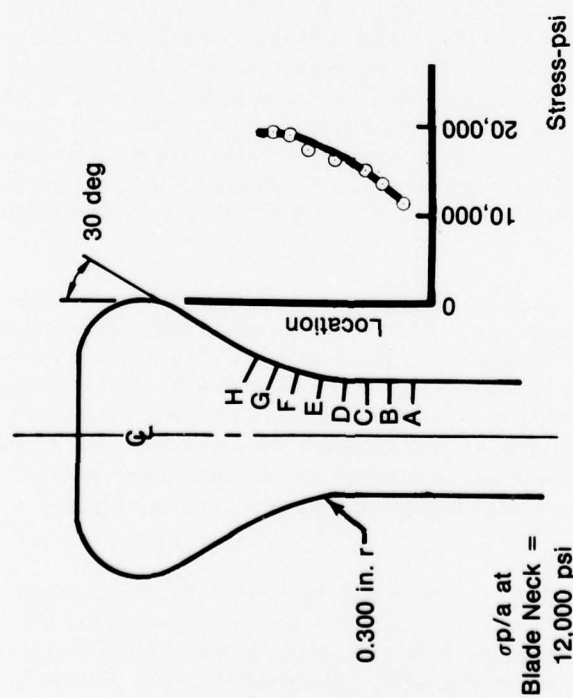
Figure 60. Photoelastic Analysis of Ceramic Blade Root Design

65

As a comparison, room-temperature ultimate spin test results were also analyzed to determine the possible maximum blade root stress. As previously reported, eight ceramic pseudoblade attachments were spin tested to their ultimate strength, resulting in a 2-Sigma P/A ultimate strength of 44 ksi. Based on an ultimate uniaxial tensile strength of 62 ksi for NC-132, and assuming that the tested blades failed at their ultimate tensile stress, the maximum stress in the dovetail was 40.9% higher than the average P/A blade root stress level. Applying this stress criteria, the maximum blade root stress at 45,000 rpm was 16.9 ksi. These two analyses correlated well, so the conservative maximum stress of 17.4 ksi was used for the flaw size determination. Thus, the maximum allowable surface flaw for a successful test was determined to be 0.009 in. as follows:

$$a = \frac{1}{\pi} \left(\frac{3 \text{ ksi } \sqrt{\text{in.}}}{(17.4 \text{ ksi}) (1)} \right)^2 \tag{5}$$

where:

$a = 0.009$ in.

This preliminary analysis indicated the small flaw size which would result in a failure in the blade root. Although it is questionable whether a flaw of this size could consistently be detected, inspection efforts were made to reduce this possibility. Previous nondestructive inspection (NDI) work conducted under the NASA program (Reference 3) using a seeded reference block indicated that X-ray inspection could detect high density inclusions as small as 0.002 in. and that C-scan sonic inspection could detect a defect as small as 0.016 in. in NC-132. Thus, prior to machining the ceramic blades, all billet material was sonic and X-ray inspected. Material containing any flaw indications was eliminated from further machining. Critical surfaces of the ceramic were also polished after final machining, and all blade surfaces were Zyglo inspected using ZL30 before the rotors were fabricated.

Upon fabricating the individual rotor components (i.e., rotor disk halves, ceramic pseudoblades, and individual platinum shims) and tooling, hybrid rotor fabrication was initiated. This consisted of (1) the upset-diffusion bond process to upset the superalloy rotor halves around the psuedoblade dovetails, thus, clamping each blade in its respective location, (2) post bond heat treatment to obtain the desired rotor mechanical properties, and (3) rotor finish machining to provide for attachment to the spin tooling. Prior to bonding the fully-bladed rotor, however, several upset/bond trials were conducted using four pseudoblades per trial to optimize techniques for the bond cycle. Following completion of the bond trials, a fully-bladed hybrid rotor was upset and diffusion bonded.

Although the fully-bladed rotor was designed to consist of 30 pseudoblades, this rotor was fabricated with two pseudoblades (one located 180 deg from the other) purposely omitted to allow for thermocouple placement in the dovetail slot. The previously obtained single-bladed rotor thermal calibration data could not be used to accurately predict the dovetail slot temperatures of the fully-bladed rotor. This was due to the anticipated disk rim area temperature increase resulting from the additional blades. The 28-pseudobladed rotor was then heat treated, finish machined, instrumented with thermocouples in the dovetail slot and on the ceramic blade, and assembled with the spin tooling. The completed hybrid rotor/tooling assembly is shown prior to thermal calibration in Figure 61.

A thermal calibration of the fully-bladed rotor was required to determine attachment area vs blade temperatures for the Milestone II spin test, and thus, verify or update the previously conducted experimental analysis conclusions. After completing fabrication and instrumentation, the rotor/spin tooling assembly, shown in Figure 61, was installed in the spin facility and the thermal calibration was conducted. The results of this calibration are shown in Figure 62 and

66

verify the anticipated higher disk rim temperature. Based on this information as well as the 2-Sigma lower bound curve in Figure 58, the 50-hr spin test at 45,000 rpm was possible. Specifically, a dovetail slot temperature of 1380°F would result in a disk life of approximately 400 hr with local strain of 0.0046 in./in.
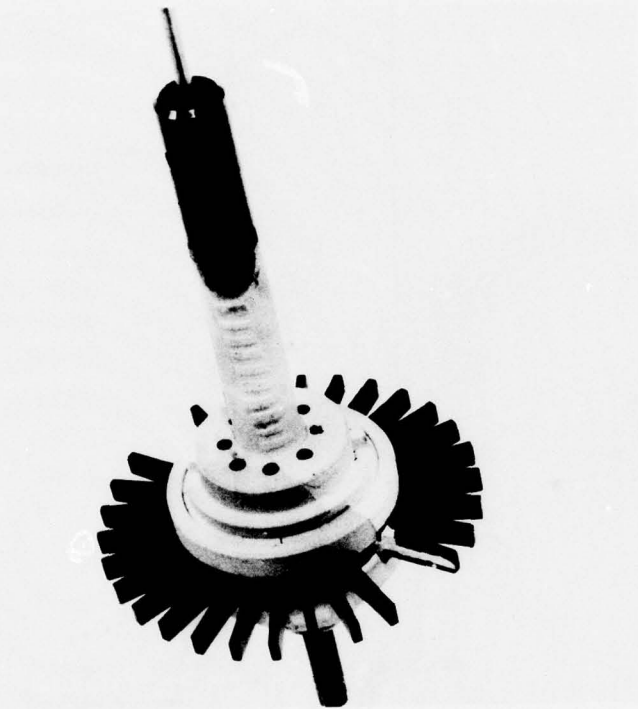
FAE 153481

Figure 61. The 28-Bladed Instrumented Rotor Prior to the 2250°F Thermal Calibration and Spin Test

Thermocouple Location	Temperatures (°F)
1	2250
2	1380
3	1280
4	1180
5	1070
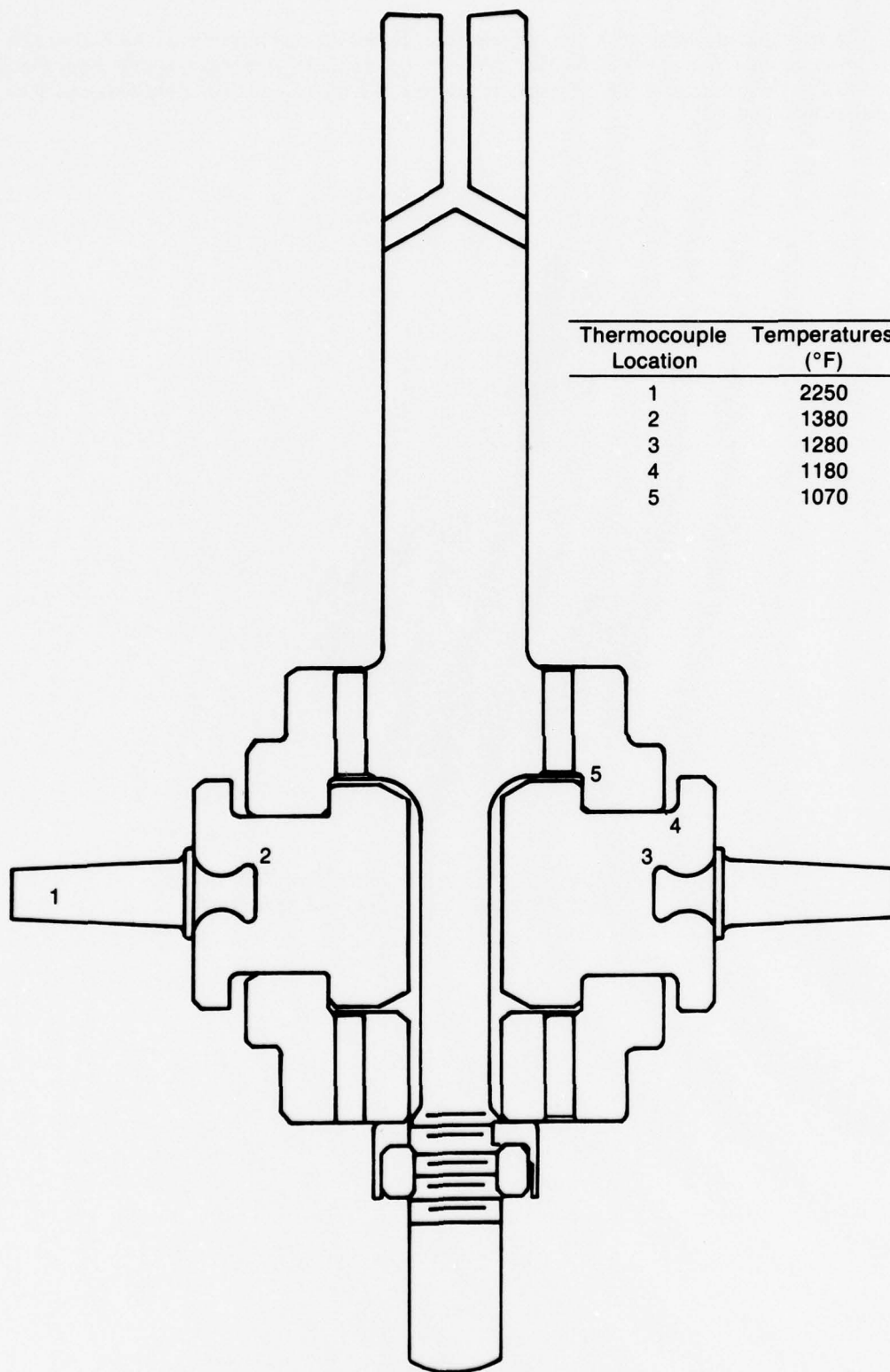
FD 101166B

Figure 62. Measured Temperatures for the 28-Bladed Rotor

68

b. Fully-Bladed Rotor Elevated-Temperature (Milestone II) Spin Test

The final task of Phase II consisted of spin testing a fully-pseudobladed rotor at 45,000 rpm for 50 hr with a blade temperature of 2250°F. Upon completion of the thermal calibration and, thus, verification of rotor life capability, the program Milestone II spin test was initiated and completed with two fully-bladed rotors containing 28 and 30 ceramic pseudoblades, respectively.

The 28-bladed rotor shown in Figure 61 was spin tested for a total of 54 hr and 10 thermomechanical cycles at 45,000 rpm with a blade temperature of 2250°F and a blade root P/A stress of 12 ksi. In addition to exceeding the milestone requirement by 4 hr at the same spin test conditions described above, this testing successfully demonstrated, for the first time, the capability of the hybrid rotor.

Additionally, to further verify rotor fabrication techniques and rotor integrity, a hybrid rotor containing 30 ceramic pseudoblades was fabricated for spin testing. Specifically, the hybrid rotor shown in Figures 63 and Figure 1 was spin tested for 50 hr and 10 thermomechanical cycles at 45,000 rpm with a blade temperature of 2250°F and a P/A attachment stress of 12 ksi. This successful rotor test further demonstrated the ceramic-wrought alloy attachment integrity as it was the second rotor to complete the program Milestone II spin test requirements.

FAE 155798

Figure 63. The 30-Bladed Hybrid Rotor and Spin Tooling Prior to Spin Test

SECTION IV

PHASE III — AIRFOILED HYBRID ROTOR ELEVATED-TEMPERATURE SPIN TEST

After completing the initial program goals, a 12-month program extension was negotiated to extend hybrid rotor technology by fabricating and spin testing a fully-bladed "airfoiled" rotor at elevated temperature. To accomplish this additional effort, a two-task program was established that consisted of:

    1. Additional Experimental Analysis of the Phase II Rotor
    2. Elevated-Temperature Spin Testing of an Airfoiled Hybrid Rotor.

To summarize, the existing pseudoblade rotor and spin tooling designs were to be used for hybrid airfoiled rotor fabrication and spin testing to minimize fabrication costs and to eliminate a disk redesign effort. Since a rotor speed of 60,000 rpm is typical for small gas turbine engines, an experimental analysis was conducted to determine whether 60,000 rpm speed capability was attainable using this rotor and tooling design. Although this analysis indicated that 60,000 rpm elevated-temperature rotor capability was feasible, the maximum speed capability of the spin tooling was limited to 53,000 rpm.

Following the completion of experimental analysis of the existing rotor, program efforts were directed toward completion of the program extension milestone; i.e., elevated-temperature spin testing of an airfoiled hybrid rotor. This effort was accomplished by (1) designing and fabricating hybrid rotor components, (2) conducting analytical and experimental analyses of these components, and (3) fabricating and spin testing a hybrid airfoil-bladed rotor at elevated temperature. Upon initiation of this test, an abrupt test abort, destroying approximately 70% of the airfoils, occurred after 5 hr of spinning at speeds ranging from 30,000 to 45,000 rpm and a blade temperature of 2250°F. A subsequent failure analysis determined that the test abort was caused by a spin tooling failure and not by airfoil component failure.

A. ADDITIONAL EXPERIMENTAL ANALYSIS OF PHASE II ROTOR

A two-part experimental strain analysis of the Phase II rotor and spin tooling designs was initiated to determine the elevated-temperature speed capability and life of these components at speeds in excess of 45,000 rpm. The analysis consisted of (1) experimental strain analyses (2) additional spin testing of the 30-pseudoblade rotor at elevated temperatures to verify or update the experimental analysis results. The results of the experimental strain analyses were superimposed to obtain the total rotor and tooling strain. This strain was then related to rotor and tooling life by using the Larson-Miller curves developed from previous testing of AF2-1DA and IN-100 materials, respectively, as discussed in the following sections.

1. Experimental Strain Analysis of Phase II Rotor

For the first part of the analysis, strain gages were attached to the rotor to measure hoop and/or axial strain at the locations identified in Figure 64. Strain gages were not attached to the spin tooling "Bottom Plate" (Figure 64) because of difficulty in routing the strain gage lead wires during rotor/tooling assembly. The rotor was installed in the spin facility, and strain vs rpm data up to 40,000 rpm were obtained. Strain results are shown in Figure 64 with extrapolated strain levels for 60,000 rpm. These strain levels are lower than levels anticipated, based on previous photoelastic anaysis of the rotor disk. One reason for this difference was the hoop restraint of the solid disk; a condition not evaluated during the two-dimensional photoelastic analysis.

Location	Temperature °F	Measured Strain at 40,000 rpm μ in./in.		Extrapolated Strain at 60,000 rpm μ in./in.	
		Hoop	Axial or Radial	Hoop	Axial or Radial
1	2250**	Not Measured	Not Measured	—	—
2	1590*	Not Measured	Not Measured	—	—
3	1500*	Not Measured	Not Measured	—	—
4	1380**	420	680	945	1530
5	1300	380	No Readng	855	—
6	1280*	390	No Reading	880	—
7	1250*	360	480	810	1080
8	1150	500	420	1125	945
9	1110	380	360	855	810
10	1110	700	No Reading	1575	—

** Fully Bladed Rotor (Phase II) Thermal Calibration
* Extrapolated From Single Blade Thermal Calibration
   Remaining Temperatures Extrapolated From Analytical
   and Experimental Analysis
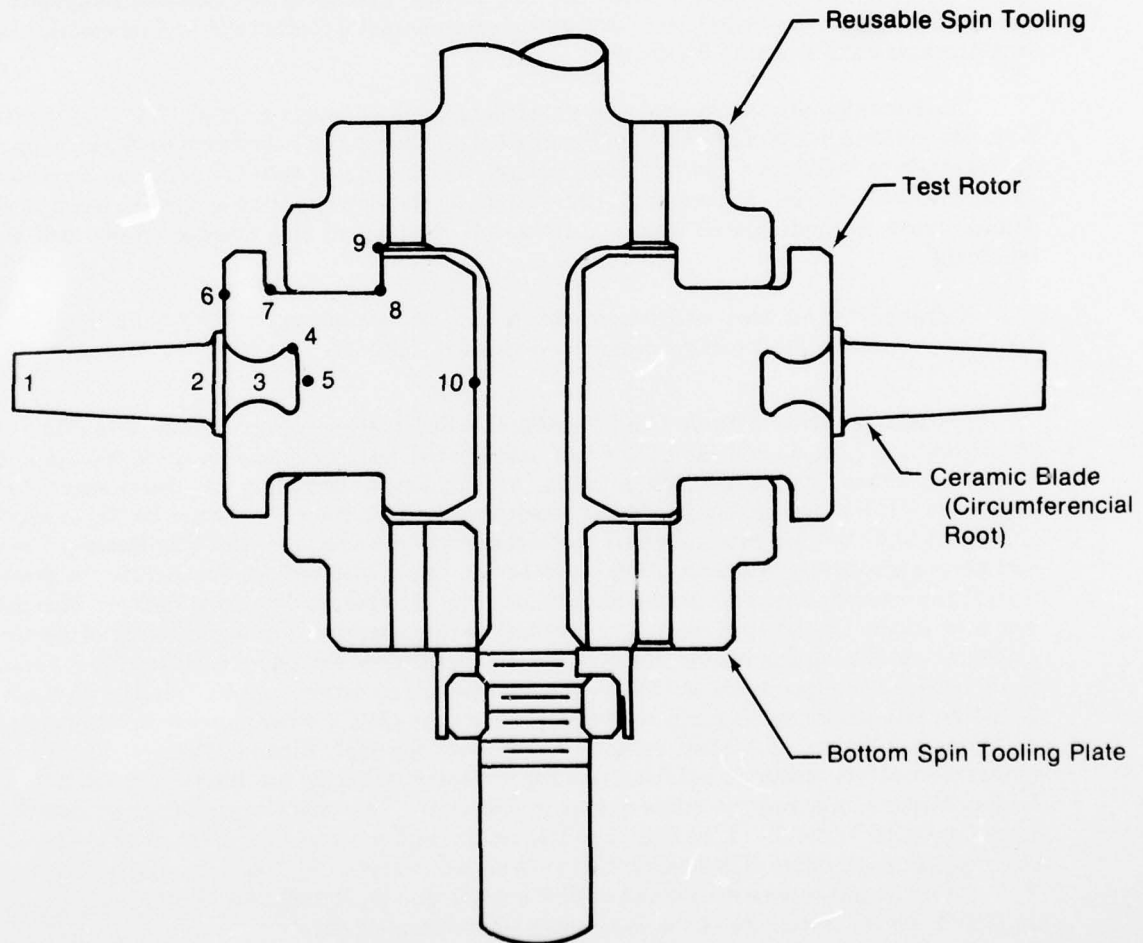
FD 101147B

Figure 44. Results of Dynamic Strain Analysis

71

Temperatures at the strain gage locations are shown in Figure 64. These temperatures are a compilation of all temperature surveys, analytical evaluations, and thermal calibrations conducted during this program and were used to evaluate the severity of the strain at each location. Test results indicated that the most severe strain and temperature conditions were in the dovetail root radius, location 4, and in the disk face flange radius, location 7. However, none of the mechanical strain levels measured or extrapolated to 60,000 rpm, would result in rotor failure at the temperatures noted based on strain rupture data previously established (Figure 65). At 60,000 rpm, hoop strain, radial strain and temperature at locations 4 and 7 are 420 μ in./in., 680 μ in./in., 1430°F and 360 μ in./in., 480 μ in./in., and 1300°F, respectively.

To determine total rotor strain, thermal strain was superimposed on the mechanical strain for evaluation. The temperatures shown in Figure 64 were used as a basis for thermal gradient generated strain. To evaluate this thermal strain, an unbladed rotor disk was instrumented with thermocouples and strain gages and subjected to conditions that would reproduce the disk thermal gradients. Thermocouple instrumentation was located in the dovetail root radius, disk face flange radius, disk rim, and bore, locations 4, 7, 6 and 10 in Figure 64, respectively. Radial and circumferential strain gages were located in the dovetail root and disk face flange radii, locations 4 and 7. Additionally, dial indicators were located at the disk rim to measure axial and radial deflection to determine whether the disk thermal gradients (not absolute temperatures) produced sufficient rim deflection to disturb the ceramic-metal contact areas. A schematic of this instrumentation is shown in Figure 66.

The condition of most interest was a thermal gradient of approximately 170°F between the disk rim and bore, locations 6 and 10 in Figure 64. This "worst case" condition produced hoop and radial strain in locations 4 and 7 of approximately −600 μ in./in. and 1000 μ in./in., and −200 μ in./in. and 340 μ in./in., respectively. These strain levels were not large enough to result in disk failure under any anticipated test conditions, but mechanical and thermal strains had to be combined.

A summary of all stress and temperature data for 60,000 rpm and 2250°F blade temperature for the two most severe locations (4 and 7) is listed in Table 9.

The results shown in Table 9 and the AF2-1DA disk material strain rupture data (Figure 65) show that rotor life should far exceed any anticipated test requirements at 60,000 rpm. The maximum strain condition (2530 μ in./in. at location 4, assuming the hoop strain to be insignificant) is shown in Figure 65 and illustrates that the rotor should not be strain-rupture limited at 1420°F. This data indicated that a temperature as high as 1450°F at location 4 would still permit a spin test in excess of 900 hr. However, this conclusion did not include the possible high R-ratio small-stress excitation effect induced by the spin facility drive turbine. This effect was seen in the IN-100 spin rotor during initial elevated-temperature spin testing of six single attachments. During this testing, the high R-ratio small-stress excitation significantly reduced in the IN-100 strain rupture life at 1500°F. Previous testing to determine the high R-ratio effect on AF2-1DA was conducted at temperatures lower than the 1380°F attachment temperature shown in Figure 64. As an additional safeguard, however, the high R-ratio effect on IN-100 (50% reduction in strain rupture life of flat strain rupture test specimens) was imposed on the AF2-1DA Larson-Miller strain rupture curve shown in Figure 65. This was accomplished by arbitrarily reducing, by 50%, the life of the specimen test results that produced the original AF2-1DA curve and replotting the curve. The resultant curve is shown in Figure 65. Using the more conservative 97.5% lower bound curve with a strain of 2500 μ in./in. and an attachment temperature of as high as 1450°F, the expected life of the rotor was still in excess of 500 hr.

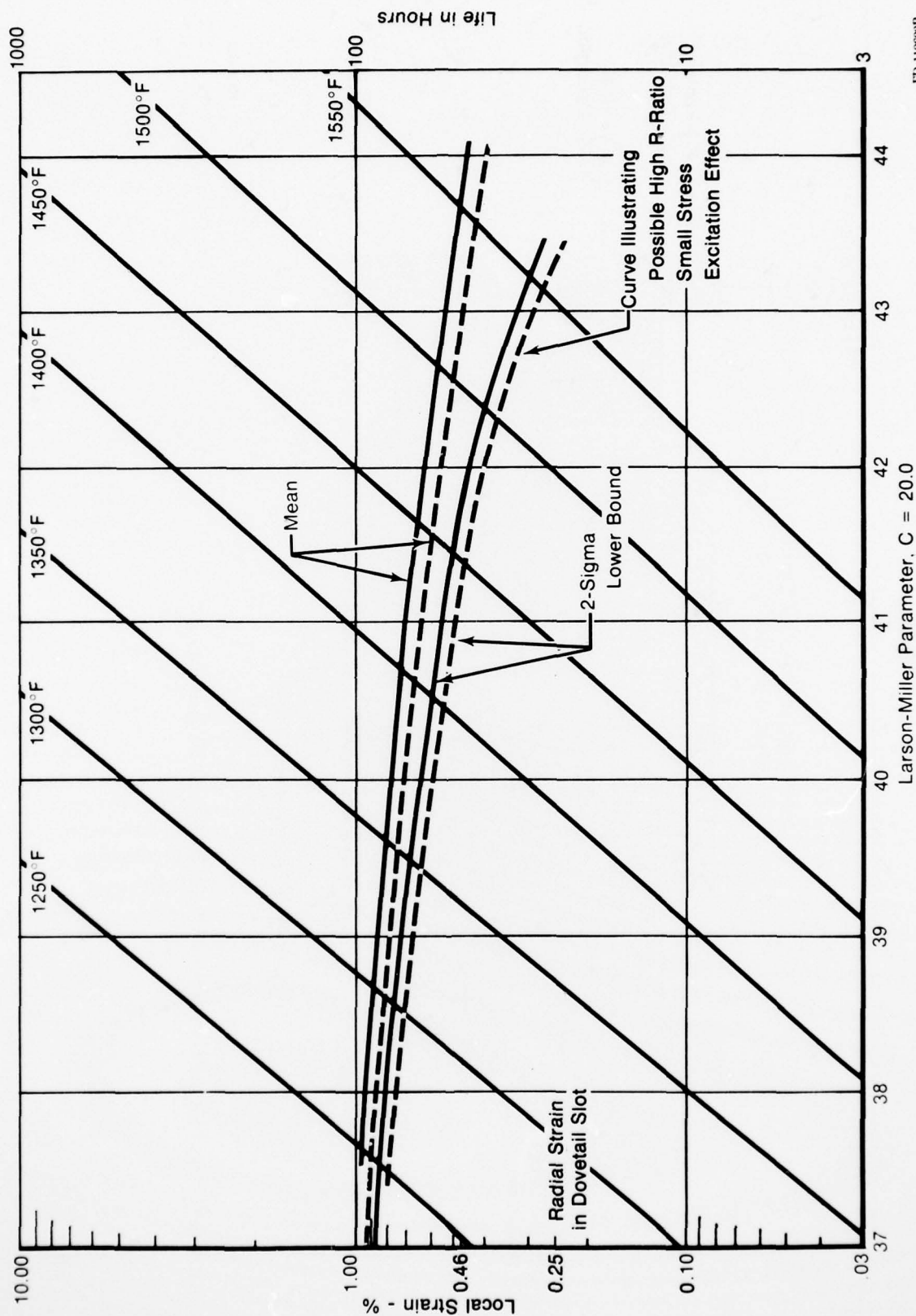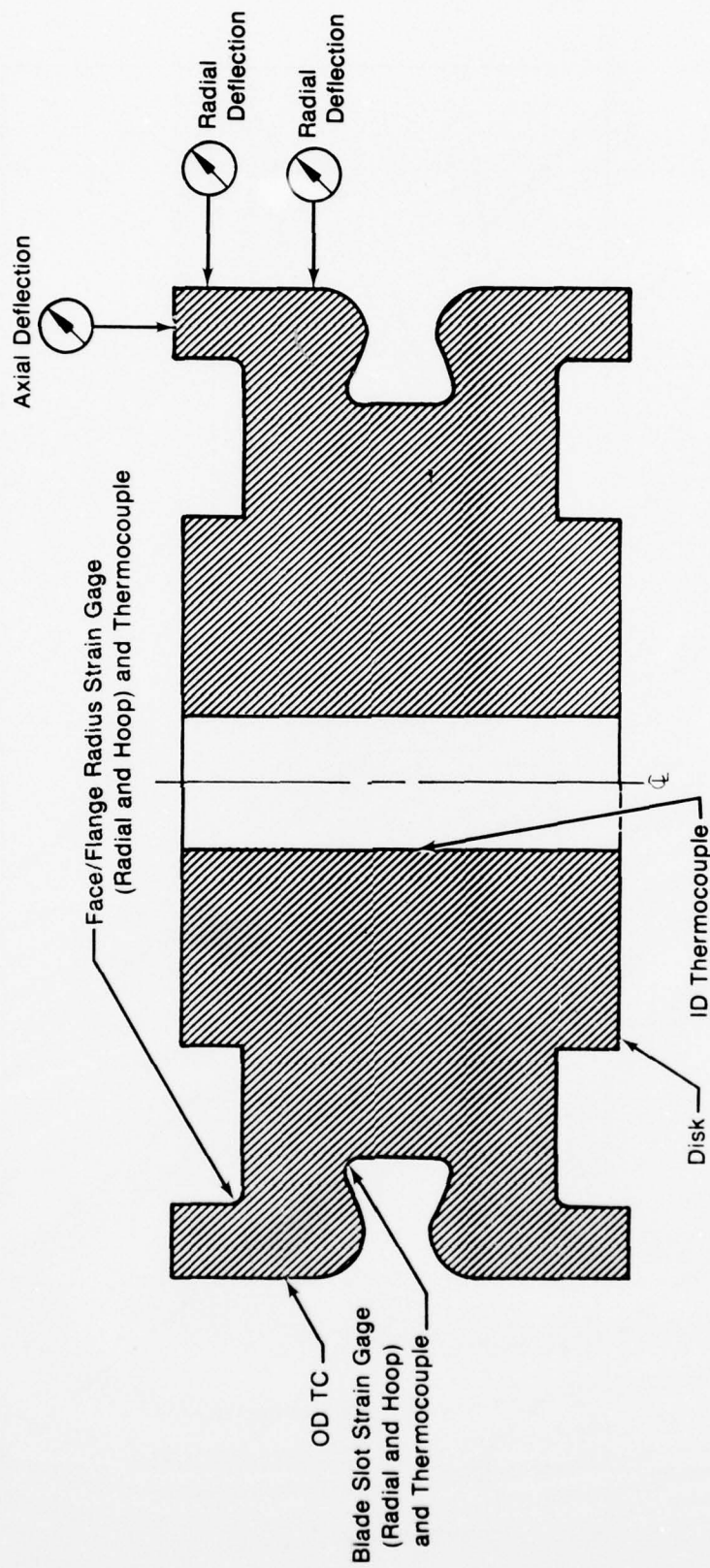Figure 65. Localized Strain Rupture Characteristics of AF2-1DA Disk Material

Figure 66. Hybrid Rotor Disk, Thermal Test Instrumentation Locations

FD 124368

TABLE 9. STRESS AND TEMPERATURE DATA

Location	Mechanical Strain (μ in./in.)		Thermal Strain (μ in./in.)		Total Strain (μ in./in.)		Temperature (°F)
	Hoop	Radial	Hoop	Radial	Hoop	Radial	
4	945	1530	−600	1000	345	2530	1430
7	810	1080	−200	340	610	1420	1250

2. Additional Phase II Rotor Spin Testing

The experimental analysis indicated that the rotor and spin tooling life would exceed the 50 hr extension milestone life requirement. However, one part of the spin tooling (bottom plate shown in Figure 64) could not be experimentally analyzed due to difficulty in routing strain gage wires during rotor/spin tooling assembly. As a result of this, and as a final verification of the 60,000 rpm rotor and tooling elevated temperature capability, additional spin testing of the Phase II 30-pseudobladed rotor was conducted.

With a ceramic pseudoblade temperature of 2250°F, the fully-bladed rotor (previously tested for 50 hr and 10 thermomechanical cycles during Milestone II spin testing of 45,000 rpm with a blade temperature of 2250°F) was spin tested for an additional 38 hr and 4 thermomechanical cycles (a cumulative total of 88 hr and 14 cycles). Prior to precluding this testing, a test was conducted to determine whether 60,000 rpm was attainable.

The rotor speed was slowly increased from 45,000 rpm toward the goal of 60,000 rpm but at 53,000 rpm an abrupt test abort occurred, destroying all of the ceramic pseudoblades. A subsequent failure analysis was initiated. Initial observations indicated that the cause of failure was an erroneously located platinum compliant layer that resulted in ceramic/metal contact on *the dovetail load carrying surface, thus causing pseudoblade failure.* The failed pseudoblade then impacted against the remaining blades causing them to fail. In addition, an inspection of the spin tooling revealed that the bottom plate (Figure 64), which could not be experimentally analyzed, had yielded to an oval shape (approximately 0.002 in. out-of-round). As a result of yielding the tooling, it was concluded that future elevated-temperature airfoiled hybrid rotor testing would be limited to rotor speeds less than 53,000 rpm.

B. ELEVATED-TEMPERATURE SPIN TESTING OF AIRFOILED HYBRID ROTOR

Upon completion of the pseudobladed rotor spin testing and experimental analysis, program efforts were directed toward fabrication and elevated-temperature spin testing of an airfoiled hybrid rotor. This effort was conducted in three-subtasks consisting of:

1. Airfoiled Rotor Component Design and Fabrication
2. Airfoil Analytical and Experimental Analyses
3. Airfoiled Hybrid Rotor Elevated-Temperature Spin Test.

To summarize, hybrid rotor component design and fabrication was conducted. As previously mentioned, the superalloy disk used in the pseudobladed rotor design of Phase II was chosen for the hybrid rotor, thus minimizing fabrication costs and eliminating a disk redesign effort. The airfoil concept selected for use with the circumferential hybrid attachment approach was the "platformless blade" concept. This concept, chosen for its machinability and low cost, consisted of a blade without a platform. The platform (endwall) sections were fabricated separately and were placed between the blades to protect the rotor by forming the inner gas flowpath. Typical small gas turbine airfoil and endwall components were designed and fabricated to demonstrate this concept.

75

Subsequently, analytical and experimental analyses of these components were conducted to evaluate this blade concept. The analytical study consisted of a NASTRAN plate element analysis and maximum allowable flaw size determination for the airfoil and endwall components. Experimental analysis consisted of spin testing components to failure, conducting subsequent failure analysis, and proof testing blade components prior to installation in the hybrid rotor.

After completion of airfoil analysis and component fabrication, the airfoiled hybrid rotor was fabricated and instrumented with thermocouples. A thermal calibration was then conducted. Calibration results were combined with the experimental rotor analysis results of Task I and the analytical and experimental airfoil analyses results of Task II to determine a maximum speed capability of the hybrid rotor/spin tooling assembly of 53,000 rpm. Upon establishing the maximum speed capability, a program extension milestone test plan was designed to more closely simulate the conditions of an actual small gas turbine engine cycle. This test plan called for spin testing the rotor at various speeds between 30,000 and 50,000 rpm with a constant blade temperature of 2250°F. The test was initiated but an abrupt spin test abort, destroying approximately 70% of the airfoil components, occurred at 45,000 rpm after 5 hr of spin testing at speeds ranging from 30,000 to 45,000 rpm and a blade temperature of 2250°F. A subsequent failure analysis indicated that the test abort was caused by a spin arbor failure and not by a ceramic blade failure.

These efforts are discussed in detail in the following sections of this report.

## 1. Airfoiled Rotor Component Design and Fabrication

Since the Phase II disk and spin tooling designs were to be used for the airfoiled hybrid rotor, program efforts were directed toward airfoil concept selection and design. The "platformless blade" airfoil concept was selected (over the platformed blade concept) because of its machinability and potential low cost. This concept consisted of a blade without a platform (Figure 67) and a root radial cross-section that followed the blade airfoil camber. The platform (endwall) selections were fabricated separately and were placed between the blades to protect the rotor by forming the inner gas flowpath (Figure 68).

With the selection of the platformless blade concept, a typical small gas turbine airfoil and accompanying endwall section were designed. For simplicity of fabrication, the airfoil design was straight-line faired from root to tip using the airfoil sections shown in Figure 69. The dovetail root radial cross-section was the same as the blade root section of Figure 69, and the circumferential root cross-section was the same as that of the Phase II pseudoblades. The endwall section was designed to mate with the respective concave and convex surfaces of the airfoil root.

After completion of airfoil and endwall design, fabrication of the tooling needed to machine the actual airfoil and endwall components was initiated.* Airfoil and endwall fabrication was then initiated. Although fabricated separately, the airfoil blade and the endwall (platform) sections were each fabricated using three operations: (1) dovetail root machining, (2) concave contour machining, and (3) convex contour machining. Dovetail root contour machining for both parts was accomplished on a visual grinding machine using a rotary table to obtain the circumferential root contour. As shown in Figures 70 and 71, the dovetail contour was machined to a 10X chart while rotating the part under the diamond grit grinding wheel.
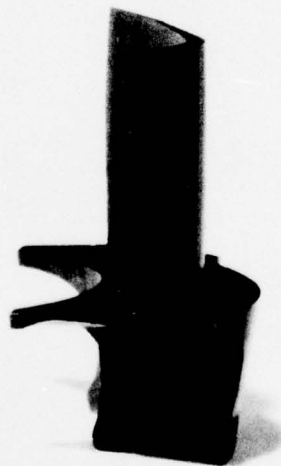
---

*This tooling is shown in a subsequent description of the fabrication process (Figures 73 through 79).
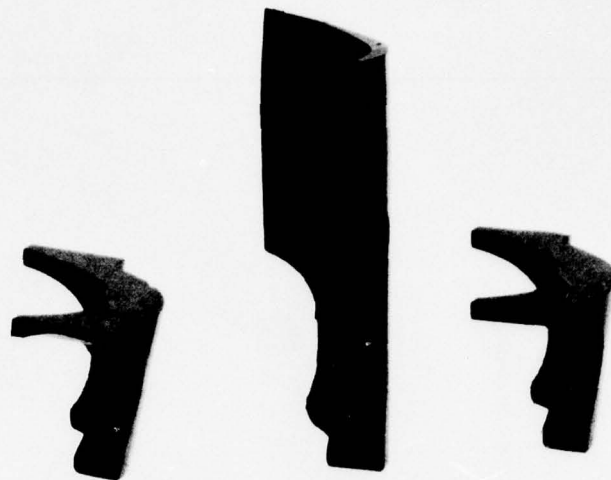
FE 158624

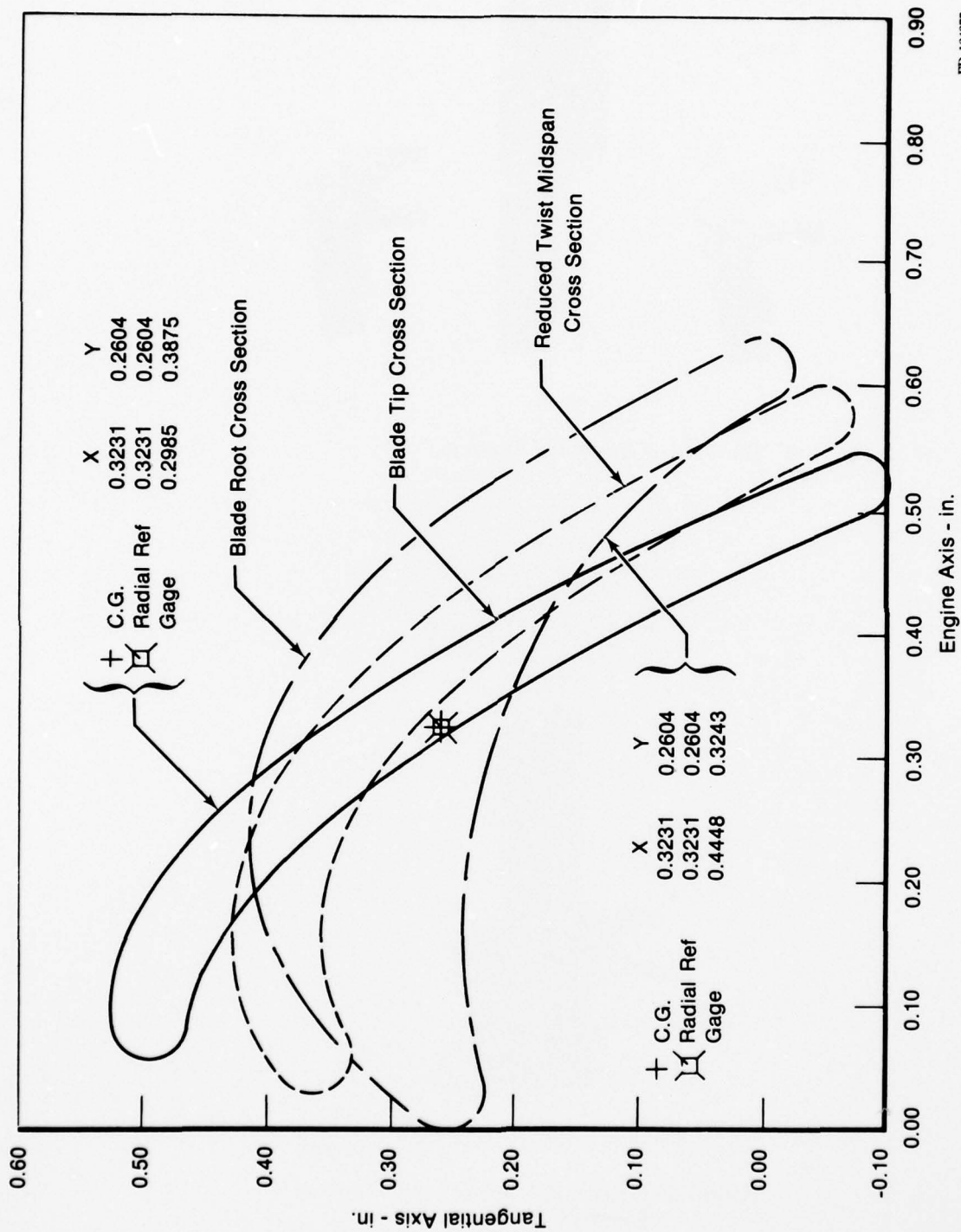*Figure 67. Platformless Blade and Endwalls*

FE 158623

Figure 68. Platformless Blade and Endwall Assembly

Figure 69. Ceramic Blade Root Cross-Section

FD 124377

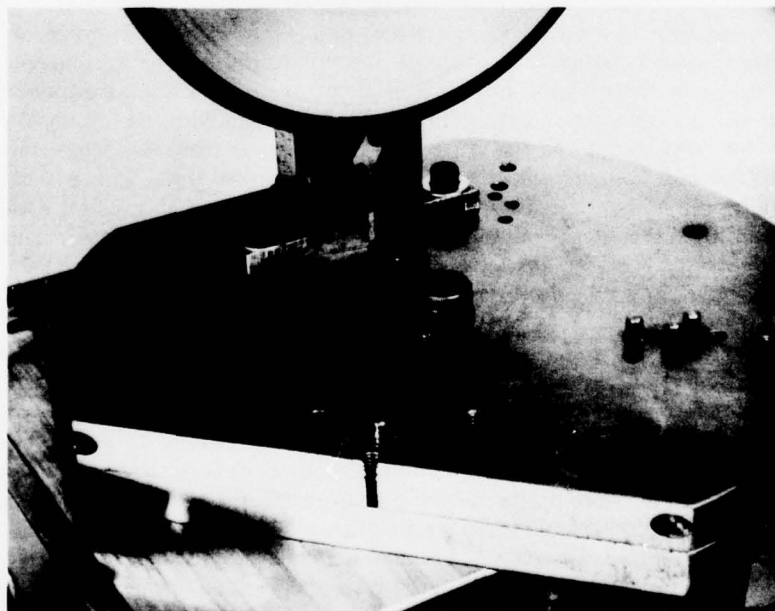Optical
Grinding
Machine
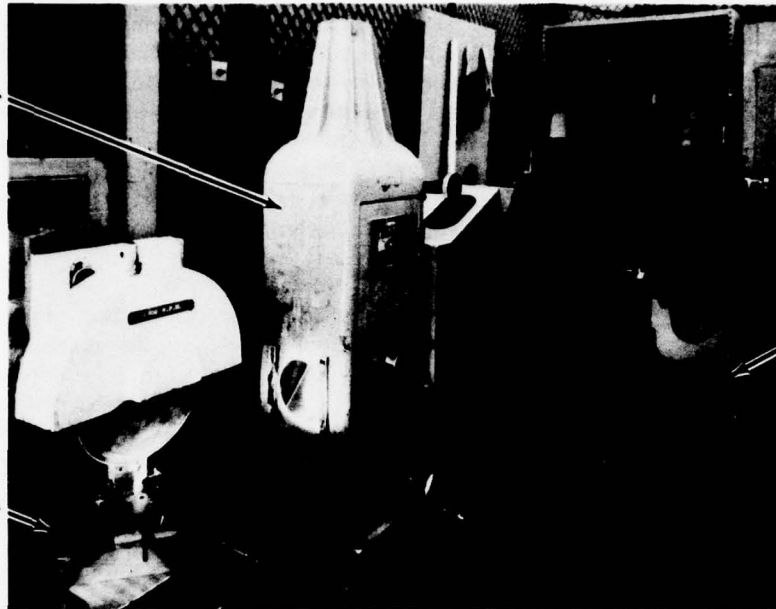
10X View
of Ground
Dovetail

Rotary
Table

FE 161853

FD 124388

Figure 70. Visual Grinder Set Up for Dovetail Grinding

FE 161854

FD 124389

*Figure 71. Rotary Table Used to Rotate Dovetail Under Grinding
Wheel*

79

The convex and concave airfoil surfaces of both parts were gang-ground using the camfollower controlled floating table shown in Figure 72. To machine blades using this fabrication process, separate concave and convex airfoil contour models were produced and used as templates for the respective airfoil contours on the ceramic blade and endwall section. The ceramic block and model were supported by a pressurized air cushion which maintained the model in contact with the follower wheel. While the horizontal motion of the grinding machine table moved the ceramic block under a grinding wheel, the cam action of the follower on the model controlled the vertical motion of the floating table. Thus, the respective concave and convex contours of the model were duplicated on the ceramic surfaces as shown in Figures 73, 74, 75, and 76.

After machining each airfoil and endwall part, the dovetail contact radius and all sharp edges of each part were polished to remove the circumferential grinding marks and to radius the edges, respectively. This was done in an attempt to avoid fracture initiation due to the transverse grinding marks in the highly-stressed dovetail contact area and to avoid fracture initiation due to the sharp edges of each part. Previous studies indicate that both of these conditions, when stressed, promoted fracture initiation in hot pressed silicon nitride material (Reference 1). Thus, an attempt was made to alleviate the problem.

After polishing, each airfoil and endwall section was heat treated at 1800°F for 50 hr in air. Previous testing conducted by Garrett AiResearch Corp. on another ARPA-funded ceramics program (Reference 4) indicated that this heat treatment significantly increased the flexural strength and impact resistance of transversely ground ceramic MOR test specimens.* Upon completing heat treatment, the airfoil and endwall sections were ready for room temperature proof spin testing (which will be discussed later in paragraph 2b).

2. Airfoil Analytical and Experimental Analyses

In summarizing this subtask, analytical and experimental analyses of the airfoil and endwall designs were conducted to evaluate the "platformless blade" concept. The analytical study consisted of a two-dimensional plate element analysis of these components to determine localized operational stresses in each component. Additionally, a maximum allowable flaw size calculation was conducted for the airfoil and endwall designs to determine the maximum acceptable flaw size for successful spin testing at 60,000 rpm. The experimental analysis consisted of spin testing to failure and proof spin testing of individual airfoil and endwall components. This testing was conducted to verify or update the analytical study conclusions.

a. Airfoil Analytical Analysis

During the design, and prior to fabrication of the airfoil and endwall components, an analytical structural analysis of the platformless blade concept was conducted to evaluate the integrity of the chosen airfoil and endwall design. This analysis consisted of a NASTRAN plate element analysis of the airfoil and endwall components to determine local operational stresses. Since the blades and endwalls are not integral components, each was evaluated separately. However, both analyses were performed for a rotor speed of 60,000 rpm assuming a linear airfoil thermal gradient from 2250°F blade tip temperature to 1590°F at the airfoil base, to 1460°F at the dovetail base. This speed was chosen because it is characteristic of typical small gas turbine engines, and these temperatures were chosen from previous testing as the worst acceptable spin test conditions. The airfoil component analysis was conducted utilizing separate plate element analyses for the concave and convex airfoil surfaces. Figure 77 illustrates the element breakup used for the blade model concave surface analysis.

*Specimens ground transverse to the bending direction anticipated during testing.

FD 116498A
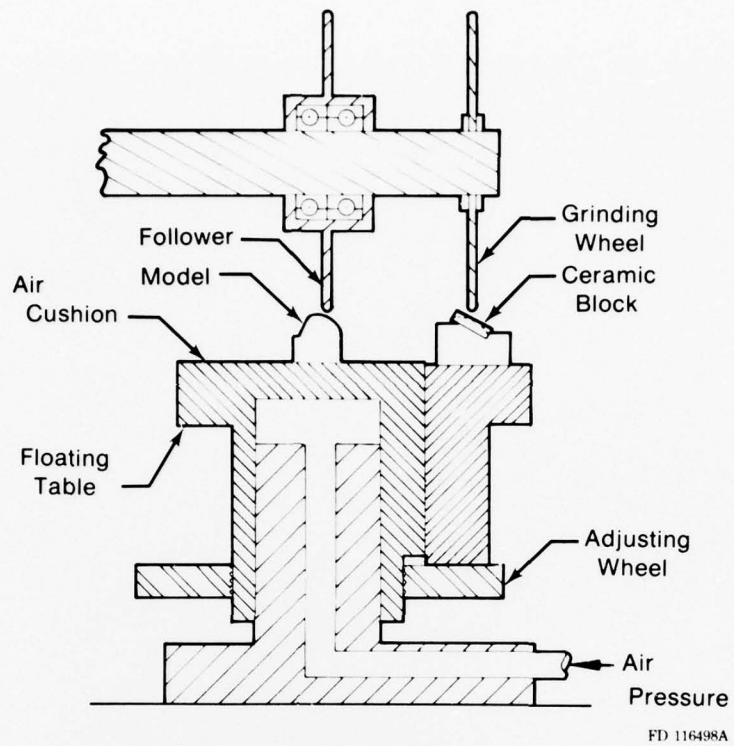
Figure 72. Air Cushion Duplicating Fixture
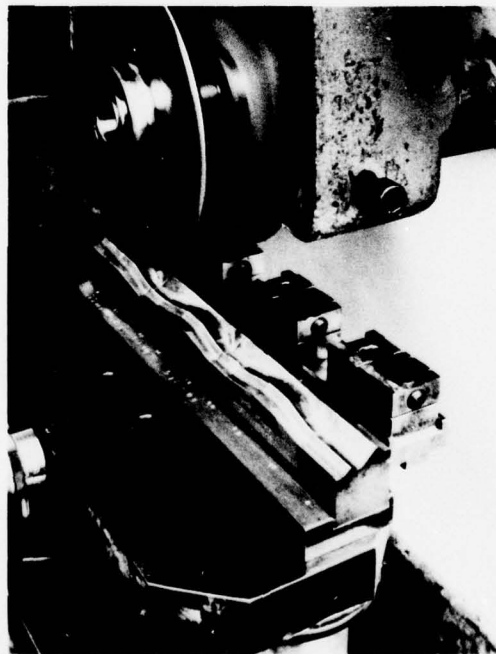
FD 124390

Figure 73. Set-Up for Gang Grinding Airfoil Concave Surfaces
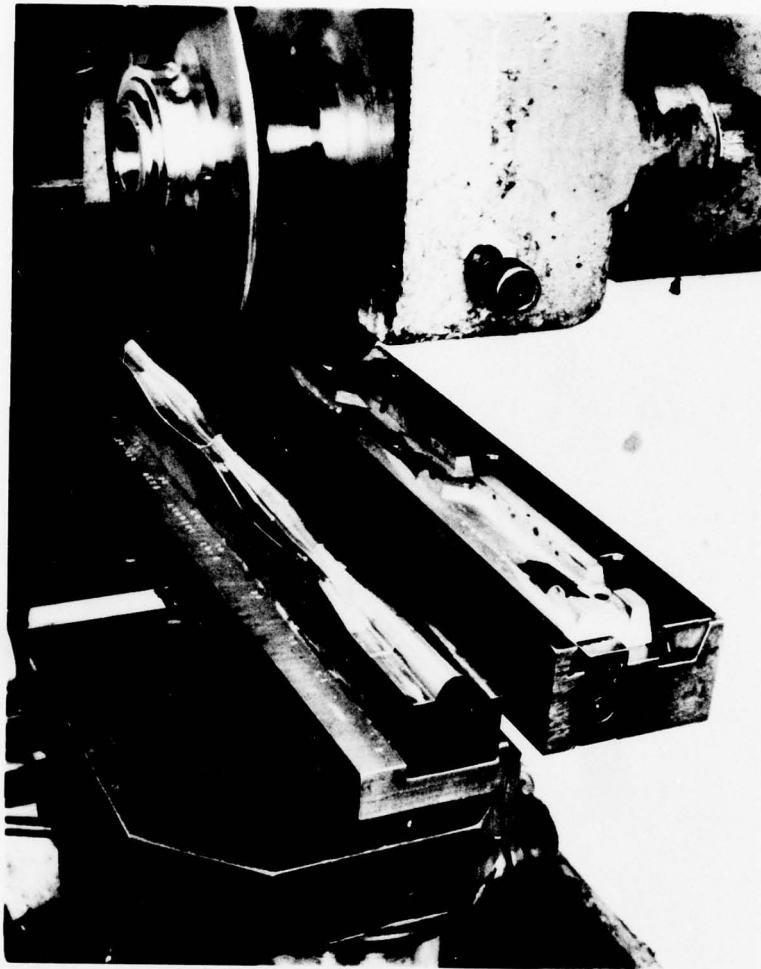
FD 124391

Figure 74. Set-Up for Grinding Airfoil Convex Surfaces
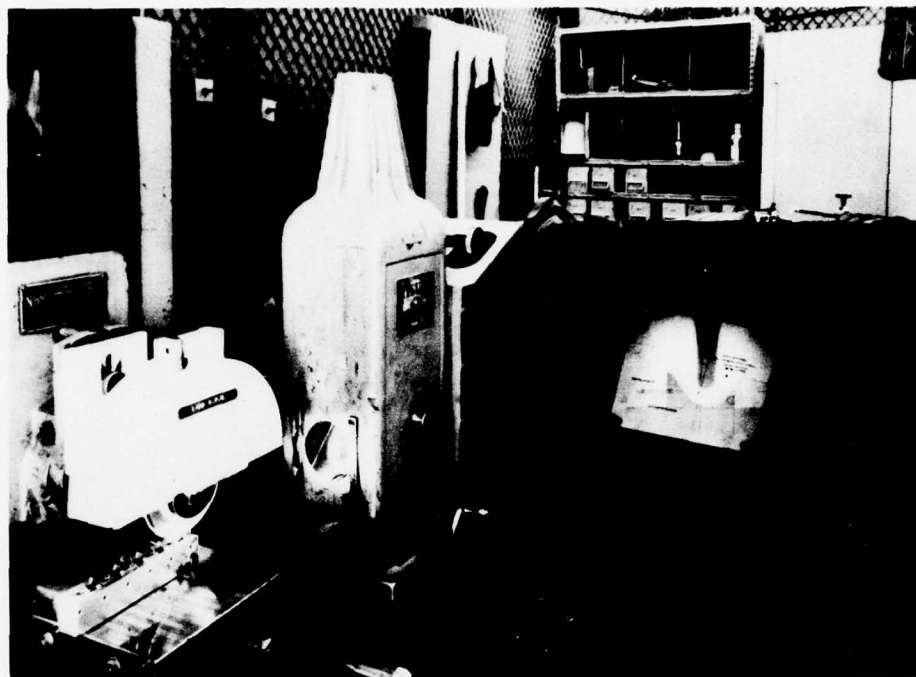
FE 162366

a. Setup
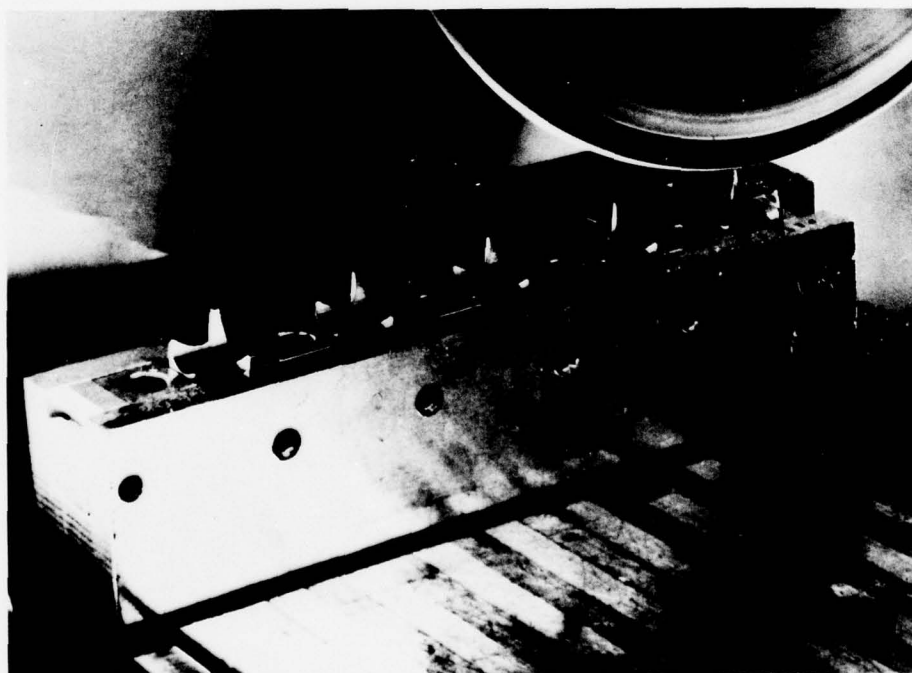
FE 161863

b. Closeup

FD 124397

Figure 75. Endwall Concave Surface Fabrication

83
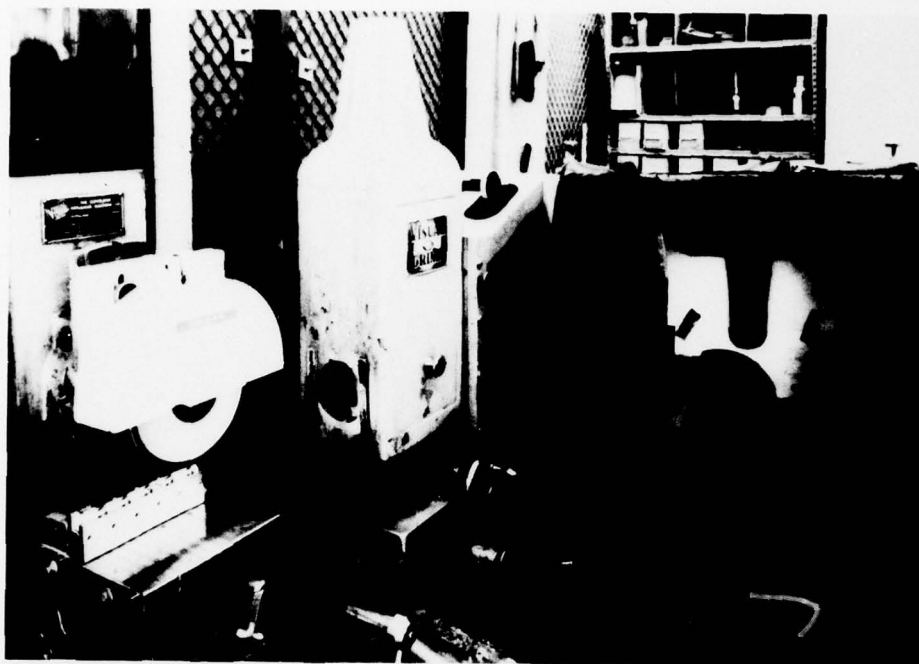
FE 161860

a. Setup
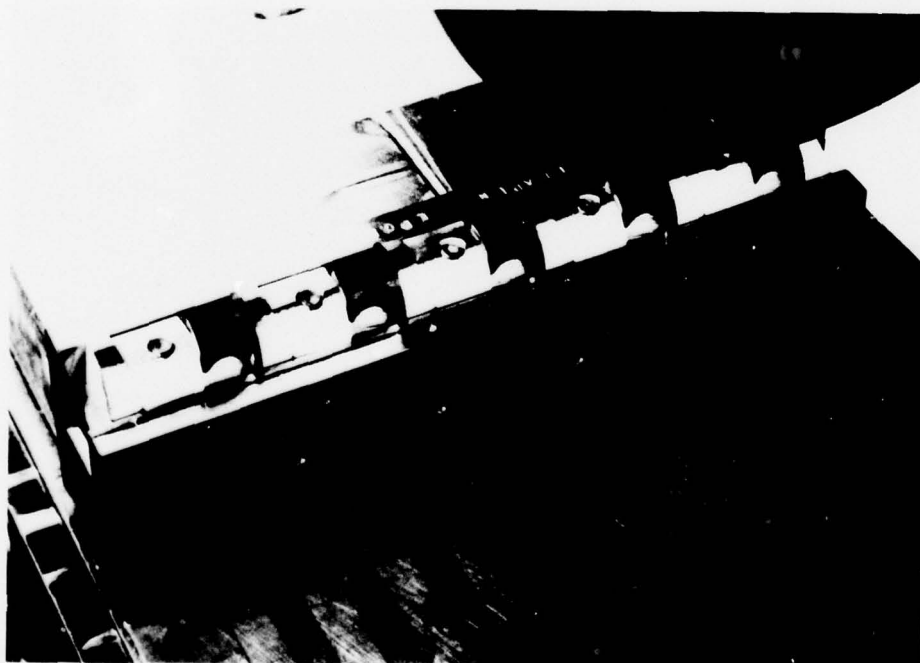
FE 162427

b. Closeup

FD 124398

Figure 76. Endwall Convex Surface Fabrication

84

END
DATE
FILMED
4—79
DDC

Concave Side View

Figure 77. Element Breakup

FD 124371

85

The results of these analyses were evaluated by using allowable stress criteria (Reference 5) previously used by P&WA/Florida in evaluating a JT15D ceramic blade design under Contract F33615-76-C-2128, Design Study of Ceramic Components for Turbine Engines. In this appr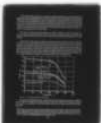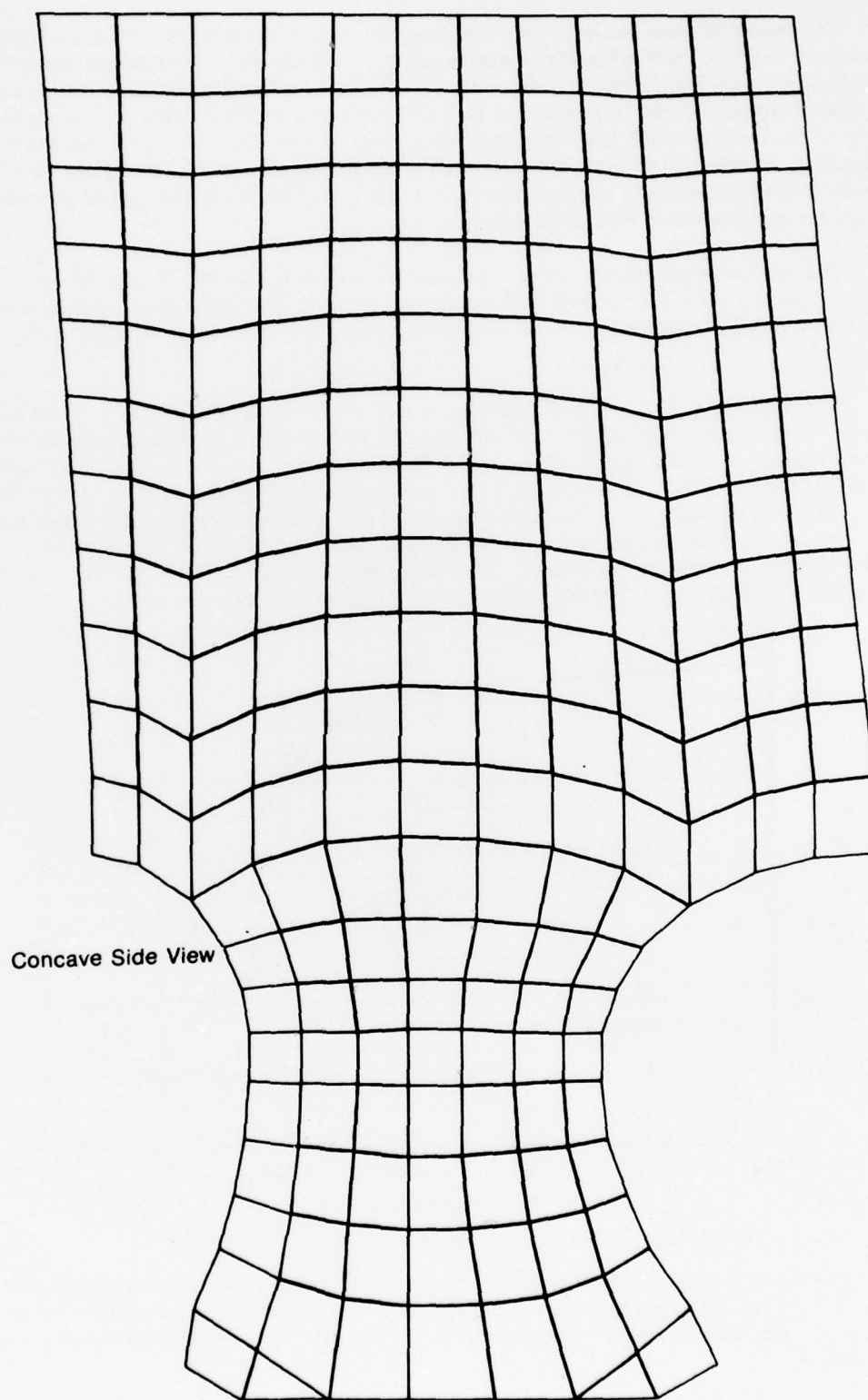oach, calculated stress was classified as either uniaxial tension or bending stress and was evaluated in terms of the criteria which best described the loading. Allowable stress curves for the two types of loading, as determined from material testing for hot pressed Si_3N_4, are shown in Figure 78. These curves represent the ultimate strength of the material, where the typical procedure is to design for approximately 60% of this stress.

The results of the initial airfoil analysis, as shown in Figures 79 and 80, illustrate the concave surface principal stresses and the convex surface principal stresses, respectively. The maximum predicted stress was 30 ksi and occurred in the dovetail leading edge of the concave surface.*

Although the initial analysis indicated a maximum stress less than the 40 ksi allowable (using 60% of the uniaxial tensile strength criteria), an additional analytical analysis conducted during the experimental airfoil study indicated a maximum stress that was 18 ksi above this allowable stress (58 ksi). However, since the maximum speed capability of the spin tooling was previously determined to be 53,000 rpm, the 58 ksi predicted maximum airfoil stress (at 60,000 rpm) was recalculated to be 45.3 ksi for 53,000 rpm. Although this stress was still in excess of the 40 ksi allowable, proof testing of each airfoil was planned to substantiate the airfoil design at a rotor speed of 60,000 rpm. Details of this testing are discussed in paragraph 2b.
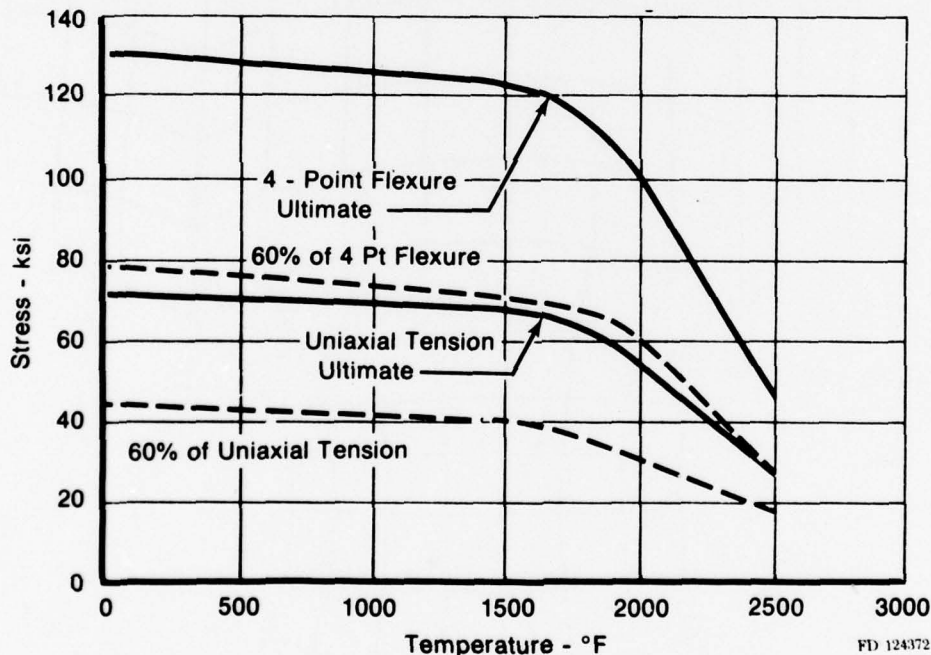
Figure 78. Strength of Hot Pressed Si_3N_4

The maximum allowable flaw size calculated for this blade configuration spinning at 60,000 rpm was 0.003 in. This flaw size could go undetected, thus care and effort in machining, polishing, and inspection were required to alleviate possible surface flaw problems associated with these operations.

---

* Additional airfoil analysis was conducted during a subsequent experimental analysis to verify the basic airfoil model used in determining the 30 ksi maximum predicted stress shown above. This analysis revealed an error in the airfoil model. Subsequently, upon correcting this error, the analysis was repeated, resulting in a predicted stress of 58 si (at 60,000 rpm and 2250°F blade temperature) located in the concave "trailing" edge surface of the dovetail contact radius. This is discussed in the following experimental airfoil analysis section.

86

Units in ksi
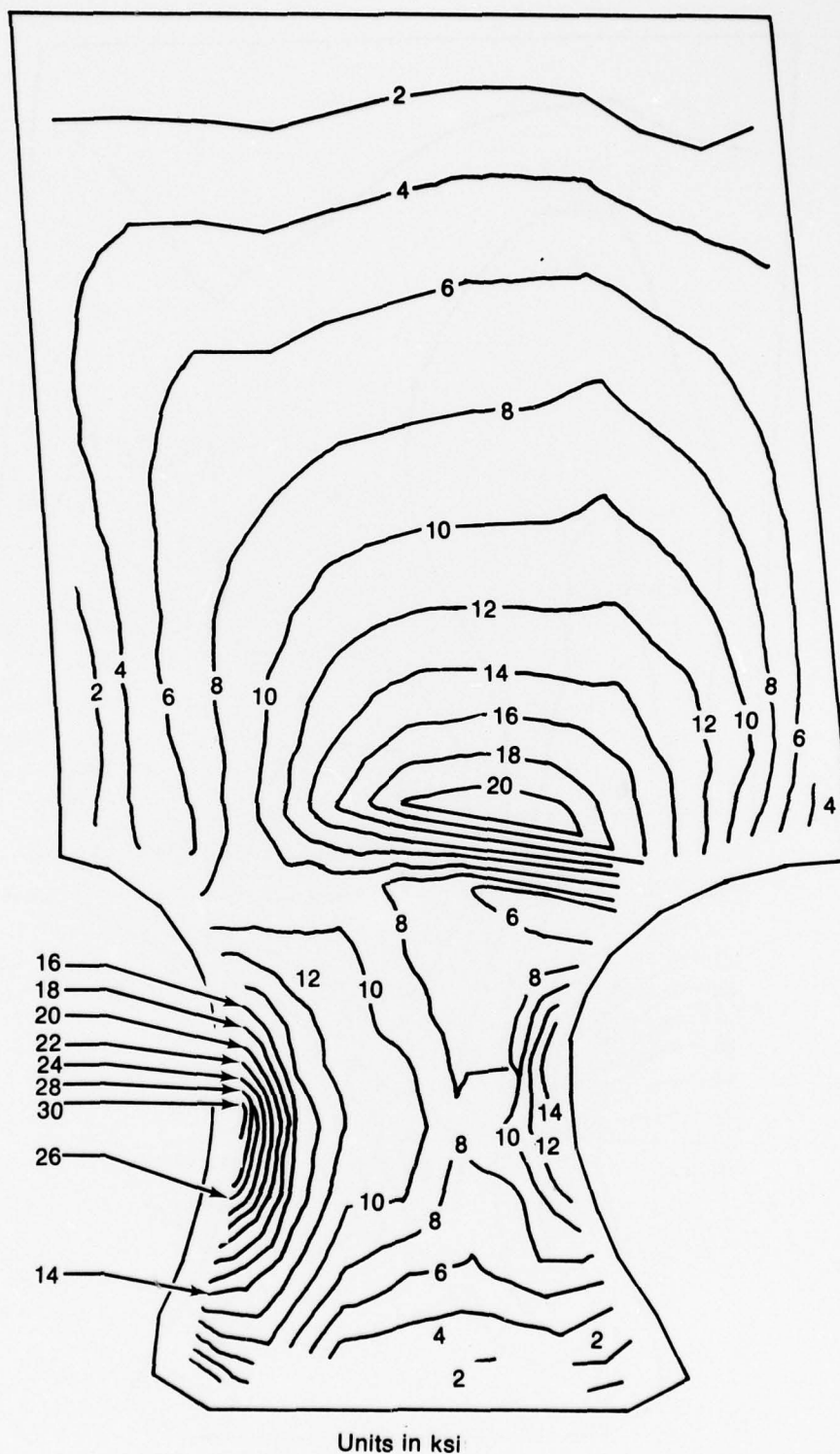
Figure 79. Major Principal Surface Stress, Concave Side, Combined Loads,
Original Model

87

Units in ksi
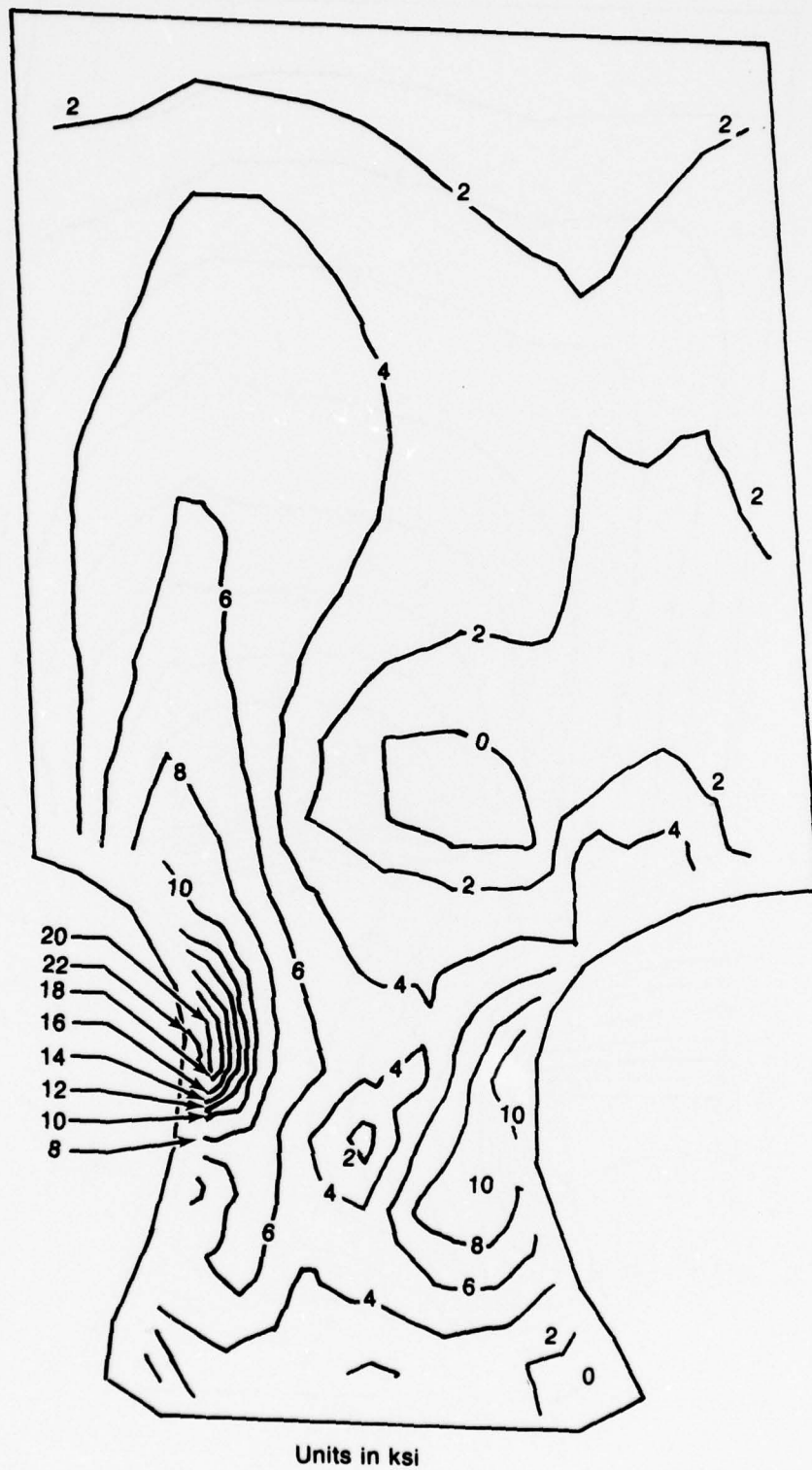
FD 124376

Figure 80. Major Principal Surface Stress, Convex Side, Combined Loads, Original Model

When the airfoil analysis was completed, an analysis of the endwall component design was conducted. Overall loads on the endwall were expected to be low due to the low endwall mass and large attachment cross-section. However, portions of the endwall that overhang the front and rear of the attachment, (Figure 81) would be subjected to considerable bending by centrifugal loading. To simplify the analysis, substructure models of these areas were composed of plate elements and constrained so as to represent attachment to the rigid bulk of the remainder of the endwall.
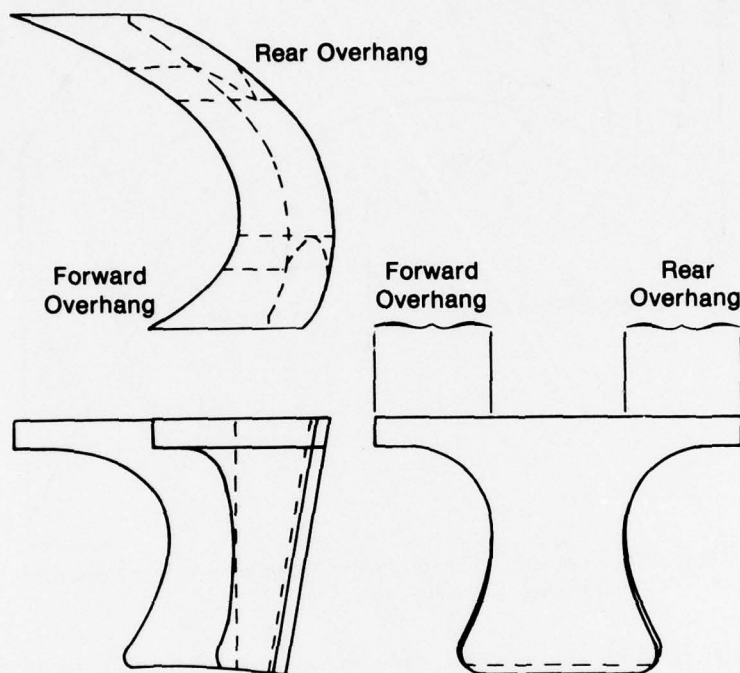
Figure 81. Ceramic Endwall Design

FD 124382A

Only centrifugal loading at 1500°F was analyzed because of the uncertainty of thermal and attachment induced loads. Stresses were calculated for the lower surface (attachment side) of the endwall; the upper surface was to be primarily in compression and was not considered here. These stresses were evaluated conservatively using the uniaxial tension criteria previously mentioned, as well as the maximum allowable flaw size.

The results of this analysis are shown in Figure 82. The maximum stresses are 9 and 17 ksi, respectively, for the front and rear overhangs. These stress levels are well below the 40 ksi maximum allowable stress of the uniaxial tension criteria previously discussed.

Maximum allowable surface flaw sizes were calculated as 0.035 in. and 0.010 in. for the front and rear overhangs, respectively, for this configuration endwall. Flaws of this size were not likely to be undetected; however, the same care and effort in machining, polishing, and inspecting the airfoil blades were applied to the endwall components.

b. Airfoil Experimental Analysis

Prior to fabrication and spin testing of the fully-bladed rotor, additional airfoil experimental evaluation was planned to verify the previously conducted analytical study. This evaluation consisted of spin testing airfoil and endwall components at room temperature, conducting a subsequent failure analysis of the failed components, and room-temperature proof spin testing of each airfoil to be installed in the hybrid fully-bladed rotor.

Leading Edge

2
4
6
8
-9 ksi
5
Trailing Edge
10 5
15
Blade Stacking Point
17 ksi
5
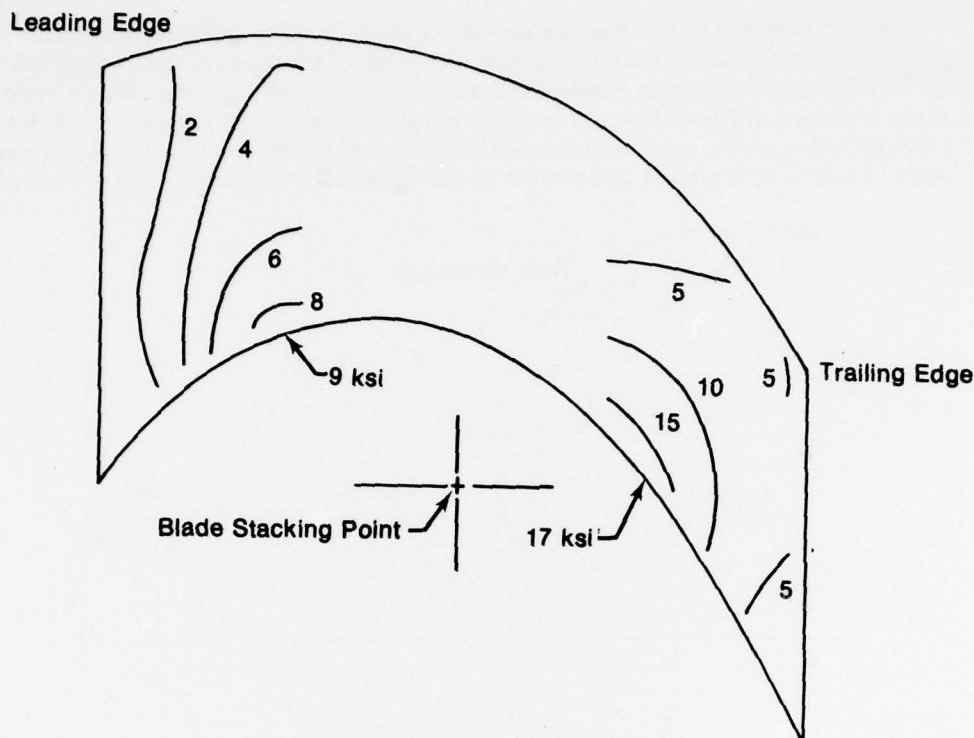
FD 124366A

*Figure 82. Ceramic Endwall (Lower Surface) Leading Edge and
Trailing Edge Stresses*

Initially, six airfoil blades were room-temperature proof spin tested (to 150% of the design load) to experimentally determine any inherent weaknesses in the design that were not detected by the analytical study. The design load is that load which the airfoil experiences spinning at 60,000 rpm in the fully-bladed hybrid rotor. It should be noted that, even though the maximum elevated-temperature rotor speed was limited to 53,000 rpm, this proof testing was conducted at speeds in excess of the design load speed (60,000 rpm) to substantiate the room-temperature integrity of these blades with respect to the centrifugal loading of typical small gas turbine engines.

Upon proof testing the six airfoils, three of the test blades successfully reached the 150% load level. The remaining three failed at levels corresponding to 75%, 137%, and 150% of the design loads. Subsequently, the three successfully proof tested airfoils were also spun to failure, and failure load levels of 167%, 168%, and 188% were attained. Table 10 lists the failure speeds, corresponding percent of design loads, and the equivalent fully-bladed hybrid rotor speed.

Although additional data were required for a statistically meaningful conclusion, these initial results were encouraging and indicated that proof testing airfoils prior to use would further improve hybrid rotor integrity.

A failure analysis of the root sections of the six failed ceramic airfoils was performed to determine the location of the fracture origin. Features of the fracture surfaces indicated that all failures initiated in the dovetail near the concave-trailing edge corner, as shown in Figure 83. This failure location was in conflict with the initial NASTRAN plate analysis prediction which showed the area of maximum stress as located on the leading edge of the concave surface. This discrepancy, prompted a reevaluation of the airfoil model used to conduct the initial analysis.

90

Upon reevaluation, an error in the basic airfoil model was detected. The error was corrected and a reanalysis of the airfoil stress levels at 60,000 rpm was conducted. This resulted in indicated maximum principal stresses of 58 ksi and 40 ksi in the concave and convex surface trailing edge corners of the airfoil, respectively, as shown in Figures 84 and 85. This failure location was in agreement with the actual fracture origin area determined for the six failed ceramic airfoils mentioned above.

TABLE 10. AIRFOIL CERAMIC BLADE SPIN TEST RESULTS

Airfoil S/N	Failure Speed (rpm)	Fully Bladed Hybrid Rotor Design Load (%)	Equivalent Fully Bladed Hybrid Rotor Speed (rpm)
1	54,000	188	82,250
2	48000	150	73,000
3	51,000	168	77,700
4	46,000	137	70,100
5	50,900	167	77,500
6	34,000	75	51,700
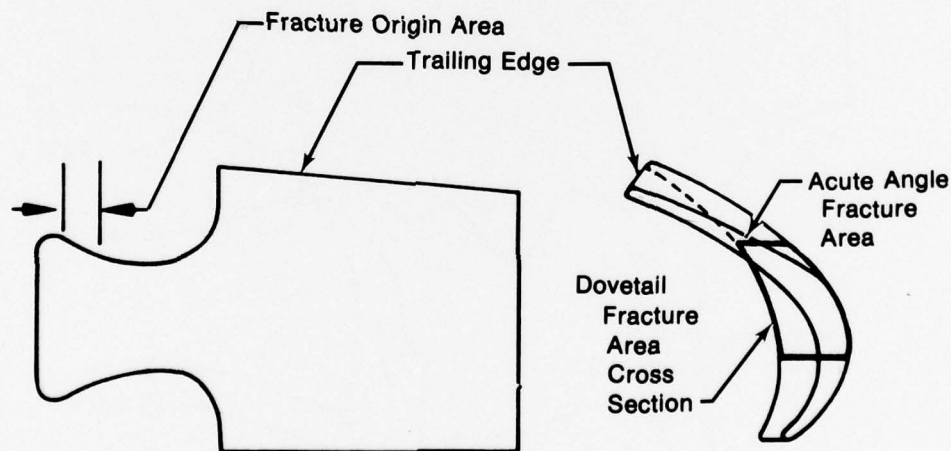
FD 131163A

Figure 83. Fracture Origin Location on Failed Airfoil Blades

Subsequently, six "endwall" components were successfully proof spin tested to 150% of the design load levels. These results were anticipated as the previously conducted analytical study predicted a maximum dovetail stress of only 17 ksi (as compared to 58 ksi for the airfoil). Although subsequent mechanical problems in the spin facility precluded additional failure testing, these results were sufficiently encouraging to substantiate the applicability of the platformless blade concept.
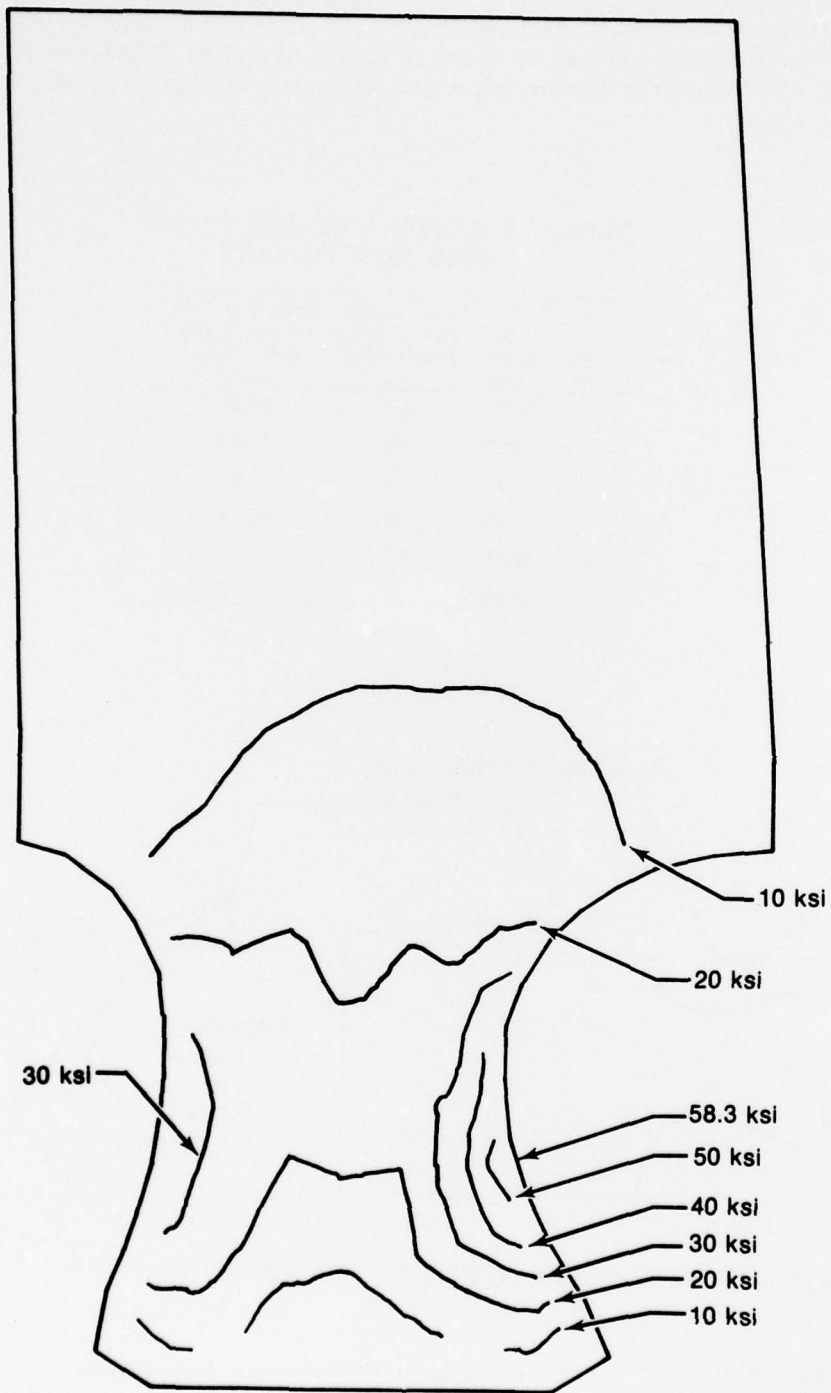
FD 140382

Figure 84. Major Principal Surface Stress at 60,000 rpm, Concave Surface, Corrected Model

92

10 ksi

20 ksi

40 ksi

30 ksi

20 ksi

10 ksi

20 ksi

10 ksi
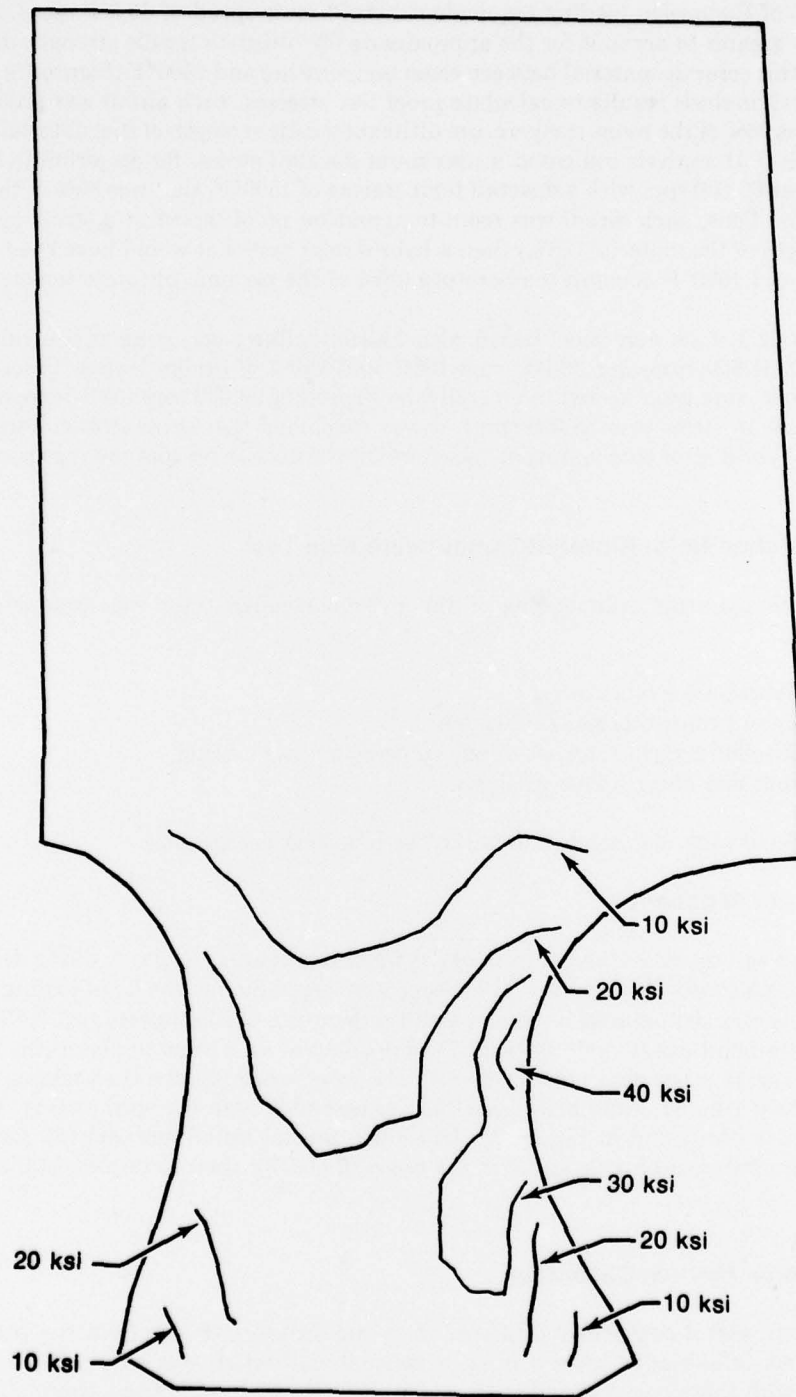
FD 140384

Figure 85. Major Principal Surface Stress at 60,000 rpm, Convex
Surface, Corrected Model

93

Prior to hybrid rotor fabrication, all airfoil components were room-temperature proof spin tested to 120% of the design loading (equivalent hybrid rotor speed of 66,000 rpm). The airfoil stress was 20% greater to account for the approximate 6% ultimate tensile strength degradation that occurs in this ceramic material between room temperature and 1500°F (Figure 78). Using the airfoil analytical analysis results to calculate proof test stresses, each airfoil was proof tested at a stress that was 98% of the room-temperature ultimate tensile strength of the material. However, the airfoil analytical analysis indicated a maximum dovetail stress, for an airfoil in the hybrid rotor spinning at 60,000 rpm with a dovetail temperature of 1500°F, that was 85% of the ultimate tensile strength. Thus, each airfoil was room-temperature proof tested at a stress closer to the ultimate strength of the material (98%) than a hybrid rotor test that would have been conducted at 60,000 rpm and 1500°F dovetail temperature (85% of the ceramic ultimate tensile strength).

A total of 32 airfoils were proof tested with 2 airfoil failures occurring at equivalent hybrid rotor speeds of 51,800 rpm and 66,000 rpm (86% and 120% of design loads). Since all of the remaining airfoils were proof tested to an equivalent speed of 66,000 rpm (32% increase in speed and 74% increase in stress over 53,000 rpm), it was concluded that these airfoils were obviously acceptable for hybrid rotor spin testing at speeds below the maximum spin tooling speed of 53,000 rpm.

3. Airfoiled Hybrid Rotor Elevated-Temperature Spin Test

Elevated-temperature spin testing of the hybrid airfoiled rotor was conducted in four subtasks:

a. Hybrid rotor fabrication
b. Hybrid rotor thermal calibration
c. Airfoiled hybrid rotor elevated temperature spin testing
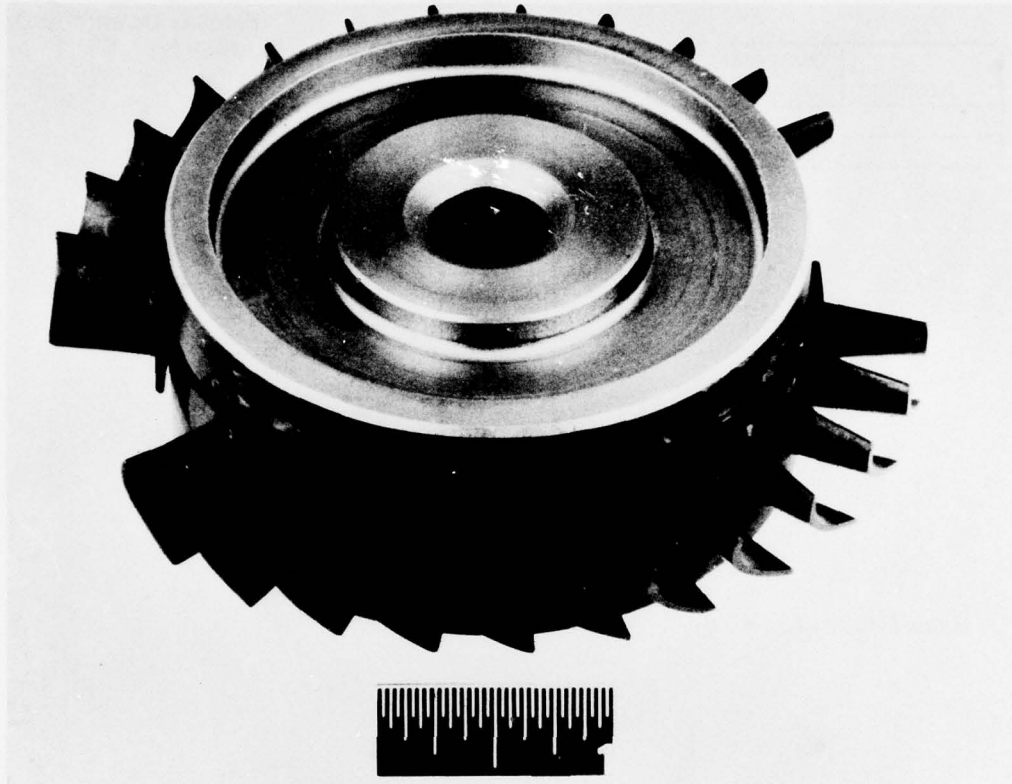d. Spin test abort failure analysis.

These subtasks are discussed in detail in the following paragraphs.

a. Hybrid Rotor Fabrication

After proof testing all airfoil components at room temperature to 120% of the design loads, airfoil, endwall, platinum shim, and rotor sections were assembled in the bond tooling. The bond tooling assembly was then placed in an elevated-temperature vacuum press and GATORIZED® per the diffusion bond upset cycle to bond the rotor halves as well as to clamp the airfoil and endwall components in the circumferential slot. The rotor assembly was then removed from the bond tooling, heat treated, and finish machined for assembly with the spin tooling. The finish-machined rotor is illustrated in Figure 86. As shown, several airfoil and endwall sections were omitted from the rotor to provide space in the dovetail slot for thermocouple installation.

b. Hybrid Rotor Thermal Calibration

Since these airfoil components differed in configuration and size from the pseudoblades used in previous fully-bladed rotor testing, a thermal calibration was required. The rotor was instrumented with thermocouples in the locations shown in Figure 87, and a thermal calibration was conducted. The resultant temperatures are shown in Figure 87. As illustrated, with a 2250°F blade temperature, the highest stressed area of the attachment shown in location 2 (Figure 87) was at 1430°F. As mentioned upon concluding the experimental analysis, this rotor temperature would easily permit completing a 50-hr hot spin test at speeds as high as 60,000 rpm.

94

FE 167243

Figure 86. Hybrid Rotor Prior to Assembly With Spin Tooling

95

Location	Temperature (°F)
1	2250
2	1430

3/16 dia Support Spindle (Extends Upward to Drive Turbine)

Tooling Shaft
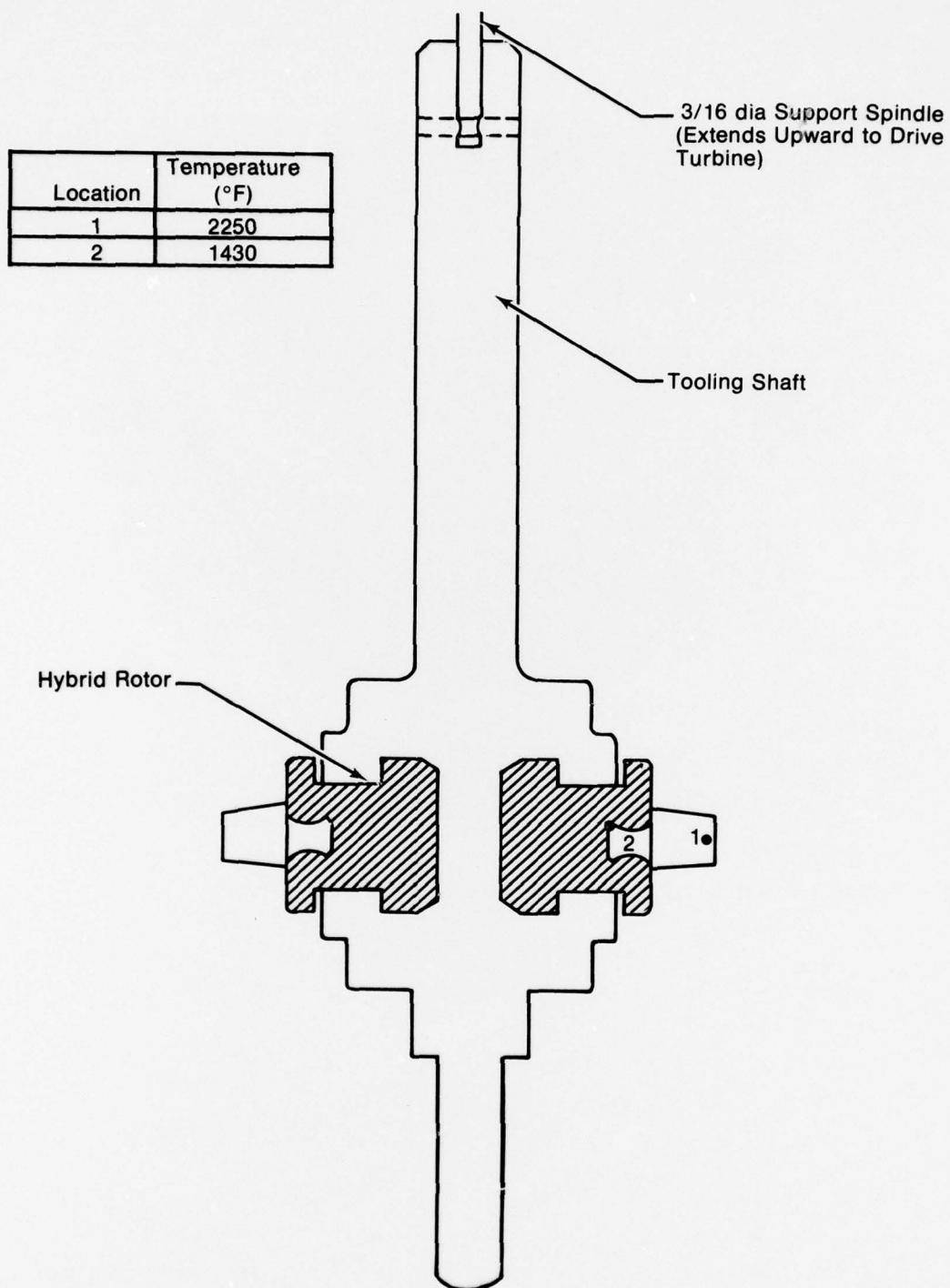
Hybrid Rotor

FD 140379

Figure 87. Hybrid Rotor/Spin Tooling Assembly Showing Thermocouple Locations

c. Airfoiled Hybrid Rotor Elevated-Temperature Spin Test

Following thermal calibration, the program extension milestone spin test cycle was planned. Although previous spin testing during this program was conducted at constant rotor speeds and blade temperatures, the extension milestone spin test goal was changed to more closely simulate a typical 50-hr turbine cycle for a gas turbine engine with this type of technological application. The scheduled test cycle established for this milestone is shown in Figure 88. As shown, the speed was to be varied between 30,000 and 50,200 rpm to simulate the different turbine operating speeds encountered in a typical engine cycle. This cycle was to be repeated four times to accumulate a total of 50 hr of testing at a blade temperature of 2250°F. The maximum rotor speed of 50,200 rpm was chosen for two reasons even though all blades had passed the 120% stress proof spin. First, this speed corresponds to the 60% allowable dovetail maximum stress of 40 ksi (at a 1500°F dovetail temperature as shown in Figure 78) as calculated from the airfoil analytical study results.* Second, this speed was below the 53,000 rpm speed previously indicated as the maximum allowable spin tooling speed without a tool redesign and build.

FD 140380
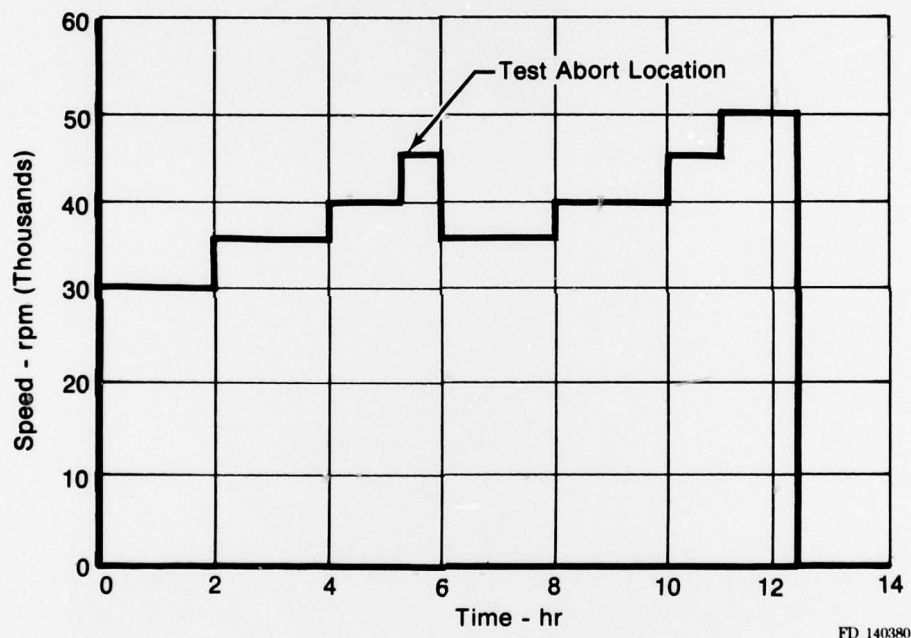
Figure 88. Scheduled Hybrid Rotor Milestone Spin Test Cycle

With the spin test cycle established, the program extension milestone test was initiated. After spinning for 5 hr at the various speeds shown in Figure 88, an abrupt test abort occurred (after 5 min at 45,000 rpm) failing approximately 70% of the airfoil and endwall components. Figures 89A and 89B illustrate the rotor after removal from the spin facility and prior to failure analysis.

---

* The airfoil analytical study predicted a maximum dovetail trailing edge stress of 58 ksi at 60,000 rpm and 1500°F. Using this correlation, a speed of 50,200 rpm was calculated to produce the 60% allowable stress of 40 ksi.
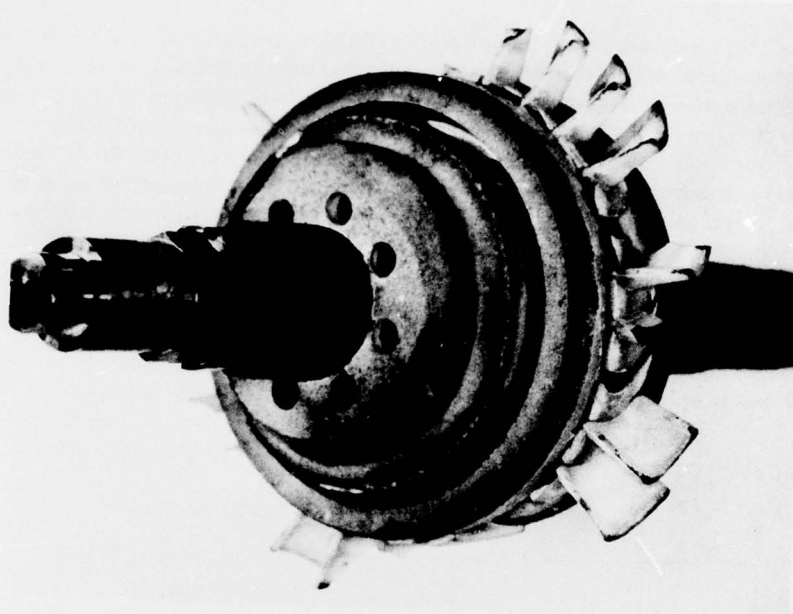
A.   FAL 47846
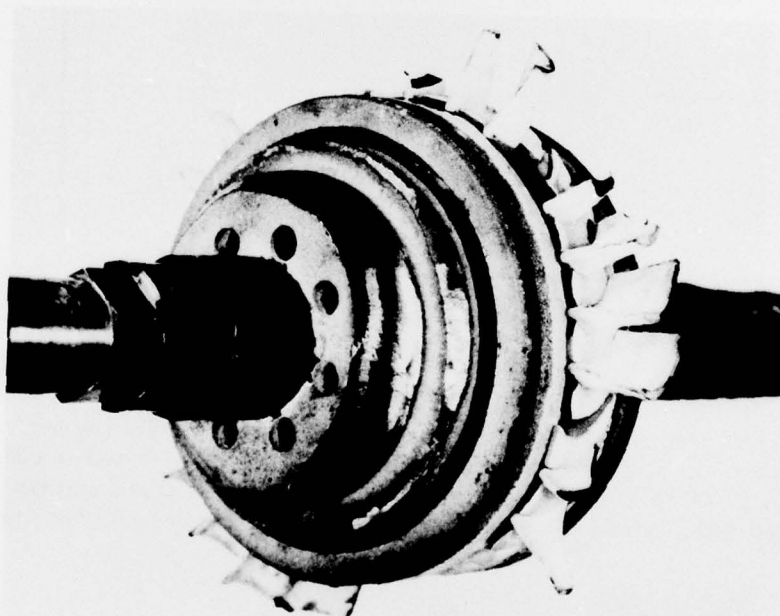
B.   FAL 47847

                                                           FD 140381

Figure 89. Ceramic Bladed Rotor After Test Abort at 45,000 rpm. The Rotor is Rotated 180 deg to Show Both Sides in the Two Views

98

d. *Spin Test Abort Failure Analysis*

Failure analysis of the hybrid rotor/tooling assembly indicated the test abort and subsequent blade failures were due to spin tooling failure. A 3/16-in. diameter metal spindle (Figure 87) supporting and connecting the spin tooling/rotor assembly to the drive turbine failed, thus causing the assembly to drop slightly and impact against adjacent metal structures as it slowed from 45,000 rpm. The airfoil and endwall components fractured as a result of these impacts. An analysis of each of the ceramic fracture surfaces indicated failure due to impact and not due to centrifugal loading.

With the completion of the program extension milestone spin test requirement, the GATORIZED hybrid airfoiled rotor in an elevated-temperature environment was successfully demonstrated.

SECTION V
CONCLUSIONS AND RECOMMENDATIONS

CONCLUSIONS:

1. An airfoiled hybrid rotor was demonstrated by spin testing at speeds and temperatures characteristic of small gas turbine engine operation for short life applications, typically 50 hr.

2. A "platformless blade" airfoil concept that segregates the conventional blade configuration into separate airfoil and platform (endwall) sections was developed and demonstrated for the circumferential hybrid attachment approach. Potential fabrication costs of this concept indicate airfoil-endwall unit costs reduced by a factor of 10 over existing methods used to fabricate conventional type ceramic blades of the same material. This fabrication process also represents a practical method for high volume machining of blades from hot-pressed ceramic material. In addition, this airfoil configuration is a viable shape for hot pressing in large quantity to near net shape to further reduce unit cost.

3. Elevated temperature hybrid rotor integrity was demonstrated with the testing of two ceramic pseudobladed rotors at 45,000 rpm and 2250°F blade temperature for 88 and 54 hr, respectively, without failure.

4. Attachment concept room temperature feasibility was demonstrated by determining the 3-σ lower bound load capability (20.5 ksi) of single hybrid attachments.

5. The use of experimental analyses to predict hybrid rotor life at elevated temperature was successfully demonstrated by correlating Larson-Miller strain plots with analytical models and actual hardware failures.

6. A good correlation was obtained between analytical modeling of the "platformless" blade and experimental spin test results. Airfoil maximum stress and failure locations were predicted yielding a high reliability design model.

7. Proof testing of individual blades to eliminate unexpected failures prior to hybrid rotor fabrication was proven to be a satisfactory method for this application.

RECOMMENDATIONS:

1. Since most ceramic work to date has been directed toward short life applications, larger life testing of this material should be conducted to verify and expand technology readiness for other extended life applications.

2. Explicit definition of performance requirements for an engine using ceramic materials in the turbine is also recommended. This will result in setting specific design goals and material requirements for this application of ceramic technology.

3. A basic life prediction methodology for elevated temperature high strength brittle ceramic materials should be developed. Development should include NDE correlations between predicted allowable flaw sizes, actual detected flaws, and actual hardware failures. This methodology would also enhance the ability to set specific design goals and material capabilities with respect to performance requirements as mentioned above.

4.   To further advance the state of the art in ceramic materials, funding of a major methodology program in ceramic material processing is recommended to develop low cost, high quality ceramics for elevated temperature applications.

5.   Lastly, we strongly recommend application of this hybrid rotor concept in a turbine engine. As mentioned, this concept and individual ceramic components have been demonstrated at steady-state temperatures and stresses comparable to small gas turbine engine operation. However, the ultimate method of proving a new concept such as the circumferential hybrid attachment is by testing the concept in a gas turbine engine.

REFERENCES

1. Brennon, J. J. and F. Lemkey, "Development of Si_3N_4 and Sic of Improved Toughness," Interim Report under Contract NAS3-19731, 15 January 1977, Report No. R77-912252-17.

2. McLean, A. F., E. A. Fisher, R. J. Bratton, and D. G. Miller, "Brittle Materials Design, High Temperature Gas Turbine," Interim Report, October 1975, AMMRC CTR 75-28.

3. Calvert, G. S., J. P. Mitchell, "Design, Fabrication, and Spin Testing of Ceramic Blade-Metal Disk Attachment," Contract NAS3-19715, 1978, Report No. FR-10179.

4. "Ceramic Gas Turbine Engine Demonstration Program," Interim Report No. 2 for Contract N00024-76-C-5352, Garrett AiResearch Corp., Report No. 76-212188(2).

5. Trantina, G. G. and H. G. deLorenzi, "Design Methodology for Ceramic Structures," ASME Journal of Engineering for Power, Paper No. 77-GT-40.

Department of the Navy
Ships Systems Command
Washington, D.C. 20360
Attn: Code 03423

National Aeronautics and Space
Administration
600 Independence Avenue
Washington, D.C. 20546

Chief of Naval Research
Department of the Navy
Washington, D.C. 20360
Attn: ONR 423, 471 (2 copies)

U.S. Army Materials Research Agency
Watertown Arsenal
Watertown, Massachusetts 02172
Attn: Mr. S. Arnold

Director
U.S. Naval Research Laboratory
Metallurgy Division
Washington, D.C. 20390
Attn: Mr. W. Pellini

Commander
U.S. Army Munitions Command
Frankford Arsenal
Pitman Dunn Laboratory
Philadelphia, Pennsylvania 19137
Attn: Mr. K. Kleppinger

Commanding Officer
Naval Air Development Center, Johnsville
Aero Materials Laboratory
Warminster, Pennsylvania 18974
Attn: Mr. F. S. Williams

Battelle Memorial Institute
Defense Metals Information Center
505 King Avenue
Columbus, Ohio 43201

Air Force Materials Laboratory
Wright-Patterson Air Force Base
Dayton, Ohio 45433
Attn: Codes LLM, LC, MXE, MBC (1 each)

Avco Systems Division
Lowell Industrial Park
Lowell, Massachusetts 01851

Bell Helicopter Textron
Box 482
Fort Worth, Texas 76101

Brush Wellman, Inc.
17876 St. Clair Avenue
Cleveland, Ohio 44110
Attn: Mr. Bryce King

Sikorsky Aircraft
Stratford, Connecticut 06602
Attn: Dr. M. J. Salkind

The Boeing Company
Aerospace Division
P.O. Box 3707
Seattle, Washington 98124
Attn: Mr. E. C. Bovee

USAEC Division of Reactor
Development and Technology
Washington, D.C. 20545
Attn: Mr. J. M. Simmons, Chief
Metallurgy Section

Hughes Tool Company
Helicopter Division
Centinela Ave and Teale Street
Culver City, California 90230

Department of the Interior
Bureau of Mines
Washington, D.C. 20240

Defense Documentation Center
Cameron Station Bldg. 5
Alexandria, Virginia 22314
Attn: TISTA (14 copies)
Via: Naval Air Systems Command
        Code AIR-50174
        Washington, D.C. 20360

U.S. Department of Commerce
National Bureau of Standards
Washington, D.C. 20234

National Academy of Sciences
National Materials Advisory Board
2101 Constitution Avenue
Washington, D.C. 20418
Attn: Dr. J. C. Lane

The Franklin Institute Research
Laboratories
Benjamin Franklin
Pkwy at 20th Street
Philadelphia, Pennsylvania 19103
Attn: Technical Director

Douglas Aircraft Company
3855 Lakewood Blvd.
Long Beach, California 90846

General Dynamics
Convair Division
Box 80847
San Diego, California 92138
Attn: Mr. A. Hurlich

Aerotech, Inc.
4319 Alonzo Avenue
Encino, California 91316
Attn: Dr. A. W. Sommer

Boeing Vertol Company
Box 16858
Philadelphia, Pennsylvania 19142

Kaman Aerospace Corporation
Old Windsor Road
Bloomfield, Connecticut 06002

IIT Research Institute
10 West 35th Street
Chicago, Illinois 60616
Attn: Dr. N. Parikh

Kawecki Berylco Industries, Inc.
P.O. Box 1462
Reading, Pennsylvania 19603
Attn: Dr. G. London

Ladish Company
Packard Avenue
Cudahy, Wisconsin 53110
Attn: Mr. Joseph Picher, Librarian

Clevite Corporation
Mechanical Research Division
540 East 105th Street
Cleveland, Ohio 44108
Attn: Mr. A. D. Schwope

Lockheed Aircraft Corporation
Lockheed Missiles and Space Co., Inc.
P.O. Box 501 - Orgn. 80-72, Bldg. 18
Sunnyvale, California 91088
Attn: Dr. M. I. Jacobson

Lockheed Georgia Co.
Composites Materials Research
Dept. 72-15 Zone 402
Marietta, Georgia 30061
Attn: Mr. R. M. Gray

Avco Corporation
Lycoming Division
550 South Main Street
Stratford, Connecticut 06497
Attn: Division Library

P. R. Mallory & Co., Inc.
3029 East Washington Street
Indianapolis, Indiana 46206
Attn: Technical Librarian

Martin Marietta Aerospace
Orlando Division
P.O. Box 5837
Orlando, Florida 32805
Attn: Dr. Richard C. Hall
        Mail Point 275

Midwest Research Institute
425 Volker Boulevard
Kansas City, Missouri 64110

NASA Scientific and Technical
Information Facility
P.O. Box 33
College Park, Maryland 20740

North American Aviation
Autonetics Division
P.O. Box 4173
Anaheim, California 92803
Attn: Mr. A. G. Gross, Jr.
        Dept. 522-92

Union Carbide Corporation
Linde Company
P.O. Box 44
Tonawanda, New York 14152

Commonwealth Scientific
500 Pendleton Street
Alexandria, Virginia 22314
Attn: Mr. A. P. Divecha

Martin Marietta Aluminum
19200 South Western Avenue
Torrance, California 90509
Attn: Mr. Paul E. Anderson
(M/C 5401)

Reactive Metals, Inc.
Niles, Ohio 44446
Attn: Dr. Howard Bomberger

The Boeing Company
12842 72nd Ave., N.E.
Kirtland, Washington 98033
Attn: Mr. W. Spurr

Defense Advanced Research Projects Agency
1400 Wilson Boulevard
Arlington, Virginia 22209
Attn: Dr. E. C. vanReuth

Department of Materials Engineering
University of Illinois at Chicago Circle
Box 4348
Chicago, Illinois 60680
Attn: Dr. John A. Schey

Rockwell International Corporation
P.O. Box 1082
1027 Camino Dos Rios
Thousand Oaks, California 91320

Lockheed Missiles & Space Company, Inc.
Palo Alto Research Laboratory
3251 Hanover Street
Palo Alto, California 94304
Attn: Dr. Thomas E. Tietz, 52-31/204

Northrop Corporation
Aircraft Division
3901 West Broadway
Hawthorne, California 90250
Attn: Technical Information
3343-32

Titanium Metals Corporation of America
Henderson, Nevada 89015
Attn: Dr. Harry W. Rosenberg

Southwest Research Institute
8500 Culebra Road
P.O. Drawer 28510
San Antonio, Texas 78284
Attn: Dr. C. Gerald Gardner

Grumman Aerospace Corporation
Bethpage, New York 11714
Attn: Mr. R. Heitzmann (2 copies)

Reynolds Metals Corporation
Metallurgical Research Division
4th and Canal Streets
Richmond, Virginia 23261
Attn: Mr. George Esu
Research Metallurgist

McDonnell Aircraft Company
P.O. Box 516
St. Louis, Missouri 63166
Attn: Mr. H. C. Turner

Air Force Materials Laboratory
Wright-Patterson AFB, OH 45433
Attn: Dr. Norman Tallon

AiResearch Manufacturing Company of Arizona
Dept. 93-39M
402 South 36th Street
Phoenix, AZ 85034
Attn: Chief, Materials Engineering Department

IIT Research Institute
10 West 35th Street
Chicago, IL 60616
Attn: Dr. Kishor Kulkarni

Office of Naval Research, Code 471
Arlington, VA 22217
Attn: Dr. A. M. Diness

International Harvester Company
Solar Division
2200 Pacific Highway
San Diego, California 92138
Attn: Dr. A. G. Metcalfe

TRW Inc., Corporate Headquarters
23555 Euclid Avenue
Cleveland, Ohio 44117
Attn: Elizabeth Barrett

United Technologies Research Center
East Hartford, Connecticut 06108
Attn: Mr. Roy Fanti

Vought Corporation
P.O. Box 5907
Dallas, Texas 75222

Whittaker Corporation
Nuclear Metals Division
West Concord, Massachusetts 01718

Horizons Incorporated
2905 East 70th Street
Cleveland, Ohio 41404

Narmco Industries, Inc.
Research and Development Division
8125 Aero Drive
San Diego, California 92123
Attn: Technical Library

General Electric Company
Missile & Space Division
Materials Science Section
P.O. Box 8555
Philadelphia, Pennsylvania 91901
Attn: Technical Library

Reynolds Metals Company
Reynolds Metals Building
Richmond, Virginia 23218
Attn: Technical Library

Artech Corporation
2816 Fallfax Drive
Falls Church, Virginia 22042
Attn: Mr. Henry Hahn

Massachusetts Institute of Technology
Department of Metallurgy and Material
Science
Cambridge, Massachusetts 02139
Attn: Dr. W. A. Backofen (1)
Dr. N. J. Grant (1)

Westinghouse Electric Corporation
R&D Center
Beulah Road
Pittsburgh, Pennsylvania 15235
Attn: Dr. Donald F. Harrison

Bell Telephone Laboratories, Inc.
600 Mountain Avenue
Murray Hill, New Jersey 07974
Attn: Dr. Kenneth A. Jackson

General Electric Research Laboratory
Schenectady, New York 12301
Attn: Dr. Ron Wood (1)
Mr. David Lillie (1)

Cabot Corporation
Stellite Division
1020 West Park Avenue
Kokomo, Indiana 46901
Attn: Mr. H. E. Hersh

Aluminum Company of America
1200 Ring Bldg.
Washington, D.C. 20036
Attn: Mr. G. B. Barthold

Pratt & Whitney Aircraft Group
400 Main Street
East Hartford, Connecticut 06108

Department of Metallurgical
Engineering
Drexel University
32nd & Chestnut Streets
Philadelphia, Pennsylvania 19104

Tyco Laboratories, Inc.
16 Hickory Drive
Waltham, Massachusetts 02145
Attn: Dr. A. I. Mlavsky
Senior Vice President for
Technology & Director of
Corporate Technology